Charles University in Prague

Faculty of Mathematics and Physics

HABILITATION THESIS

Josef Mysliveček

Quantitative morphological information in model catalysis

Department of Surface and Plasma Science

Prague 2016

Acknowledgments

Table of Contents

1 Introduction

This Thesis deals with implementation of the experimental technique Scanning Tunneling Microscopy (STM) on the research in the field of model catalysis in the Surface Physics Group, Department of Surface and Plasma Science, Faculty of Mathematics and Physics, Charles University in Prague. STM allows investigating the morphology of model catalyst surfaces, extracting quantitative morphological information, and relating the quantitative morphological information to the information on the chemical state and the chemical reactivity of model catalysts. This allows performing advanced atomic-level studies into the physical and chemical processes controlling the reactivity, selectivity and stability of industrially relevant heterogeneous catalysts.

The Thesis takes a form of a commented compilation of my publications. The publications selected for the compilation are attached as Appendices 1-22. The Thesis, and the selected publications cover two topics representing the prerequisites for the model catalysis research employing the quantitative morphological information – the STM technique and its capabilities (Section 3, Appendices 1-4), and the self-organization phenomena governing the creation of surface nanostructures (Section 4, Appendices 5-10). Subsequently, the Thesis describes the model catalytic studies over ceria (CeO$_x$) and Pt-ceria model catalysts (Section 5, Appendices 11-22). The presented studies introduce novel ceria based model catalysts, where self-organization is employed to obtain atomic-level control of the morphology and stoichiometry of the model ceria surfaces as well as novel Pt-ceria model catalysts where the Pt load is ultimately dispersed in the form of single supported Pt ions.

2 Model catalysis

Model catalysis is a general denomination for a large spectrum of experimental and computational approaches towards understanding the physicochemical foundations of heterogeneous catalysis and to knowledge-based designing of more effective heterogeneous catalysts [1]. An industrial heterogeneous catalyst is a multiple phase nanostructured material where a nanostructured structural support is carrying a nanostructured catalyst, often in the form of a binary metal-oxide nanostructure [2], (Figure 1). The catalyzed chemical reactions are taking place on the very complex surface of the catalyst.
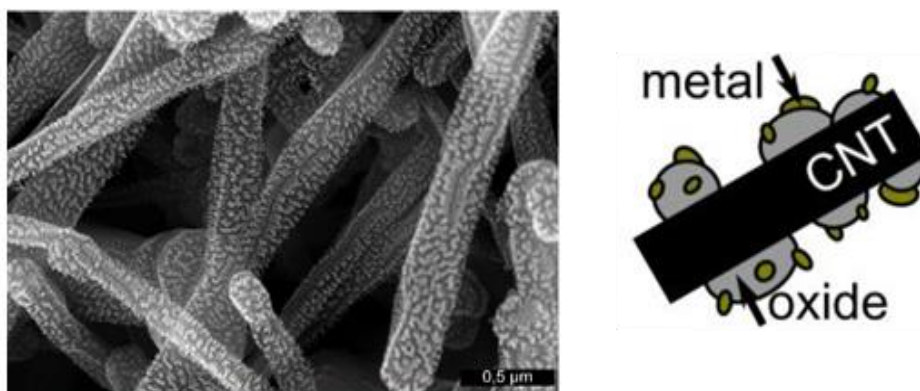
Figure 1. Left: scanning electron microscope image of a large-area oxide-metal heterogeneous catalyst on carbon nanotube support. Right: Schematic of the catalyst structure. Filip Dvořák, Ph.D. Thesis, Charles University in Prague, 2014 [2].

Model catalysis is following a so called "reductionism approach" [3] when structurally complex real catalysts are replaced by ordered surfaces with simple geometry. Historically, the first approximation to studying the properties of real catalysts was studying the physical and chemical properties of low-index metal surfaces representing idealized flat terminations of metal single crystals (Figure 2).

Pt(100) Pt(110) Pt(111)
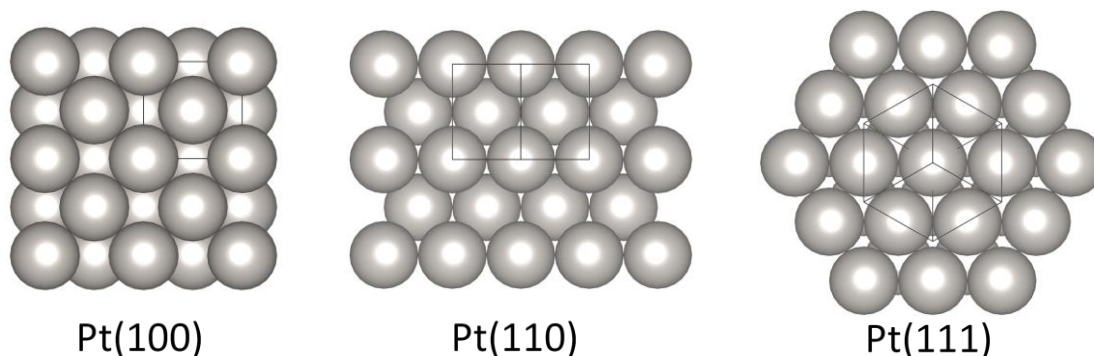
Figure 2: Top view of atom arrangement on different low-index surfaces of platinum. Outlined is the bulk unit cell of Pt.

The surface structure, the adsorption and desorption of reactants, and the kinetics of the surface chemical reactions on low-index single crystal surfaces have been clarified in detail by a growing number of surface sensitive experimental techniques, rendering surface science a mature scientific discipline in the second half of the 20th century [4]–[6]. The relevance of surface science on single crystal surfaces has been acknowledged by the award of Nobel prize in chemistry to Professor Gerhard Ertl in 2007 "for his studies of chemical processes on solid surfaces" [7], including a detailed understanding of one of the most important for mankind catalyzed reaction, the synthesis of ammonia by Haber-Bosch process [8].

2.1   Model catalysts with controlled complexity

In spite of its indisputable strengths, the surface science on single crystal surfaces is being criticized for the overly simplification that cannot clarify more complex catalytic reactions [9]. The difference between the simplicity of single crystal surfaces and the complexity of the real catalysts is referred to as "materials gap" [10]. For bridging the materials gap, several important concepts were developed. The surface science studies extended to oxide surfaces [11]–[15], the studies of surface chemical reactions extended to so called "active sites" – defects on low-index surfaces (Figure 3) that may deliver considerably more reactivity than the low-index surfaces alone [16]–[20], and the model catalytic studies extended to well-defined metal clusters supported on oxide surfaces [21]–[25].

Using the above concepts for resolving a particular problem in heterogeneous catalysis it becomes possible to prepare model catalysts with increasing but controlled complexity [26] (Figure 4) that allow to recognize the critical causalities without imposing unrealistic abstractions. Particularly, for supported metal catalysts the models with controlled complexity allow studying a broad range of processes that determine the catalytic properties of the supported metal catalyst [26] (Figure 5).
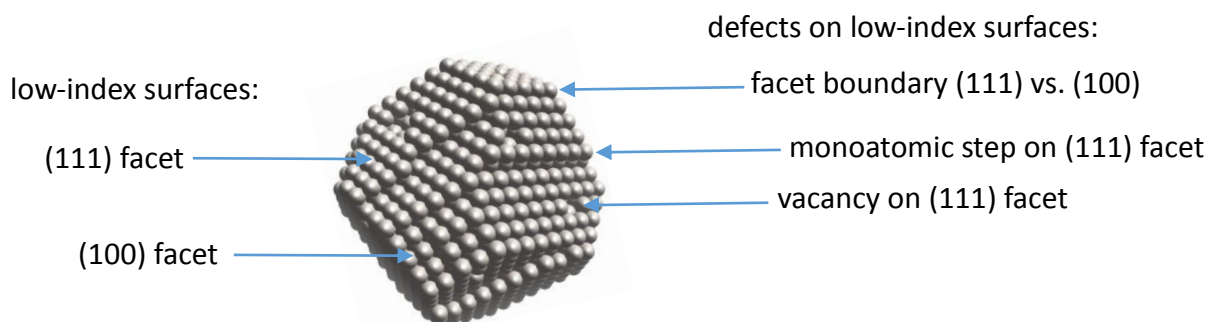
Figure 3: Defects on low-index surfaces that may act as active sites for heterogeneous catalytic reactions.
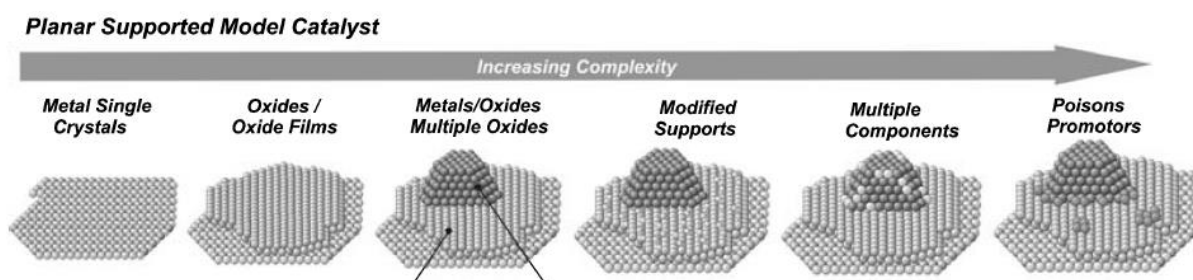
Figure 4: Hierarchical buildup of model catalysts with increasing but controlled complexity. Adapted from Ref. [26]
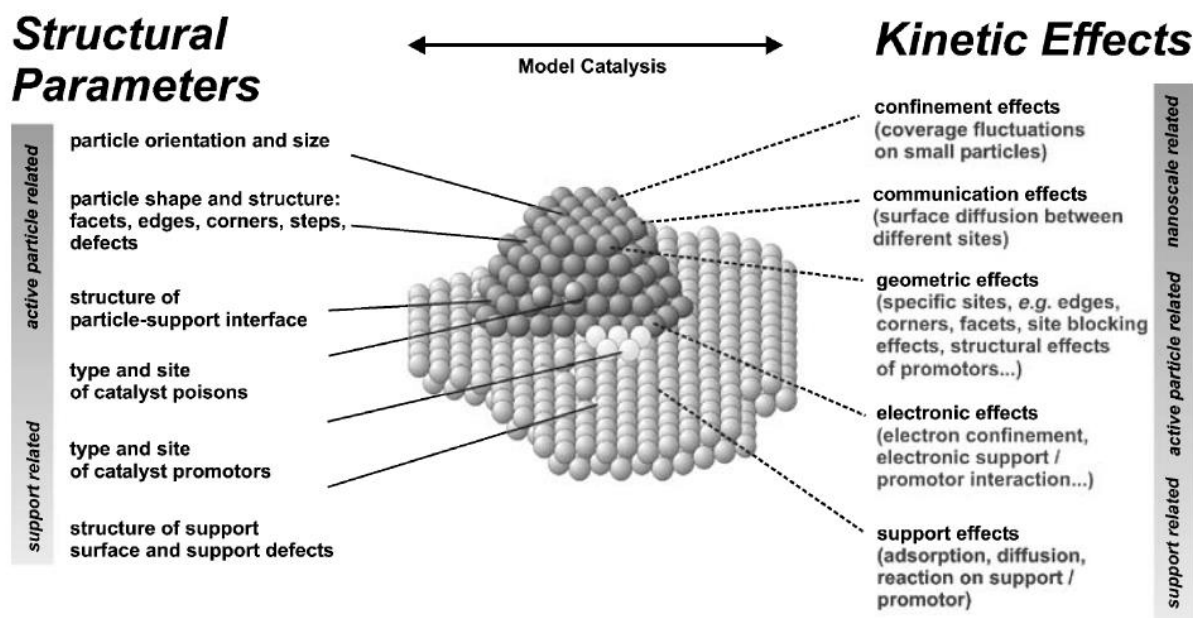
Figure 5: Structural parameters of the model catalyst with the controlled complexity and their relation to physical and chemical processes determining the catalytic action of the supported metal catalyst. Adapted from Ref. [26].

2.2 Quantitative morphological information in model catalysis

Central experimental techniques of surface science are space-averaging providing information on the sample properties from a characteristic area of approximately 1 mm². These techniques provide complex information on the surface and adsorbate crystallography (low- or high energy electron diffraction– LEED, RHEED [27]–[29]), on the surface and adsorbate chemical composition and chemical state (photoelectron spectroscopy – PS [30], [31]), or on the products and kinetics of the surface chemical reactions (temperature programmed desorption – TPD [32], [33], molecular beams – MB [34], [35]). Information on the sample morphology yielded by these techniques is however indirect.

The availability of high resolution bulk and surface imaging methods – electron microscopy [36], scanning tunneling microscopy [37], [38], and atomic force microscopy [39] allowed to view the morphology of the model catalysts in real space with atomic resolution and to quantify the morphological information. Studies that relate the quantified morphological information to the reactivity of the model catalysts maximize the insight in the elementary catalytic processes, and the impact on the overall advance in the field. Prototypical studies quantifying the density of different surface defects [40], the coverage of the active phase [41], and the size of the metal clusters in supported metal catalysts [42] are presented in Figures 6-9.
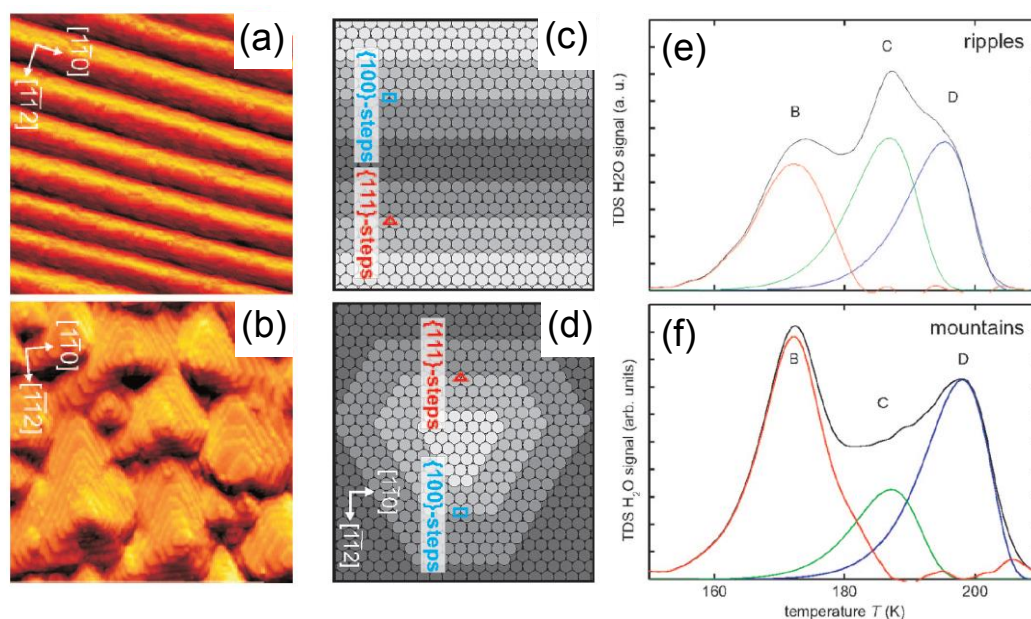
Figure 6: Quantification of the step density of different step types. (a, b) STM of different step architectures on Pt(111) surface – "ripples" prepared by ion bombardment (a) and "mountains" prepared by by Pt homoepitaxy (b). STM image width 90 nm. (c, d) Schematic of the model Pt(111) surfaces. "Ripples" on model Pt(111) surface contain equal proportion of two types of steps, (100)-step and (111)-step (c). "Mountains" on model Pt(111) surface contain a majority of (111)-steps (d). (e, f) TPD of H_2O from model Pt(111) surfaces. The intensity of the three desorption peaks (B, C, D – red, green and blue curves) corresponds to the surface density of different adsorption sites on the model Pt(111) surfaces. B – Pt(111) terrace, C- (111)-step, D – (100)-step. This prototypical study resolves different adsorption sites for H_2O molecule on Pt(111) surface complementing the picture of water chemistry on Pt surface [43]. Adapted from Ref. [40].
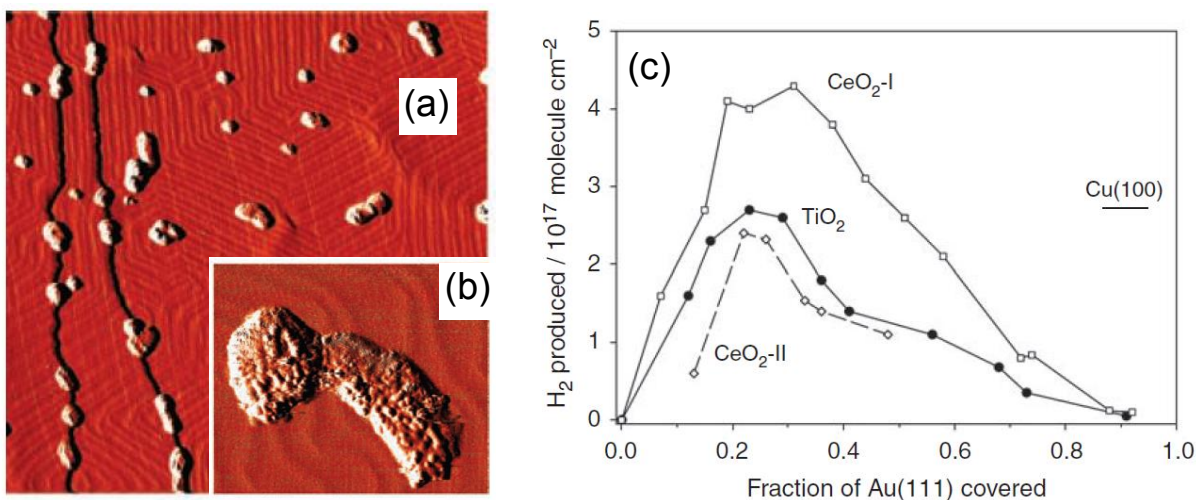
Figure 7: Quantification of the coverage of the active phase. (a, b) STM of CeO_2 clusters on Au(111) surface – example of model catalyst in so called inverse layout [44]. The coverage is determined as the fraction of the metal substrate covered by the oxide. STM image width (a) 200 nm, (b) 30 nm. (c) H_2 yield of the water-gas shift reaction over the CeO_2/Au(111) and TiO_2/Au(111) model catalysts. H_2 yield exhibits a maximum for oxide coverage of approximately 30 % rendering the metal-oxide boundary as an active site for the water-gas shift reaction [45]. This prototypical study ultimately resulted in designing of a new class of industrial inverse catalysts for water-gas shift reaction [46]. Adapted from Ref. [41].
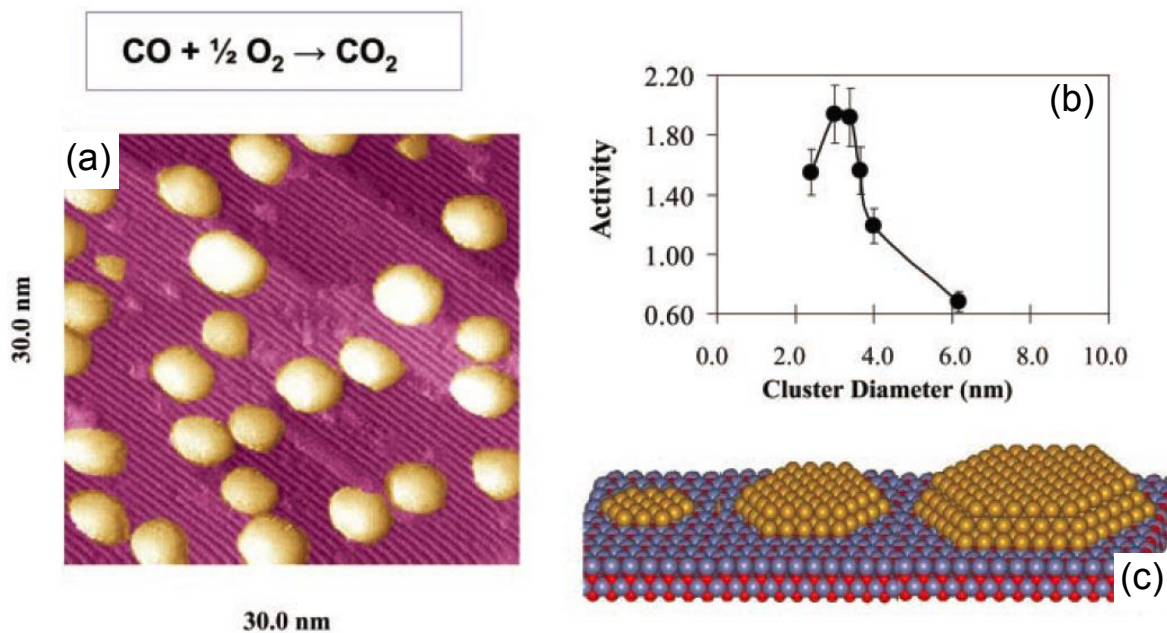
Figure 8: Quantification of the size of the supported metal clusters. (a) STM of Au clusters on TiO_2(110). (b) CO_2 yield exhibits a maximum for the diameter of Au clusters approximately 3 nm corresponding to a situation when the Au clusters are formed less than 3 monolayers thick and are becoming nonmetallic [42], (c). This prototypical study brought microscopic insight into the intriguing phenomenon of catalysis by gold when gold nanoparticles exhibit catalytic activity in spite of the fact that gold, generally, is catalytically inactive [47]. Adapted from Ref. [42].

7

2.3   Model catalysis in the Surface Physics Group

The Surface Physics Group at the Charles University in Prague, under the guidance of Professor Vladimír Matolín, is an active player in the field of model and real heterogeneous catalysis. Investigations performed in the Surface Physics Group contributed to understanding of several important concepts in the supported metal catalysis, mainly the metal-support interactions [48], [49], and the metal-support spillover effects [50] (cf. Figure 5). Initially, the focus of the investigations were metal clusters on nominally inert oxide supports (Pd/Al$_2$O$_3$). Recently, the focus transferred to metals supported on reducible oxide supports, where the metal-support interactions and the activity of the support alone are the central phenomena influencing the activity.

Most investigated are currently metal/CeO$_2$ model and real catalytic systems. The model catalysis over CeO$_2$ (ceria) has developed based on a successful preparation of model ceria system in the form of oriented CeO$_2$(111) thin film on Cu(111) single crystalline support [51] that allowed performing model studies on the different types of interaction between ceria and metal deposits, particularly Au [52], [53], Sn [54] or W [55].

Parallel to model catalytic studies, the Surface Physics Group is developing techniques for preparing real metal/ceria catalysts by physical methods [56], [57]. Professor Vladimír Matolín holds a range of international patents on preparation of Pt-ceria catalysts by scalable planar methods of magnetron sputtering compatible with industrial fabrication of thin films and semiconductors [58]. The methods of magnetron sputtering allow preparing highly active Pt/ceria catalysts for use in Polymer Electrolyte Membrane Fuel Cells (PEMFCs) where they exhibit an exceptional activity with a very low load of Pt metal bringing the PEMFC technology even closer to applications [57], [59]–[61]. At present, the methods of magnetron sputtering are further exploited for activation of the fuel cell catalysts [62]–[64] and the technology is being adopted on both electrodes of the PEMFC with excellent results in reducing the Pt load without sacrificing the fuel cell activity [65].

The characterization of the model as well as real catalysts in the Surface Physics Group traditionally relied on the space-averaging experimental methods of surface science, TPD [48], [49], MB [48], LEED [51], and RHEED [66], combined with photoelectron spectroscopy as the main experimental method. The Surface Physics Group significantly contributed to development of photoelectron spectroscopy methods in model catalysis, predominantly to methods allowing detailed investigations of the chemical state of model catalysts. Important PS methods developed in the Surface Physics Group allow determining the degree of reduction of the ceria supports by laboratory X-ray PS (XPS) [54], determining the degree of reduction of the ceria supports by highly sensitive resonance PS (RPES) [67], studying buried interfaces in heterogeneous catalysts by high-energy PS (HAXPES) [68], and observing the changes of the electron structure of model catalytic systems by angle-resolved PS (ARPES) [69].

In model catalytic studies, the information on the morphology of the investigated model catalysts in the Surface Physics Group was obtained indirectly from the space-averaging experimental methods of surface science. A direct, atomically resolved view of the morphology of the model catalysts has been obtained after installation and application of the experimental technique of STM. The consequences of this extension of the model catalytic research in the Surface Physics Group, and the resulting model catalytic studies based on the quantitative morphological information obtained from STM are described in the present Thesis.

3 Scanning tunneling microscopy

Scanning Tunneling Microscope is an electromechanical device measuring, in the first approximation, the height profile of surfaces of solid samples. The surface is scanned with a sharp tip at a small distance allowing for the flow of electrons between the sample and the tip via quantum tunneling (Figure 9). The parameters of the tunneling contact are the order of 1 nm width, 1 V sample bias, and 1 nA tunneling current. STM is capable of delivering images of the surface with details on the atomic scale [37] on samples with finite conductivity allowing for the passage of the tunneling current.

The tunneling current flowing between the tip and the sample is predominantly determined by the electronic structure of the valence and the conduction bands of the sample [70]. STM can thus yield information on the electronic structure of the sample via analysis of the current-voltage characteristic of the tunneling junction, so called Scanning Tunneling Spectroscopy (STS) [71], [72]. The possibilities to move and arrange atoms and molecules by the tip of the STM [73] and to perform vibrational spectroscopy on the molecules in the tunneling junction [74] broaden the spectrum of experimental techniques available in the scanning tunneling microscope and render the STM as an effective nanolaboratory (Figure 9).
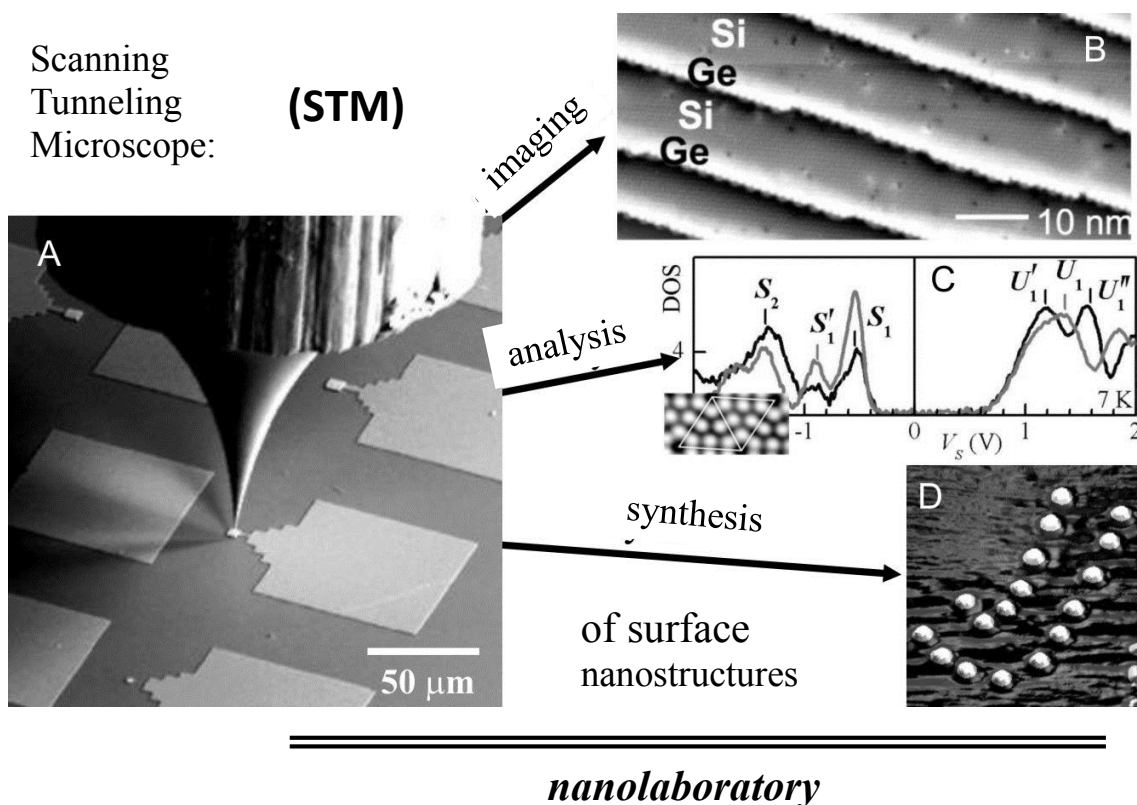
Figure 9: (A) Tip and sample arrangement in the Scanning Tunneling Microscope. (B-D) Experimental techniques available in the STM – microscopy, spectroscopy, and nanostructuring. Illustration from the undergraduate course NEVF140 – Surface Properties of Solids. Josef Mysliveček, MFF UK Praha.

3.1 Implementation in the Surface Physics Group

For the quantitative characterization of the morphology of model catalyst samples we have adapted a STM measuring head manufactured by CreaTec Fischer & Co. GmbH, Erligheim, Germany [75]. The STM head is so called "beetle" type [76], [77] (Figure 10). The STM head has been mounted on a homemade LN$_2$ cryostat allowing besides measurements at room temperature also measurements at 100 K. For STM control and data acquisition we have built a homemade control unit based on the design of, and controlled by the software developed by Doc. RNDr. Pavel Sobotík, CSc. (MFF UK). The control unit and the control software allow advanced STM and STS measurements [78]–[80].
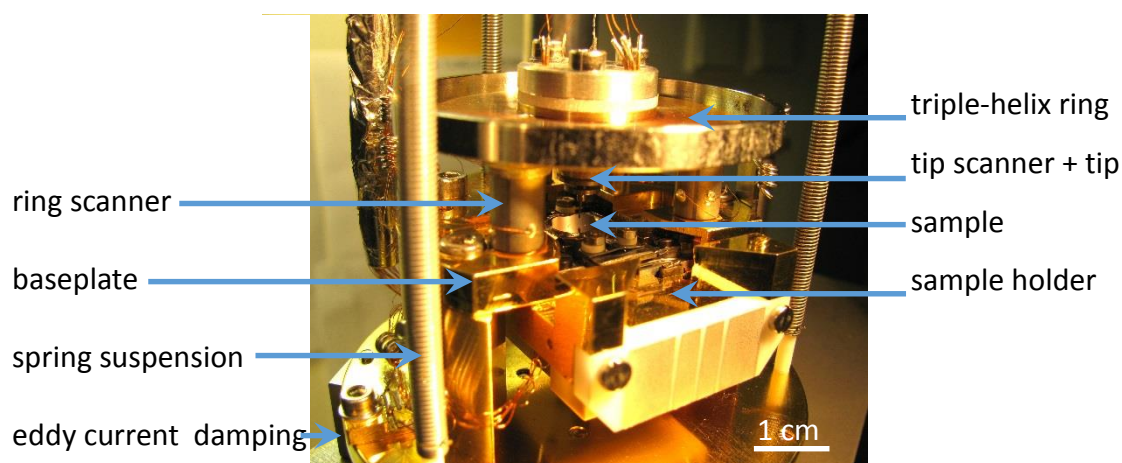
Figure 10: STM "beetle" type measuring head used in the Surface Physics Group.

The STM has been integrated in a newly built ultra-high vacuum (UHV) apparatus allowing characterization of samples, parallel to STM, by the key space-averaging experimental methods of surface science, TPD, MB, LEED, and laboratory XPS (Figure 11). The samples are prepared and characterized by all available methods "in-situ", i.e. without exposing the samples to air for transport between the methods. Uniquely in the Czech Republic, our apparatus thus allows correlating the information on the surface and adsorbate structure and chemical composition of model catalysts, and on the products and kinetics of the surface chemical reactions, with the quantitative morphological information resulting in advanced high-impact model catalytic studies.

3.2 Quantifying the morphological information

In the present Thesis, the observed morphological quantities on model catalyst samples are the density of monoatomic steps and the density and the size distribution of supported clusters. Example STM topographical images corresponding to a stepped model catalyst surface and the model catalyst surface with supported clusters are shown on Figure 12. The employed methods for quantifying the morphological information are partly automated, however, the identification of the morphological phenomena in STM images (steps, clusters) remains mostly manual. In spite of the advances in the automated image recognition, imperfections and artefacts of the STM imaging currently prevent fully automated recognition of most morphological features on model catalysts.

Figure 11: Apparatus integrating STM, XPS, LEED, TPD and MB experimental techniques for obtaining a complex view of the morphology and the physicochemical properties of model catalysts. Page from the 2014 calendar celebrating the 60th anniversary of the Department of the Surface and Plasma Science, the home to the Surface Physics Group.
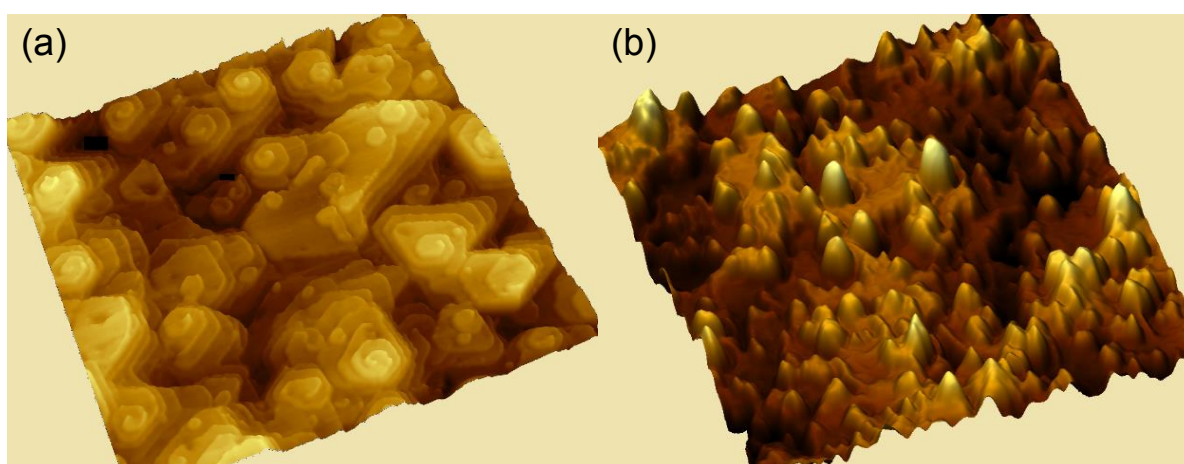
Figure 12: Morphologies of (a) stepped model catalyst surface and (b) the surface with supported metal clusters. (a) CeO_2(111) surface with threading dislocations, 250 × 250 nm^2. (b) CeO_2(111) surface with 0.1 ML of deposited Pt, 35 × 35 nm^2.

For determining the step density, we have developed a semi-automated procedure when first step outlines are marked in STM images manually. These outlines are then mapped onto a properly scaled and rotated mesh of surface atoms and the atoms that are closest to the outlines are automatically identified and considered step-edge atoms. Thus, step-edge atoms and their density in monolayers (ML) are calculated directly without the need of calibration and conversion from total step length per unit area. Sample output of the procedure is displayed in Figure 13.
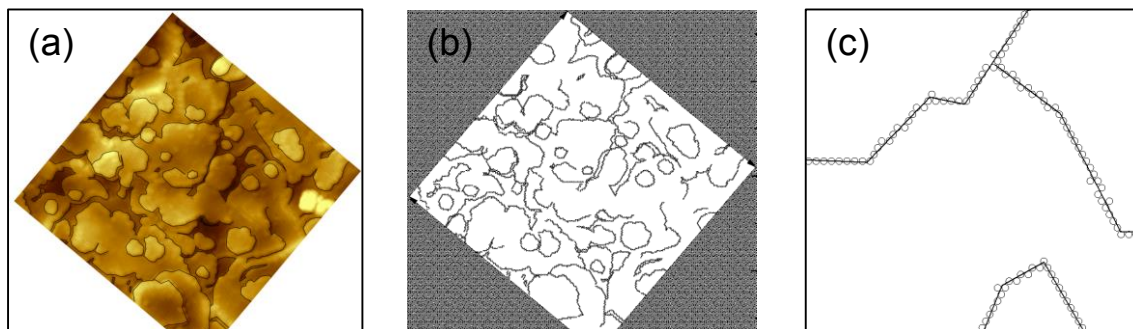
Figure 13: Illustration of the semi-automated procedure for determining the step density. (a) Manual outline of steps in the STM image (b) automated mapping of the outline on the idealized mesh of surface atoms (c) detail of the mapping output.

For determining the morphological properties of populations of supported metal clusters, automated procedures for grain recognition and grain statistics available in microscopy software packages may be used [81]. The analysis of STM images must take into account a significant lateral broadening of the detected clusters due to a finite diameter of the STM tip. Since the tip shape is generally unknown the analysis can be complemented with an independent experimental input. For cluster populations prepared by vacuum deposition in our experimental apparatus (Figure 11), the complementary information is the total weight of the deposit determined by Quartz Crystal Microbalance (QCM) [82] with resolution better than 1 per cent of a monolayer. The automated analysis of a cluster population and subsequent correction of the result for the total deposited amount of material is illustrated in Figure 14.

Automated software procedures provide detailed analysis of the density and size distribution of the clusters when supported on sufficiently flat substrate. For clusters on supports with complex morphology (cf. Figure 12 b) manual identification and quantification of the clusters remains the most effective method.
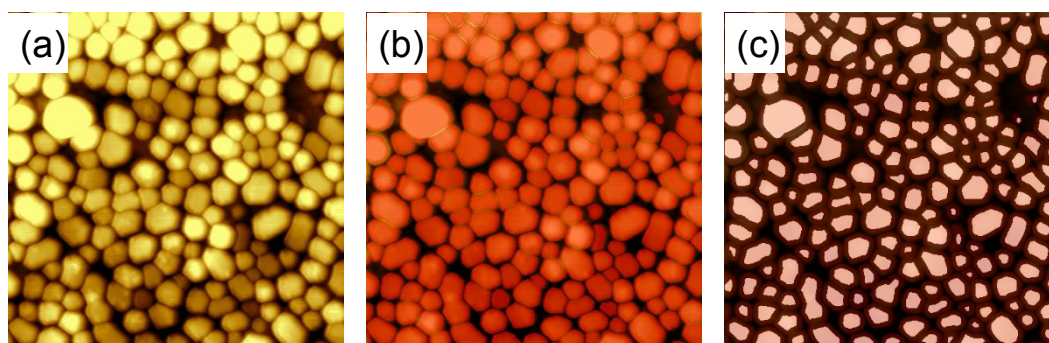
Figure 14: Illustration of the automated procedure for determining the statistics of Pt cluster population. (a) STM of 1.5 ML of Pt supported on $CeO_2(111)$, 60×60 nm^2. (b) Automated detection of clusters [81], (c) correction of the cluster sizes for the total amount of Pt determined by QCM.

3.3 Surface electronic structure

Besides imaging of the surface morphology, STM provides a possibility to determine the electronic structure of the samples via STS. Compared to the standard technique of PS for obtaining the electronic structure STS provides local information measured at the position of the STM tip, and information on both the occupied and unoccupied electron states of the sample. On the other hand, STS is limited in the energy of the investigated electron states to less than approximately 5 eV above or below the Fermi level, sufficient for investigations of valence and conduction bands, but with no access to core level electron states.

We demonstrate the spatial resolution of surface electronic spectra in an experimental study of the Si(111)-7×7 surface [83], Appendix 1. The Si(111)-7×7 surface represents one of the reference surfaces in surface physics, being the first surface to be imaged by STM with atomic resolution [84] and the first surface where spatially resolved STS has been demonstrated [85]. Easily prepared and imaged in STM, the Si(111)-7×7 surface is used to calibrate the magnification of STMs.

The Si(111)-7×7 surface contains several distinct adsorption positions related to the broken Si-Si bonds on the Si(111) surface and to the 7×7 reconstruction (Figure 15 a, b). In STS, each of these positions yields a characteristic STS spectrum revealing the spatial localization of the observed electron states (Figure 15 c). The imaging capability of the STM allows scanning the surface and mapping the spatial intensity of the individual electron states resulting, effectively, in imaging the wavefunctions of the sample for different electron energies (Figure 16). Our study [83], Appendix 1, improved the energy resolution of STS on the Si(111)-7×7 surface, and has become a reference for STS on the Si(111)-7×7 surface [86], [87]. For their illustrative qualities, the images from our study (Figures 15, 16) have been included and serve as an example of STS in a classical textbook on STM technique, "Introduction to Scanning Tunneling Microscopy" by C. J. Chen [88]. In model catalytic studies, STS is being used for investigations of electronic structure of active sites on model catalyst surfaces – supported clusters [42], linear [89] and point defects [90].
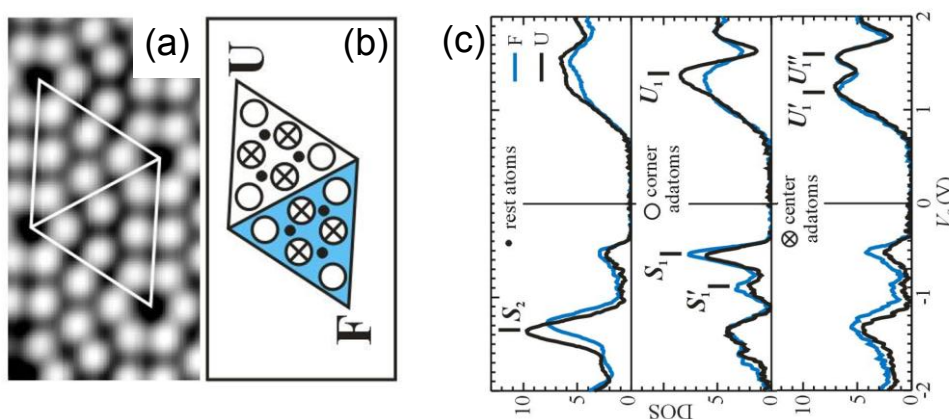
Figure 15: Spatially resolved STS electronic spectra. (a) STM of the Si(111)-7×7 surface with outlined two half-unit cells. (b) Schematic of the surface adsorption positions and their localization in the faulted (F) and unfaulted (U) half- unit cells. Restatoms – dots, corner adatoms – empty circles and center adatoms – crossed circles. (c) STS spectra measured at different adsorption positions assigning the localized electron states to rest atoms (S_2), corner adatoms (S_1', S_1, U_1), and center adatoms (U_1', U_1''). Adapted from Ref. [83], Appendix 1.
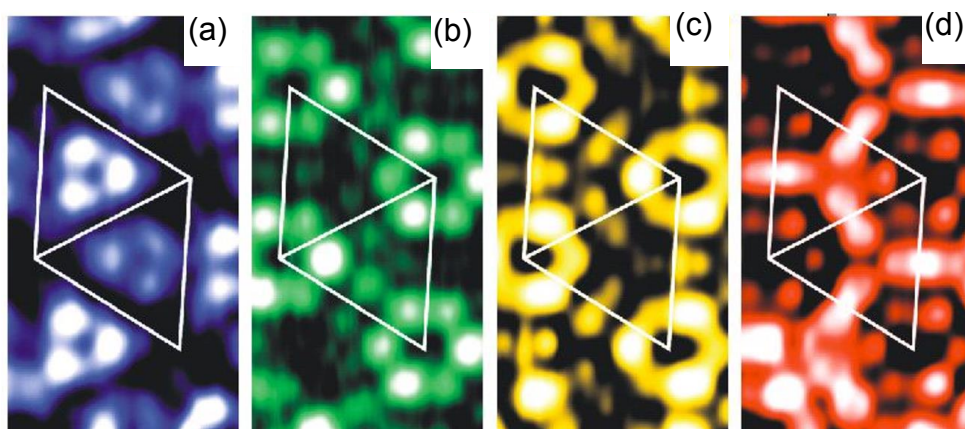
Figure 16: STS spatial maps of the electron states from Figure 15. Occupied states (a) rest atoms – S_2, (b) faulted corner adatoms – S_1, unoccupied states (c) unfaulted corner adatoms – U_1, (d) center adatoms – U_1''. Adapted from Ref. [83], Appendix 1. S_1, S_2, U_1, and U_1'' are defined in Figure 15.

3.4   Chemical contrast in the STM

For model catalytic studies, obtaining chemical contrast in a local microscopy technique represents a very desirable feature. In STM the tunneling current I_t is mostly influenced by the local density of states (LDOS) of the sample and the local height of the tunneling barrier ϕ. However, both LDOS and ϕ are lacking the chemical specificity in most cases. Electron states relevant for the STM lie within 5 eV from the surface Fermi level in valence and/or conduction bands, where the large energy shifts due to delocalization and hybridization prevent identifying energy levels of single atoms. The local tunneling barrier is modified by a charge redistribution between the surface and the bulk and can be affected by the presence of different surface atoms, however, with little relation to their chemical nature. Obtaining chemical information in STM measurements is thus more an exception than the rule.

We have illustrated the origin of the chemical contrast in STM in an experimental study of Bi terminated Si(111)-√3×√3-Bi surface [91], Appendix 2. On the Si(111)-√3×√3-Bi surface, deposition of Ge results in formation of two-dimensional, Bi terminated Ge-Si nanostructures that can act as nanowires [92] or as templates for self-organized growth of supported nanostructures [93]. The Ge-Si nanostructures (Figure 17 a) exhibit distinct, tunneling voltage-dependent STM contrast (Figure 17 b, c). Detailed measurements of STS spectra (Figure 17 d) and effects related to the tunneling barrier ϕ (Figure 17 e, f) identify contributions of both LDOS and ϕ of the Ge and Si terminated areas to the chemical contrast.

Although reasonably well understood, the chemical contrast in STM, when available, only reveals the spatial distribution of different chemical phases on the sample surface [94]–[96]. The chemical identification of the phases must be accomplished by other means. With model catalyst samples, the most straightforward method is a stepwise preparation of the samples by subsequent deposition of selected chemical species with STM observations after each deposition step identifying the morphology, and, eventually, the chemical contrast of individual chemical phases. For analysis of the sample chemical composition, complementary PS measurements are routinely performed.
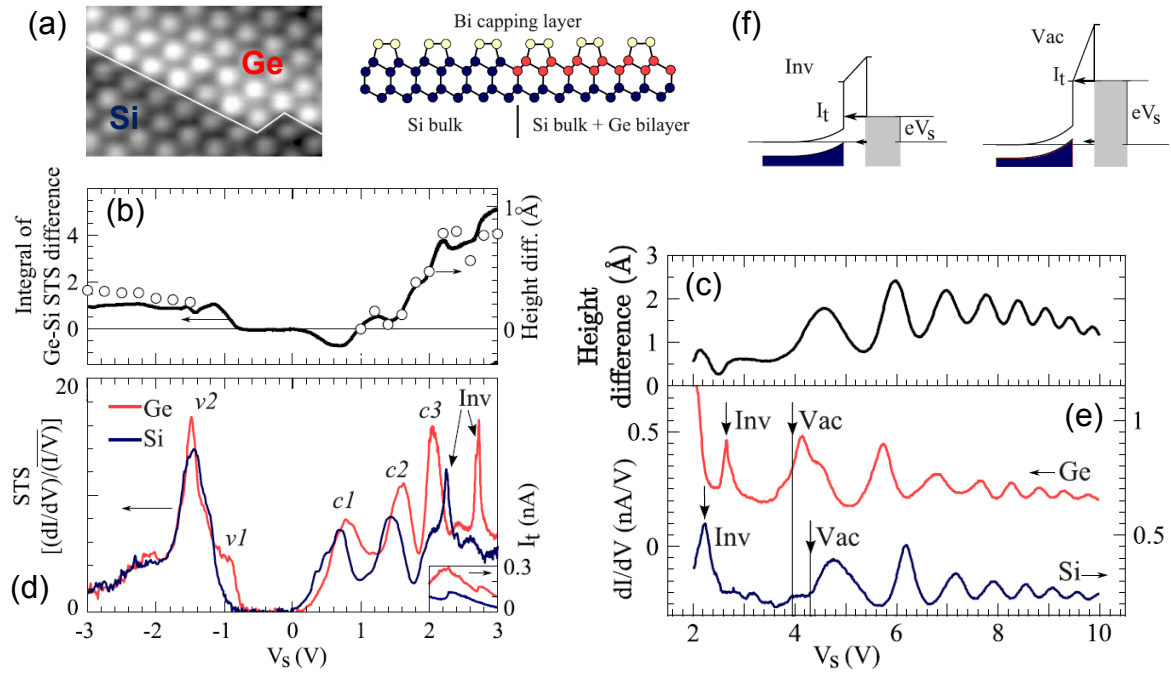
Figure 17: Chemical contrast in STM of Ge-Si nanostructures on the Si(111)-√3×√3-Bi surface. (a) STM and schematic side view of the boundary between Ge and Si-terminated areas on the Si(111)-√3×√3-Bi surface. STM image width 5 nm. (b, c) tunneling voltage-dependent height difference between Ge and Si-terminated areas for tunneling voltage $V_s \in (-3, 3)$ V (b) and $V_s \in (2, 10)$ V (c). (d, e) Normalized (STS, d) and plain (e) differential conductivity of the tunneling contact over Ge and Si-terminated areas. Differences of the electronic structure of Ge and Si-terminated areas (electron states v_1, v_2, c_1-c_3) determine the height difference at low V_s between -3 V and 2 V. Above 2 V, the height difference is dominated by non-LDOS features due to penetration of the electric field of the tip in the sample and consequent band bending. (f) "Inv" denotes tip induced inversion in the sample, "Vac" denotes crossing of the sample vacuum level by tip Fermi level. The positions of "Inv" and "Vac" differ on Ge and Si-terminated areas due to more efficient screening of the electric field of the tip on Ge areas. Adapted from Ref. [91], Appendix 2.

3.5 Molecules in the tunneling contact

STM can image and investigate the properties of individual molecules in the tunneling contact, i.e. the molecules adsorbed at the sample surface under the position of the tip. Particularly, the tunneling electrons passing the molecule between the sample and the tip can undergo an inelastic energy loss towards a vibrational state of the molecule. Similarly to STS, the inelastic losses can be determined by analysis of the current-voltage characteristic of the tunneling junction, so called Inelastic Electron Tunneling Spectroscopy (IETS, [74]).

We demonstrate IETS on individual molecules in an experimental study of endohedrally doped fullerenes $Ce_2@C_{80}$ adsorbed on Cu(111) [97], Appendix 3. In this study, we have detected besides the vibrations of the C_{80} cage also the low-energy vibrations associated with movements of the Ce atoms encapsulated inside the C_{80} cage (Figure 18). Our study proved that the vibrations of the encapsulated atoms in the endohedral fullerene may be active in determining the properties of molecular junctions.
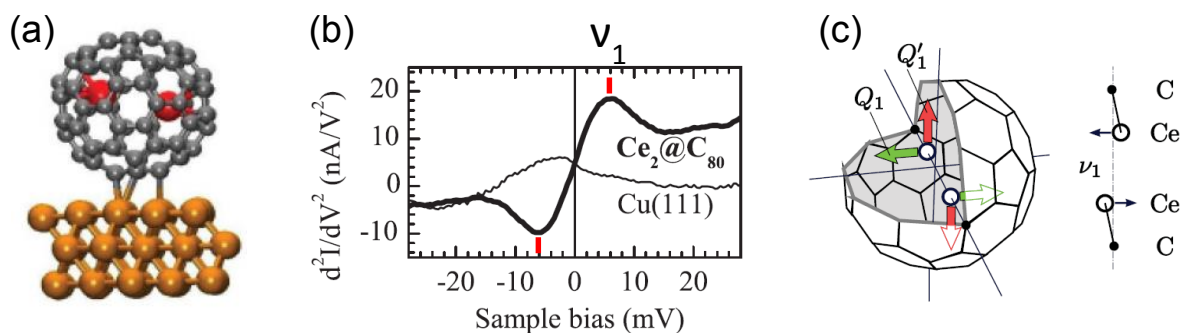
Figure 18: Inelastic electron tunneling spectroscopy of a molecule in the tunneling contact. (a) schematic of a $Ce_2@C_{80}$ molecule on Cu(111). (b) Antisymmetric peak at $|V_s|$ = 6 mV in the second derivative of the current-to-voltage characteristic of the tunneling junction indicates a low energy vibration v_1 of $Ce_2@C_{80}$. (c) Schematic of the v_1 vibration of the Ce atoms encapsulated in the C_{80} cage. Adapted from Ref. [98], Appendix 3.

In model catalytic studies, detection of molecular vibrations by IETS has been performed for identification of the products and intermediates in several outstanding fundamental studies of the elementary surface chemical reactions [99], [100], but due to the extreme requirements on the stability of the experiment [74], employing IETS in model catalytic studies is rare.

In numerous model catalytic studies, on the other hand, simple topographic contrast of the adsorbed molecules is used to identify the adsorption positions of the molecules, or, for multiple adsorbed species, to discriminate different molecular species. We demonstrate the topographic contrast between two types of molecules, endohedral fullerene $Ce_2@C_{80}$, and plain fullerene C_{60} in Ref. [98], Appendix 4 (Figure 19). The molecules were identified in a two-step deposition experiment as described in Section 3.4. Unambiguous identification of the adsorbed molecules in STM is limited by the lacking chemical sensitivity of the method and significant misinterpretations may occur. On Figure 20 two interpretations of the same model catalytic system are presented [101], [102]. To prevent such situations extreme caution in preparing and interpretation of experiments employing topographic STM data on adsorbed molecules is required, with strong support of ab-initio calculations of the STM contrast [103].
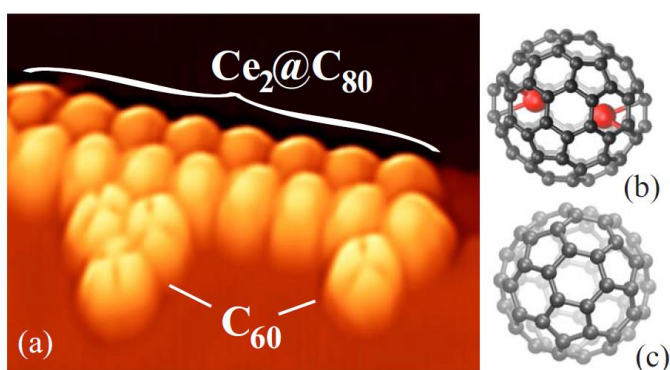
Figure 19: Topographic contrast of two molecular species adsorbed on Cu(111). (a) STM, image width 8 nm. (b) schematic of $Ce_2@C_{80}$, (c) of C_{60} molecules. From Ref. [98], Appendix 4.

Squares locate vacancy
sites, whereas circles locate O_2 molecules.

Protrusions are labeled as follows: O_{br} vacancies (open white
circles), OH_{br} groups (filled white circles), water on 5f-Ti sites
(filled black squares).
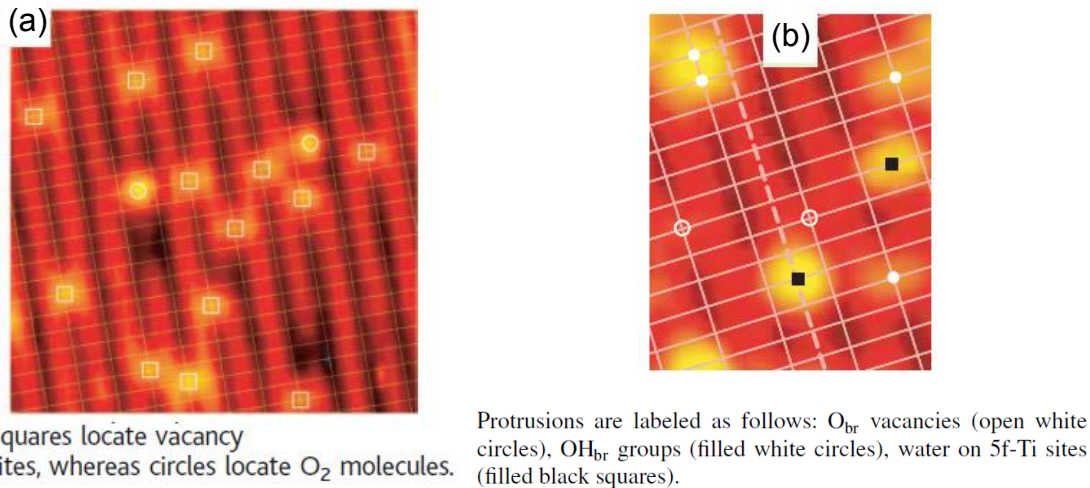
Figure 20: Ambiguous interpretation of the molecular topographic contrast on the model catalyst surface of rutile $TiO_2(110)$. (a) the original interpretation of molecular features on rutile $TiO_2(110)$ as oxygen vacancies and adsorbed O_2 [101], (b) corrected interpretation as surface hydroxyls and adsorbed H_2O [102].

4   Self-organization of surface nanostructures

For investigation of the relationships between the morphology and the reactivity of model catalysts experimental control of the morphology of the model catalysts is inevitable. In this respect, nanostructured model catalysts can be prepared with a desired morphology using self-organization phenomena taking place during growth of thin films on single-crystalline solid substrates [104]. Main parameters allowing the control of the morphology of model catalysts by self-organization are the material of the substrate, the deposition rate of the deposit, the amount of the deposit, and the thermal treatment of the sample prior, during, or after model catalyst deposition.

The material of the substrate determines the equilibrium morphology and so called growth mode of the thin film (Figure 21). The equilibrium growth of one phase (homoepitaxy, material of the substrate and of the deposit is the same) ideally proceeds by attaching the deposit material at monoatomic steps of the substrate and the substrate morphology is replicated by step flow [105], (Figure 21 a). In the case of two phases (heteroepitaxy, material of the substrate and of the deposit differ), depending on the mutual energetics of the substrate and deposit surfaces, step flow may be modified by nucleating islands after reaching a certain film thickness [106], or not take place at all in case the deposit is nucleating as three-dimensional (3D) islands from the beginning [107]. The morphology in equilibrium is dictated by minimization of the sample free energy, and the island surfaces may adopt different crystallographic structure and orientation than the substrate.
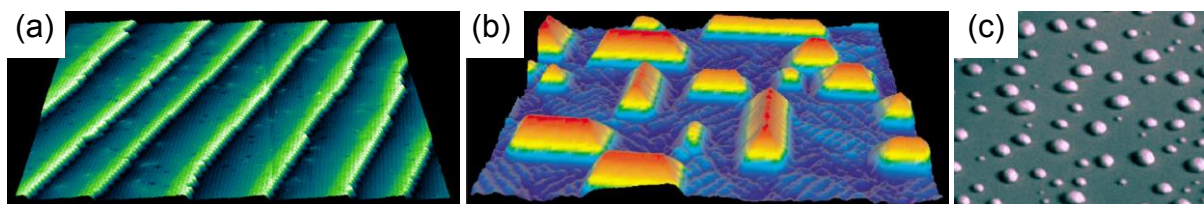
Figure 21: Equilibrium growth modes of thin films. (a) Step flow, Ge on Bi-terminated Si(111) adapted from Ref. [108]. (b) Stranski-Krastanov, Ge on Si(100), adapted from Ref. [109]. (c) Volmer-Weber, Pb on Ru(0001) adapted from Ref. [110]. Image width (a) 60 nm, (b) 130 nm, (c) 3000 nm.

17

Under non-equilibrium conditions, the morphology of the growing film is kinetically determined by a competition between the deposition rate F, at which new atoms or molecules of the deposit impinge at the substrate, and the diffusion rate of the atoms or molecules of the deposit on the surface of the substrate and of the growing thin film [111], [112]. Among different surface diffusion processes, the most important is the diffusion rate of the deposit on the atomically flat terraces of the substrate, D. Far from equilibrium, the competition gives rise to nucleation of islands on the terraces between the steps (Figure 22 a). The density of these islands n can be adjusted by adjusting F or D as $n=(F/D)^{\chi}$ with $\chi \leq 1$ [111], [113]. Islands nucleated far from equilibrium are typically one monolayer high and adopt the crystallographic orientation of the substrate. Subsequent growth of the thin film follows by lateral spreading of the islands and nucleation of new islands on top of the completed monolayers by so called layer-by-layer growth (Figure 22 b, c) [114], [115].
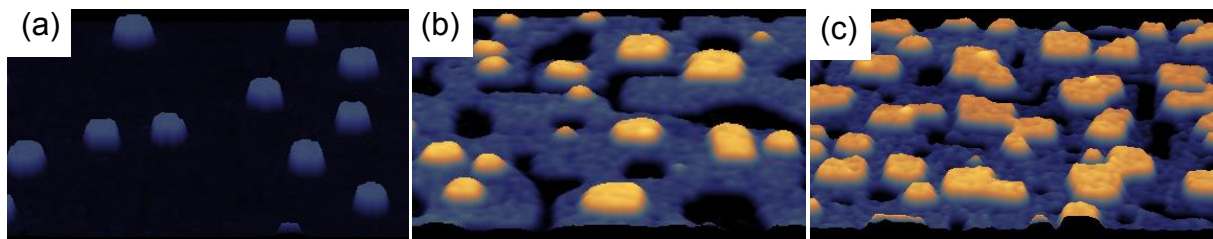
Figure 22: Non-equilibrium growth mode of thin films. Homoepitaxy of Fe(001). (a) Island nucleation, adapted from Ref. [116] (b), (c) layer-by-layer growth – Frank-van der Merwe, adapted from Ref. [115] (b), (c). Image width (a)-(c) 130 nm.

Further diffusion processes that determine the morphology of the thin films far from equilibrium are the diffusion of the deposit across or along the monoatomic step edges on the sample. The diffusion across the step edges is determining the rate of incorporation of the deposit from the upper and the lower terrace adjoining the step, and the stability of the step train during step flow growth. Predominant incorporation from the upper terrace destabilizes the step train against step bunching [117] (Figure 23 a), while the predominant incorporation from the lower terrace destabilizes the step train against step meandering [118] (Figure 23 b). The latter condition is related to the presence of so called Ehrlich-Schwoebel barrier at the step edges preventing the diffusing particles of the deposit from descending the monoatomic steps [112], [117]. The presence of the Ehrlich-Schwoebel barrier causes destabilization of the growth front also during layer-by-layer growth leading to formation of mounds [119] (Figure 32 c).
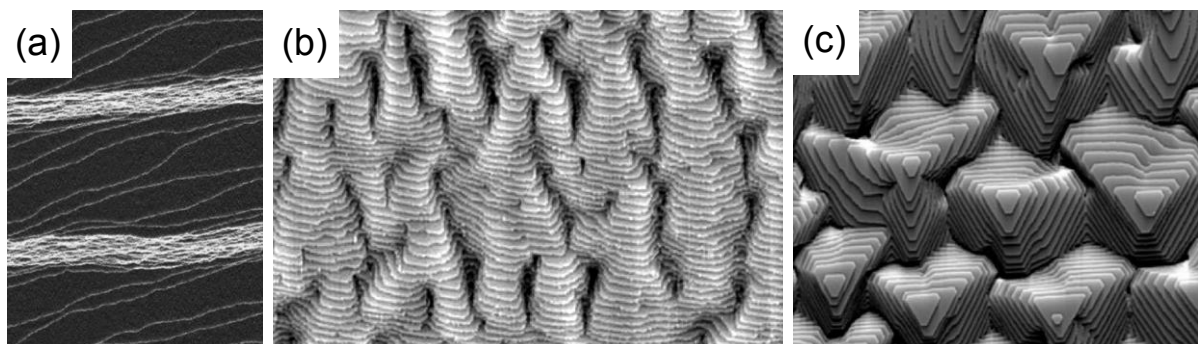
Figure 23: Growth instabilities due to barriers for crossing the step edge. (a) Step bunching during step flow growth. Homoepitaxy of InP(111), adapted from Ref. [120]. (b) Step meandering during step flow growth. Homoepitaxy of Cu(001), adapted from Ref. [121] (c) Growth of mounds destabilizing layer-by-layer growth. Homoepitaxy of Pt(111), adapted from Ref. [122]. Image width (a) 3000 nm, (b) 150 nm, (c) 250 nm.

The diffusion along the step edges is determining the morphology of the monoatomic steps propagating across the surface during growth. Step edges are compact (Figure 24 a) closer to equilibrium and become open – fractal (Figure 24 b) or dendritic (Figure 24 c), when the growth conditions depart from equilibrium [123].
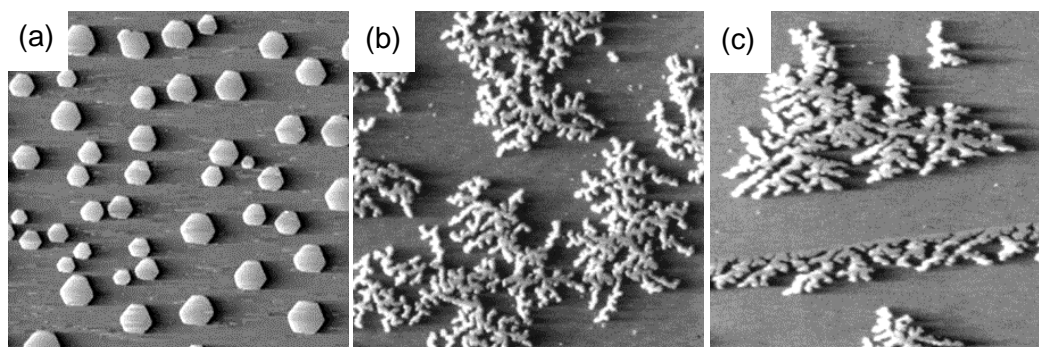
Figure 24: Growth instabilities due to barriers for diffusion along the step edge. (a) Compact islands closer to equilibrium, Pt(111) homoepitaxy, adapted from Ref. [124]. (b) Fractal islands, (c) dendritic islands far from equilibrium. (b), (c) Ag on Pt(111), adapted from Ref. [125]. Image width (a) 300 nm, (b), (c) 100 nm.

As we show in the following, further kinetic effects affecting the morphology of the growing thin films cat be identified giving the experimentalist a broad range of possibilities on how to adjust the morphology of thin film model catalysts by self-organization in a desired manner. Besides thin film growth, self-organization of the surface morphology may occur also during ion erosion of the surfaces that can be, to a certain extent, considered as a growth with negative deposition rate [124]. Directional ion erosion is used in model catalysis as a method for controlling the orientation of the monoatomic steps on model catalyst surfaces [40], [126].

## 4.1 Surface instability due to diffusion anisotropy

Many technologically relevant surfaces exhibit anisotropic surface structure and anisotropic physicochemical properties including anisotropic surface diffusion. A prominent representative of anisotropic surfaces is Si(001) [127]. The anisotropic 2×1 surface reconstruction forms so called dimer rows that rotate by 90° on each subsequent monoatomic terrace [128]. On vicinal Si(100) 2×1 miscut towards [110] direction this gives rise to two types of monoatomic steps alternating on the surface: step type A – S_A, with straight step edge parallel to dimer rows on the upper terrace (terrace type A), and step type B – S_B with jagged step edge perpendicular to dimer rows on the upper terrace (terrace B). A microscopic view of such Si(001) surface is displayed on Figure 25 a.

In Ref. [129] (Appendix 5) we prove that the anisotropic diffusion on Si(001) gives rise to step bunching instability (cf. Figure 23 a) observed in a narrow temperature range during Si homoepitaxy on Si(001) [130]. The explanation is based on the observation of morphology of vicinal Si(100) 2×1 surfaces. During homoepitaxy, the equilibrium structure of the Si(100) 2×1 surface as in Fig. 25 a persists only at high temperatures (Figure 25 b). Lowering the temperature during growth causes pairing of S_A and S_B steps and step flow of S_A-S_B step pairs [131] (Figure 25 b). In the presence of diffusion anisotropy in the model of Si(001) homoepitaxy S_A-S_B step pairs incorporate diffusing Si atoms from upper terraces more effectively than from lower terraces leading to step bunching (Figure 25 c, d) [129]. As a new and a generic instability the step bunching instability due to diffusion anisotropy on Si(001) has become a standard reference for growth instabilities observed in silicon-germanium, and, generally, semiconductor nanostructures [132], [133].
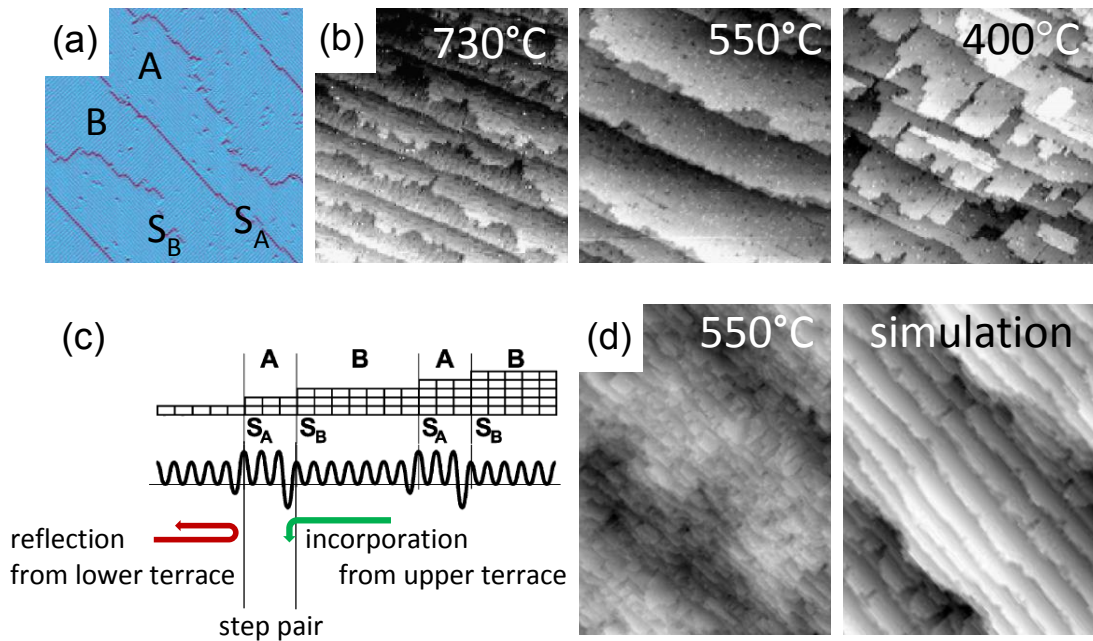
Figure 25: Step bunching instability due to diffusion anisotropy. (a) STM view of anisotropic Si(001)2×1 surface with A and B terraces and S_A and S_B step edges. Image width 50 nm. Adapted from Ref. [134]. (b) STM view of morphology during Si(001) homoepitaxy. At 550 °C, formation and step flow of S_A-S_B step pairs is observed. Image width 100 nm. (c) Diffusion potential for Si atom moving perpendicular to S_A-S_B step pair in the presence of diffusion anisotropy favors incorporation of diffusing Si atoms from the upper terraces. (d) This is causing step bunching instability observed in STM and reproduced in growth simulation using the anisotropic surface diffusion potential from (c). STM image width 300 nm. Figures (b)-(d) adapted from Ref. [129], Appendix 5.

4.2   Modification of growth kinetics via surfactants

Growth properties of a particular combination of substrate and thin film may be modified by depositing third species on the surface – a surfactant – that is floating on the surface of the growing thin film but is not incorporated into it. Surfactants are mainly used to influence the self-assembly of semiconductor nanostructures when the presence of the surfactant changes the growth mode of the system (cf. Figure 21), e.g. suppressing [135] or promoting [136] the formation of 3D islands.

In Ref. [137] (Appendix 6) we demonstrate how the surfactant influences the morphology of 2D island populations (cf. Figure 22 a) in Ge/Si heteroepitaxy. We prepare populations of 2D Ge islands on Si(111) in the presence of Bi surfactant (Figure 26 a) and quantify the island size distribution of the Ge islands (Figure 26 b). We observe that at low temperatures, the normalized Ge island size distribution deviates from island size distribution predicted by a standard growth model [116] changing from a peaked to a monotonous function. To understand this behavior at the atomic level we perform simulations of surfactant mediated epitaxy considering thermally activated processes of exchange and deexchange [138] that are not present in the standard model [116] and represent the transport of the deposited material through the surfactant layer (Figure 26 c). We conclude that the processes of exchange and deexchange can hinder the incorporation of deposited material at the step edges of the growing islands and modify the island size distribution in surfactant mediated epitaxy as observed in our experiment (Figure 26 d, e). The slow incorporation of deposited material at the step edges causes collapse of the depletion zones around nucleating islands [139] resulting in uncorrelated random nucleation of 2D islands and the monotonous size distribution.
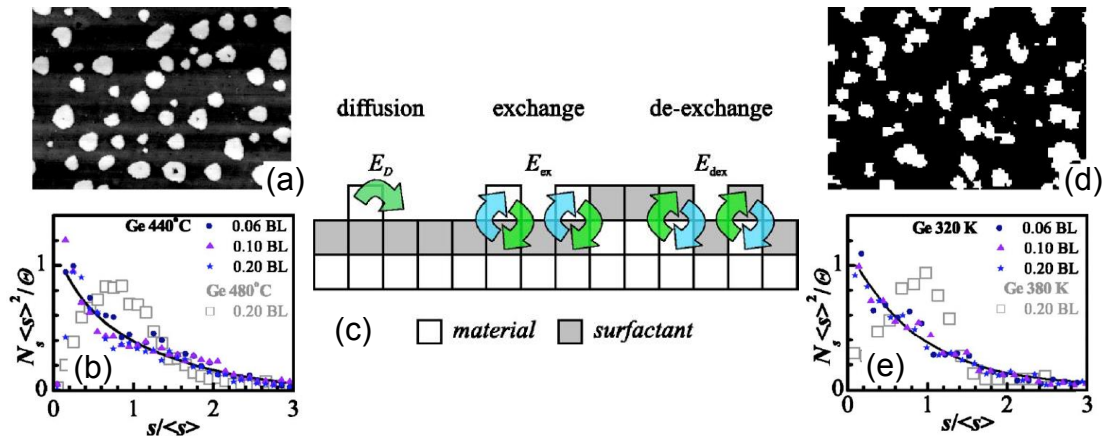
Figure 26: Influence of surfactant on the nucleation of 2D islands. (a) surfactant mediated epitaxy of Ge on Si(111) with Bi as a surfactant. (b) Normalized island size distribution of Ge islands as a function of temperature (color symbols denote lower temperature than grayscale symbols). (c) Atomic-level kinetic processes considered in the simulation of surfactant mediated epitaxy. (d, e) Morphology (d) and normalized island size distribution (e) obtained from the simulation of surfactant mediated epitaxy. Adapted from Ref [137], Appendix 6.

In a standard application of surfactant mediated epitaxy the surfactant is deposited at the surface using deposition parameters that maintain 100% coverage of the sample by the surfactant during thin film growth. In Ref [108] (Appendix 7) we have demonstrated that such strategy may be detrimental for stabilization of certain surface nanostructures. Particularly, surfactant mediated epitaxy allows fabrication of Ge/Si nanowires on Si(111) surfaces due to suppressing of Ge-Si intermixing [92]. At the same time, however, the presence of surfactant causes meandering of Si(111) step edges (Figure 27 a) and uneven decoration of the Si(111) step edges by Ge (Figure 27 b). In an attempt to prepare highly ordered Ge nanowires on highly ordered Si(111) surfaces we have developed a strategy when the amount of surfactant on the surface is temporarily reduced during critical steps of sample preparation and the ordering of the Si(111) is not disturbed (Figure 27 c, d). The presented works on surfactant mediated epitaxy have been reviewed as valid contributions to the theory and fabrication of semiconductor nanostructures [140]–[142].
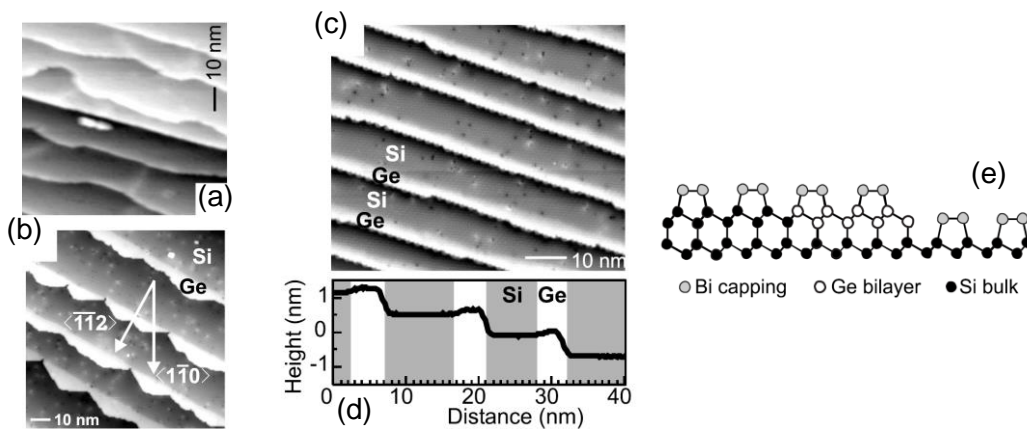
Figure 27: Surfactant coverage as an adjustable parameter during growth of surface nanostructures. (a) Step meandering on Si(111) fully covered by Bi surfactant. (b) Rotation of the growth front during step flow growth of Ge on Si(111) fully covered by Bi surfactant. (c-e) Atomically straight Ge nanowires on Si(111) prepared by step flow with intermittent reduction of Bi surfactant coverage. Adapted from Ref. [108], Appendix 7.

4.3   Metal clusters in surface superstructures

Nucleation of islands during growth of a thin film can be a result of minimization of the system free energy (Figure 21 b) [143] or a sign of growth far from equilibrium (Figure 22 a) [116]. In both cases, positions of the nucleated islands on the surface are random, with weak mutual correlations due to depletion zones [139] and/or modifications of the elastic strain [144] around the nucleated islands.

Spatially ordered nucleation of islands can be achieved on surfaces exhibiting ordered surface superstructures – regular long-range arrangements of surface atoms due to e.g. surface reconstruction [145] or a dislocation network [146]. We have studied nucleation of Ag on the Si(111) surface with 7×7 surface reconstruction [147], [148] (Appendices 8, 9).

The 7×7 reconstruction of Si(111) [84], [149] forms a large surface unit cell composed of 2.7 nm wide triangular parts – faulted and unfaulted half-unit cells (Figure 15 a). Upon deposition of Ag, three types of objects are identified in STM, denoted A-C (Figure 28 a) [147], Appendix 8. Statistical analysis of the object density reveals that the objects are Ag monomers (A), Ag dimers (B) and Ag clusters of 3 or more atoms (C) (Figure 28 b). The delocalized appearance of Ag monomers and dimers together with a considerable lifetime (at room temperature) of Ag objects indicate that the half-unit cells of the 7×7 reconstructions act as traps for Ag atoms. Ag atoms can easily move inside the half-unit cells while the transport of Ag between the half-unit cells is much slower.
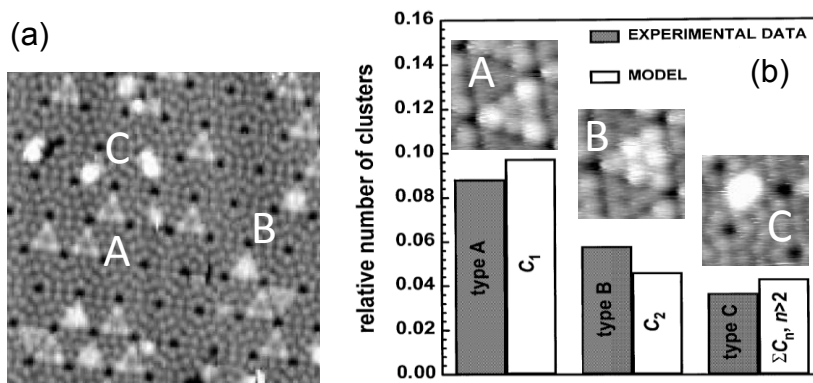
Figure 28: Nucleation of Ag on the Si(111)-7×7 surface. (a) Sample morphology with three types of Ag objects that can be identified. STM, image width 20 nm. (b) Detailed view of different Ag clusters and their corresponding densities in experiment (grey bars) and in a growth model (white bars). Adapted from Ref. [147], Appendix 8.

In order to capture the physics underlying the nucleation of Ag clusters on the Si(111)-7×7 surface we have proposed a coarse-grained model of Ag nucleation [148], Appendix 9. The coarse-graining approach focuses on the rate limiting processes taking place on the lateral scale of single half-unit cells – filling of half-unit cells by Ag atoms and transport of Ag atoms between half-unit cells – and neglects the fast processes taking place on the lateral scale of atoms – movements of Ag atoms inside half-unit cells. For determining the physical parameters of the coarse-grained model we have quantified the morphological parameters of Ag deposit on the Si(111)-7×7 surface for a range of preparation conditions – upon growth at different substrate temperatures and Ag deposition rate or upon annealing at different temperatures (Figure 29 a). Evaluated was the density of Ag clusters and the preference of Ag clusters to nucleate in the faulted half-unit cell (Figure 29 b, c, symbols). Fitting of the model outputs for the density of Ag clusters and the preference (Figure 29 b, c, lines) allowed to determine the activation energy for hopping of Ag atoms between half-unit cells E_d = 0.75 eV, the stability of Ag clusters with > 5 Ag atoms, and the capacity of the half-unit cell to accommodate ≈ 20

Ag atoms. In addition, the morphology of the samples was found to be influenced by a transient mobility of the impinging Ag atoms.
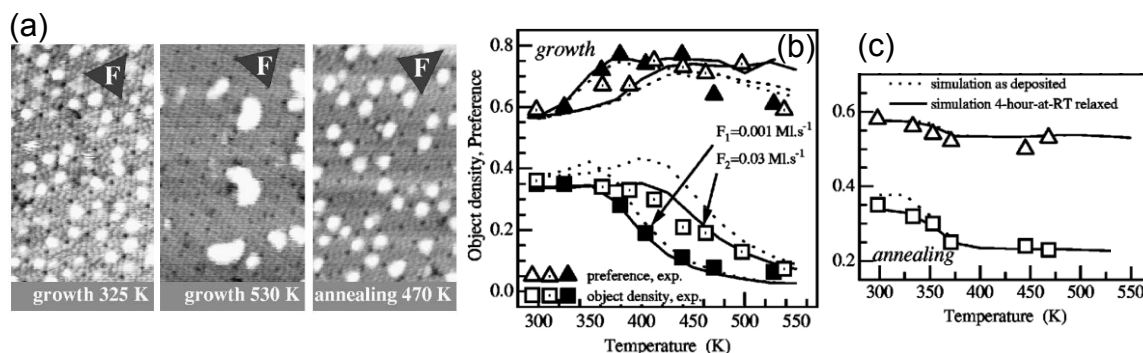
Figure 29: Morphological parameters and growth model of Ag deposit on the Si(111)-7×7 surface. (a) Morphology of Ag deposit upon different experimental treatments. Orientation of the faulted half-unit cell is marked by a black triangle. STM, image width 15 nm. (b, c) Evaluated morphological parameters (symbols) and outputs of the growth model (lines) for samples upon growth (b) or upon thermal annealing (c) of the Ag deposit. Adapted from Ref. [148], Appendix 9.

The presented analysis of nucleation of Ag on the Si(111)-7×7 surface has become a standard reference for the nucleation of metals on Si(111)-7×7 surface, in general [150], [151], and for optimization of metal cluster distribution on Si(111)-7×7 surface [152]. The coarse-grained approach to modeling of growth of metal clusters in surface superstructures was used, e.g., in a study of nucleation of metals on a superstructure formed by a graphene layer on Ir(111) substrate [153], Appendix 10.

Graphene [154] on iridium [155] and on other metal surfaces [156] forms Moiré superstructures with periodicity in single nm range due to the mismatch between the lattice constants of graphene and of the underlying metal (Figure 30 a). Similarly to the surface reconstruction of Si(111)- 7×7 surface triangular half-unit cells of the Moiré superstructure can accommodate metal clusters (Figure 30 b). Supported graphene can thus be used for fabricating large arrays of perfectly ordered metal clusters (Figure 30 c). Self-organization of metal clusters on graphene has become an important part of graphene physics [156], [157]. Generally, self-organization of metal clusters on surface superstructures represents an advanced technique for preparing model catalyst systems [25].
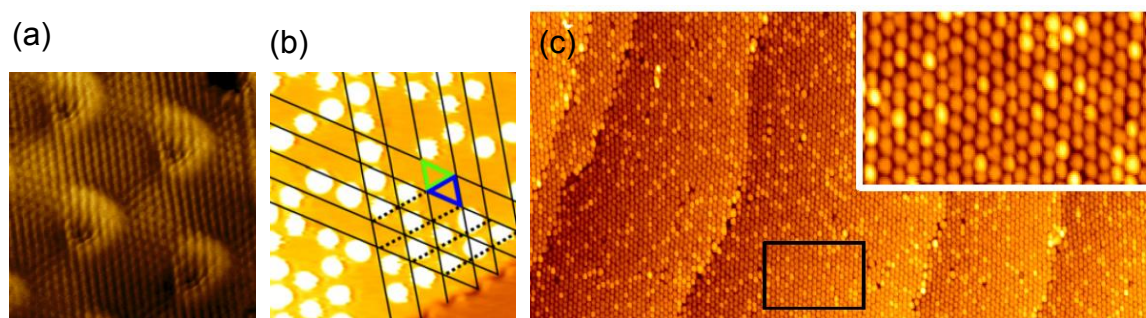
Figure 30: (a) Graphene on Ru(0001). STM of the Moiré superstructure. Image width 5 nm. Josef Mysliveček, unpublished results. (b) STM of nucleation of Pt on graphene/Ru(0001). Image width 20 nm. Unit cells of the surface superstructure are outlined black, triangular half-unit cells are marked green and blue. (c) STM of spatially extended array of Ir clusters on graphene/Ir(111). STM image width 250 nm, inset width 50 nm. Figures b, c adapted from Ref. [153], Appendix 10.

5   Model catalyst studies over Pt/ceria

Ceria based materials including ceria supported Pt find vast applications as heterogeneous catalysts [158]. They represent a main component of three-way automotive catalysts [159], [160] and catalyze a range of important chemical reactions in energy conversion, environmental protection, and production – hydrogen generation [161], water-gas shift [162], [163], selective catalytic reduction of NO [164], soot combustion [165], or a range of organic reactions [166]. Ceria based materials allow the development and investigations of perspective and intriguing catalytic phenomena – catalysis by gold [167], [168] or single-atom catalysis [169], [170]. Ceria also represents an important functional material in devices for energy conversion – solid electrolyte in high temperature and intermediate temperature solid oxide fuel cells [171], [172] or oxygen exchange material in thermochemical H_2O/CO_2 splitters [173], [174].

The Surface Physics Group at the Charles University in Prague is developing Pt-ceria catalysts for polymer electrolyte membrane fuel cells (PEMFC, Section 2.3). Preparation and properties of catalyst for hydrogen oxidation on the anode of the fuel cells are presented in Figure 31 (Ref. [59], Appendix 11). The catalysts are prepared by a patented method of magnetron sputtering [58] on high-area carbon substrates (Figure 31 a, b). A characteristic feature of these Pt-ceria catalysts is the presence of Pt in ionic states Pt^{2+} and Pt^{4+} (Figure 31 c). The catalysts show a high activity in power tests in fuel cells (Figure 31 d). Pt-ceria catalysts yield the power density comparable to the reference Pt/Ru catalysts, however with 3 orders-of-magnitude smaller Pt load promising a significant reduction of Pt load in the emarging PEMFC applications.
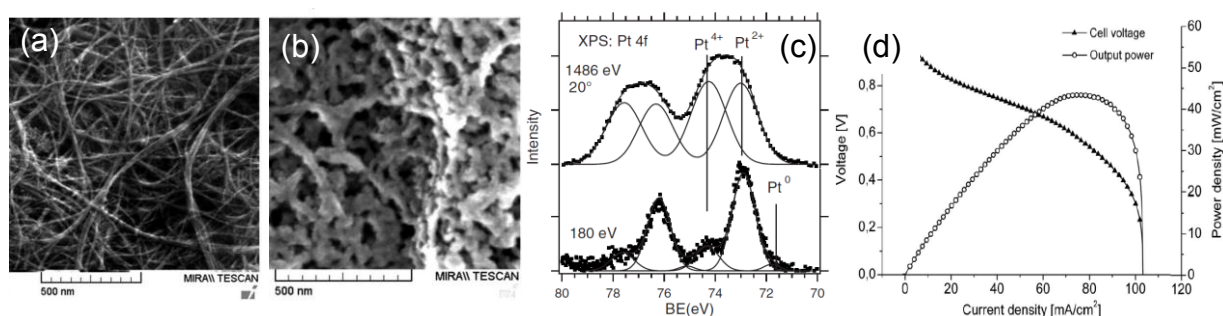
Figure 31: Properties of Pt-ceria catalysts for hydrogen oxidation on the anode of PEMFC. (a) Scanning electron micrograph of double-wall carbon nanotube (DWCNT) catalyst support. Image width 1.5 μm. (b) 30 nm of Pt-ceria catalyst sputter deposited on the DWCNT support. Image width 900 nm. (c) PES of Pt 4f showing the presence of Pt in ionic forms Pt^{2+} and Pt^{4+}. PES with high surface sensitivity (bottom curve) indicates that Pt^{2+} is localized preferentially on the surface of the catalyst. (d) Polarization and power density diagrams of a fuel cell with $Pt-CeO_2$/DWCNT anode demonstrate the high activity of the catalyst. Adapted from Ref. [59], Appendix 11.

Model catalyst studies aiming at understanding the physicochemical properties of ceria based catalysts have been performed by a range of laboratories, mainly on thin oriented films of CeO_2 (111) on single crystal metal substrates. Majority of the work have been performed on CeO_2/Ru(0001) [14], [175]–[177]. Important results have been obtained also on other metal substrates – Pt [178]–[180], Au [41], [181], Cu [45]. The main adjustable parameter in existing model studies on ceria is the degree of ceria reduction and the related concentration of oxygen vacancies in ceria [14]. Low-coordinated sites on the surface of ceria, particularly the monoatomic steps have been considered qualitatively as the nucleation sites of metal clusters [182], [183].

The Surface Physics group has been developing model catalyst system of thin film of CeO_2(111) on Cu(111) [51]. Employing scanning tunneling microscope and evaluating quantitative morphological information on this model catalyst as described in the present Thesis we were able to develop a range of model ceria based catalysts with increasing but controlled complexity (cf. Figure 4) and to use these model catalysts in high-impact model catalytic studies on ceria and Pt-ceria catalysts.

5.1 Inverse model catalysts and proximity effects

Parallel to the traditional configuration of model catalysts when metal clusters are supported on planar oxide surfaces [21]–[25], model catalysts are prepared and investigated in so called "inverse" configuration as oxide clusters supported on planar metal surfaces. Such configuration is readily investigated with microscopic methods [184], and, compared to the traditional configuration, oxide clusters expose many low-coordinated active sites relevant for the comparison with real catalysts ([44], [45], Figure 7). Inverse model catalysts represent systems of ultrathin oxide layers that are strongly influenced by the close proximity of the metal [185] eventually giving rise to oxide phases that are not existing in bulk but may be relevant for heterogeneous catalysis [186].

We have studied inverse model catalyst CeO_2/Cu(111), Refs. [187], [188], Appendices 12, 13. Islands of CeO_2(111) growing on Cu(111) consist of 1 monolayer (1 ML), 2 ML, and ≥2 ML thick areas allowing to compare physicochemical properties of different thicknesses of ultrathin ceria (Figure 32 a). 2 ML and thicker ceria exhibit bulk-like unreconstructed termination in STM (Figure 32 b), Ref. [189]. 1 ML thick ceria, on the other hand, exhibits a 2×2 reconstructed structure (Figure 32 c). Ab-initio calculations reveal that the observed structure is due to an ordered array of oxygen vacancies localized in the interface between Cu and 1 ML ceria (Figure 32 c). Different behavior of the oxygen vacancies in 1 ML thick ceria compared to bulk ceria may give rise to the high catalytic activity of ultrathin cerium oxide islands on Cu(111).
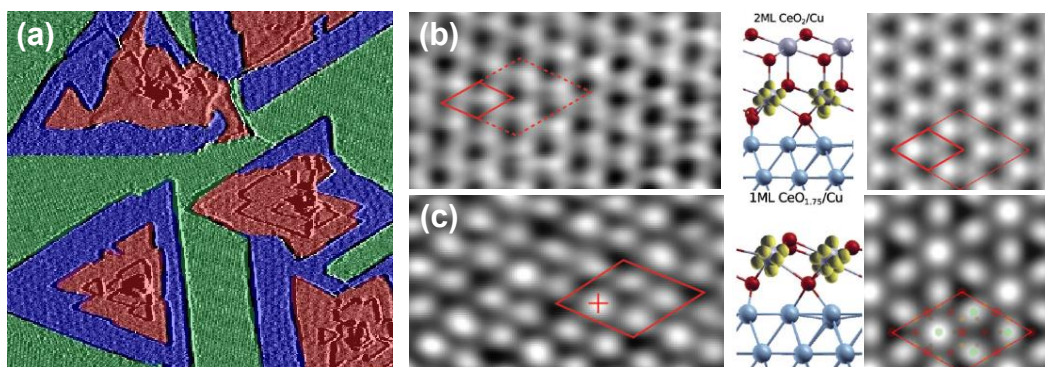
Figure 32: Inverse model catalyst CeO_2/Cu(111). (a) Morphology of 0.5 ML CeO_2(111) on Cu(111). STM, image width 100 nm. Green – oxidized Cu substrate, blue – 1 ML thick ceria, brown – 2 ML or thicker ceria. (b) properties of 2 ML thick ceria. Left – STM view of the unreconstructed CeO_2(111) surface of 2 ML thick ceria, middle – structure of 2 ML ceria from ab-initio calculation, right – ab-initio calculation of STM image of 2 ML thick ceria. The elementary surface unit cell is outlined red. (c) properties of 1 ML thick ceria. Left – STM view of the 2×2 reconstruction of 1 ML thick ceria, middle – structure of 1 ML ceria from ab-initio calculation, right – ab-initio calculation of STM image of 1 ML thick ceria. The unit cell of the 2×2 reconstruction is outlined red. Image width (b, c) 2.5 nm. Adapted from Ref. [187], Appendix 12.

Besides the variations in the behavior of oxygen vacancies caused by charge transfer between ceria and copper in 1 ML thick ceria we observe a contraction of the lattice constant of ultrathin ceria as a function of ceria thickness (Refs. [187], [188], Appendices 12, 13). Ab-initio calculations on thin ceria slabs identify this phenomenon as an intrinsic finite size effect. Supported on Cu(111) the contraction of the lattice constant is alleviated by the charge transfer between the ceria and the substrate as well as by the formation of the oxygen vacancies, however, it still remains a distinct property of the inverse model catalyst CeO_2/Cu(111). Variation of the ceria thickness in the inverse model catalyst CeO_2/Cu(111) causes a strongly inhomogeneous strain distribution in the ceria thin film that can be considered as a generic mechanism of strain buildup in heteroepitaxy of incommensurate thin films ([188], Appendix 13). The presented studies of the inverse model catalyst CeO_2/Cu(111) have become a standard reference for the crystallographic and electronic structure and for the proximity effects on metal-ceria interfaces [190]–[193].
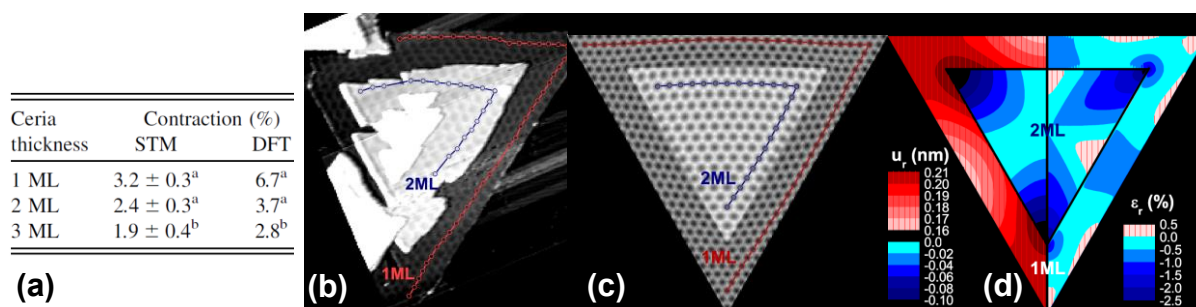
Figure 33: (a) Thickness-dependent lattice constant of ceria films with 1, 2, and 3 nm thickness. STM – from experimental Moiré patterns, DFT – from ab-initio calculations. (b - d) Strain distribution in the inverse model catalyst CeO_2/Cu(111). (b) STM of a Moiré pattern on the CeO_2 island on Cu(111) with indicated 1 ML and 2 ML thickness. Image width 120 nm. (c) Simulation of the Moiré pattern in the CeO_2 island from a finite element calculation. (d) Radial displacement u_r and radial strain ε_r in the CeO_2 island. Adapted from Ref. [188], Appendix 13.

5.2   Step density and oxygen vacancy concentration on model ceria surfaces

Step edges are considered important low-coordinated adsorption positions that may determine the surface chemical reactivity in a decisive way [16], [194], [195]. The importance of the step edges is beginning to be recognized also on oxide substrates [196]–[198] including ceria [189], [199]–[201]. For quantitative investigations of the chemical reactivity of step edges on ceria we have developed experimental procedures allowing to adjust the step density on the CeO_2(111) thin films on Cu(111), Ref. [202], Appendix 14.

For depositing CeO_2 on the copper surface we are using a standard method of depositing Ce metal on the Cu substrate at elevated temperature and in oxygen atmosphere with oxygen pressure 5×10^{-5} Pa [51]. The growth mode of ceria on Cu(111) turns out to be three-dimensional, yielding a discontinuous film with ceria mounds separated by trenches with exposed Cu substrate (Figure 34 a). Since the high chemical reactivity of the ceria-copper interface [45] may strongly influence the results of model catalytic studies, we first modify the procedure to obtain continuous ceria films. This is achieved by imposing a kinetic limitation on the growth of the ceria layer [203], [204] by depositing ceria initially at room temperature (RT) and increasing the temperature of the copper substrate at later stages of ceria deposition [202]. The resulting films are continuous, atomically flat, and mimicking the ideal termination of a CeO_2(111) single crystal (Figure 34 b).

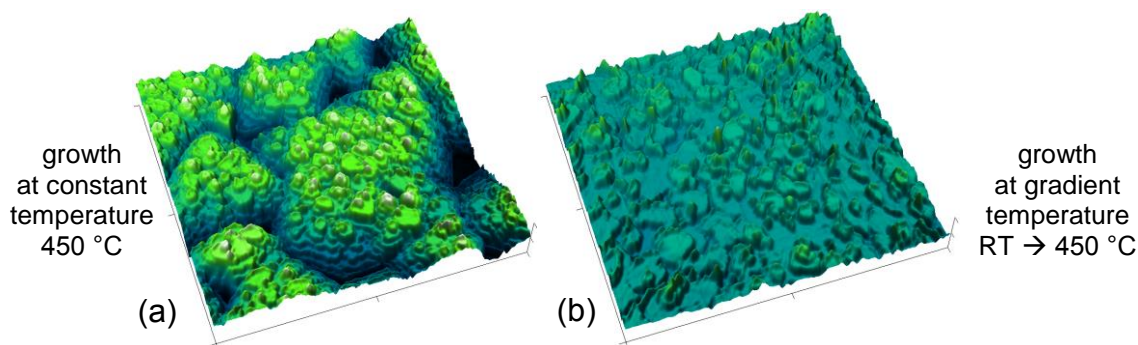**Figure 34:** Morphology of ceria layer on Cu(111). (a) Growth at constant substrate temperature, (b) growth with substrate temperature increasing from room temperature. STM images 240×240 nm^2, adapted from Ref. [202], Appendix 14.

On the flat and continuous CeO$_2$(111) films on Cu(111) we obtain control over the density of monolayer high step edges by adjusting the maximum temperature of the copper substrate during growth. Step densities between approximately 6 and 18%, i.e. changing by a factor of 3 can be achieved (Figure 35). When using these model catalysts for further investigations care must be taken about the maximum temperature in the experiment. When the temperature in the experiment exceeds the growth temperature of the model catalyst, step density of the model catalyst may decrease [202].
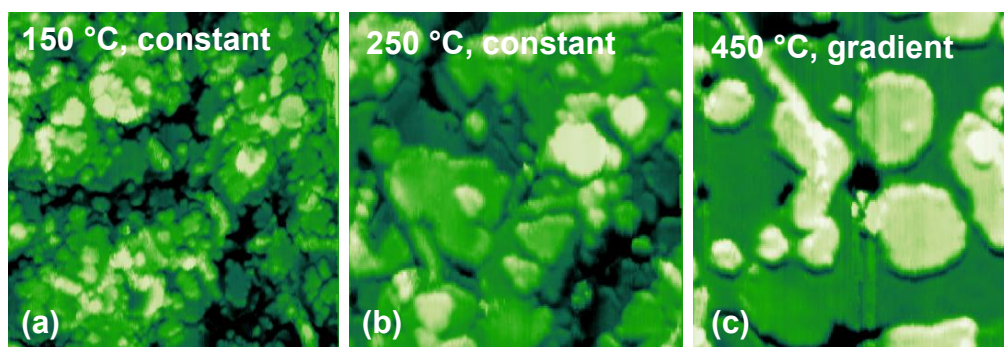
Figure 35: Morphology and step density of ceria layers on Cu(111) prepared at different maximum temperatures (constant or gradient). STM image width 60 nm, adapted from Ref. [202], Appendix 14.

Virtually all practical applications of ceria are based on the ability of ceria to release and store oxygen via creation and annihilation of surface and bulk oxygen vacancies [158], [205]–[208]. Density of oxygen vacancies, and the related degree of reduction of ceria are thus the most important parameters of model and real ceria based catalysts [14], [46], [174], [209]. In model catalysts, ceria reduction has been achieved by a variety of experimental approaches – growth of ceria layers in a reduced pressure of oxygen [175], reduction of ceria by annealing in vacuum [178], by interaction with a reducing atmosphere [210], or by ion erosion [211]. Ceria reduction is standardly determined by XPS [54]. Oxygen vacancies on the ceria surface can be identified by microscopic methods [179]. In some cases microscopy reveals a tendency of the surface oxygen vacancies to organize in regular structures [206], [212].

We have developed an alternative method of preparing reduced thin films of ceria. Instead of removing oxygen from the ceria sample we deposit Ce metal on thin films of CeO$_2$(111) and let the Ce react with the CeO$_2$ thin film ceria in a so called interfacial reaction [213]–[215]. Initially, the method has been used for preparing thin films of Ce$_2$O$_3$ on Cu(111), Figure 36 ([213], Appendix 15).

900 K
CeO₂ layer + Ce metal → Ce₂O₃ layer
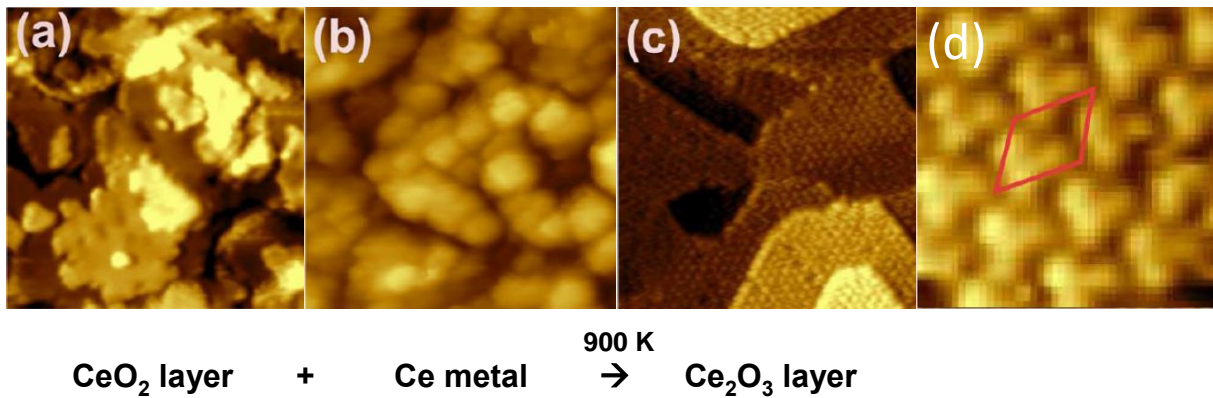
Figure 36: Method for obtaining thin films of reduced ceria via interfacial reaction with metallic Ce. STM morphology of (a) thin film of CeO₂(111)/Cu(111), (b) Ce metal deposited on the CeO₂(111) thin film at room temperature, (c) thin film of Ce₂O₃ upon annealing of Ce/CeO₂(111)/Cu(111) at 900 K In vacuum. (d) A detailed view of the surface morphology of the Ce₂O₃ thin film with outlined unit cell of the 4×4 surface reconstruction [with respect to CeO₂(111)]. Image width (a) – (c) 45 nm, (d) 6 nm. Adapted from Ref. [213], Appendix 15.

Ce₂O₃ represents a limiting case of ceria reduction with 25 % of oxygen atoms removed. Thin films of Ce₂O₃ prepared by the interfacial reaction exhibit a surface superstructure corresponding to a 4×4 surface reconstruction with respect to CeO₂(111) (Figure 36 d). This is a fingerprint of cubic bixbyite structure of the prepared Ce₂O₃ layers [216] and a result of long range ordering of oxygen vacancies in ceria reduced by interfacial reaction with Ce metal.

Degree of reduction and the concentration of oxygen vacancies in ceria layers prepared by the interfacial reaction with Ce can be adjusted by depositing different amounts of Ce metal. This way, layers of CeO$_{2-x}$ in the full range of $0 \leq x \leq 0.5$ can be obtained (Ref. [214], Appendix 16). Besides Ce₂O₃, we observe formation ordered oxygen vacancies also for other stoichiometries of the reduced CeO$_{2-x}$ layers, particularly a 3×3 superstructure for CeO₁.₆₇, and a √7×√7 superstructure for CeO₁.₇₁ or Ce₇O₁₂, Figure 37. The interfacial reaction with Ce, and the identification of reduced ceria phases by electron diffraction represent universal approaches that can be used also on other substrates than Cu(111) as evidenced on the examples of Ru(0001) [215] or Cu(110) [217].
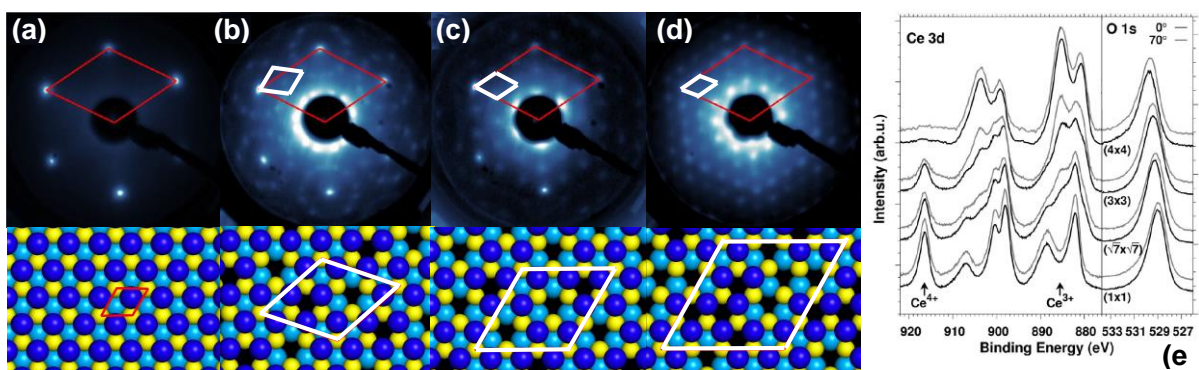
Figure 37: Ordered phases of reduced ceria obtained by the interfacial reaction of Ce with CeO₂(111) thin films. LEED diffraction pattern (E=55 eV) and surface models of (a) CeO₂(111) surface before the reaction, and (b)-(d) superstructures obtained for CeO₁.₇₁ (√7×√7), CeO₁.₆₇ (3×3), and CeO₁.₅ (4×4). Red outline – surface unit cell of CeO₂(111), white outline – surface unit cells of the oxygen vacancy superstructures. Ball models: yellow – Ce, blue – O, black – O vacancy. (e) XPS spectra corresponding to the ordered phases of reduced ceria. Adapted from Ref. [214], Appendix 16.

The experimental bottom-up approaches to nanostructuring thin films of ceria on Cu(111) developed and presented in Refs. [202], [213], [214] (Figures 34-37, Appendices 14-16) allow to prepare ceria based model catalysts with independent atomic-level control of key morphological parameters – the coverage of the ceria layer, the density of steps of the ceria layer, and the density and the space correlations of oxygen vacancies. The unique portfolio of the bottom-up approaches to nanostructuring thin films of ceria has been summarized in a dedicated review (Ref. [218], Appendix 17) as well as in a dedicated book chapter [219]. The studies involved in establishing the bottom-up approaches to nanostructuring thin films of ceria revealed many fundamental physicochemical aspects of ceria reduction and metal-ceria interactions and have been broadly acknowledged by the heterogeneous catalysis community being listed e.g. in many recent reviews of catalysis over ceria and catalysis over reducible oxides in general [14], [191], [220]–[222].

A study of chemical reactivity on the abovementioned model ceria surfaces appeared in Ref. [223], Appendix 18 dealing with the interaction of ceria surfaces with water. We have compared the adsorption and desorption of water on stoichiometric stepped $CeO_2(111)$ surface (Figure 38 a) and on the same surface reduced by ion erosion (Figure 38 b). Morphological information obtained from STM revealed that adsorption and desorption of water induces no morphology changes on both the stoichiometric and the reduced ceria (cf. Figures 38 a, b top and bottom), and, in combination with resonant photoelectron spectroscopy measurement [67] allowed to conclude that after ion erosion, reduction of ceria is due to creation of oxygen vacancies on the terraces of $CeO_2(111)$. We observe stronger formation of OH by dissociation of water on the reduced ceria surfaces (cf. Figures 38 c, d). Our study contributed to shaping the up-to-date view of the interaction of the most important molecule – the water molecule – with the ceria surface [208], [224], [225].
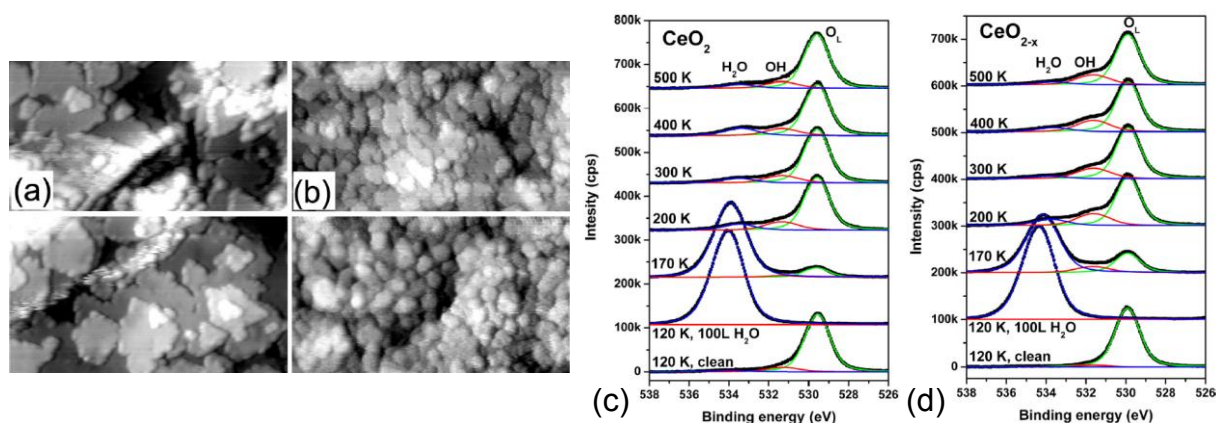
Figure 38: Interaction of stoichiometric and reduced ceria surfaces with water. (a, b) STM morphology of stoichiometric $CeO_2(111)$ (a) and of the same surface reduced by ion erosion (b). Top – morphology before, and bottom – morphology after adsorption and desorption of water. (c, d) XPS spectra of O 1s documenting adsorption and desorption of water on stoichiometric $CeO_2(111)$ (c), and on the surface reduced by ion erosion (d). H_2O – water molecule, OH – dissociated water, O_L – lattice oxygen of ceria. Adapted from Ref. [223], Appendix 18.

5.3   Platinum clusters on model ceria surfaces

Continuous thin films of $CeO_2(111)$ on $Cu(111)$ introduced in Section 5.2 (Figure 35) are serving as well-defined substrates with a controlled amount of surface defect sites in the studies of ceria supported metal catalysts [210], [226]–[229]. We have performed two fundamental studies into the properties of Pt/ceria catalysts [230], [231], Appendices 19, 20. In both studies, STM was employed to obtain quantitative morphological information on the properties of Pt cluster population on the model ceria surface.

In a study of CO interaction with model Pt/ceria catalysts (Ref. [230], Appendix 19) Pt particles were deposited on the $CeO_2(111)$ layer on $Cu(111)$ prepared at 250 °C (Figure 35 b, Figure 39 a). The interaction of CO with this model catalyst were studied by temperature programmed desorption (TPD) and by infrared absorption spectroscopy (IRAS). In TPD, oxidation of CO and production of CO_2 is observed as a result of reverse spillover of lattice oxygen from the ceria support to the Pt particles [232]. IRAS identifies the adsorption positions of CO molecules on the Pt/ceria catalysts. Besides adsorption positions on the low-index surfaces and on defects on Pt and on CeO_2 we identify adsorption positions of CO influenced by the phenomenon of the reverse spillover – both on the reduced sites of CeO_2, and on the oxidized Pt particles.
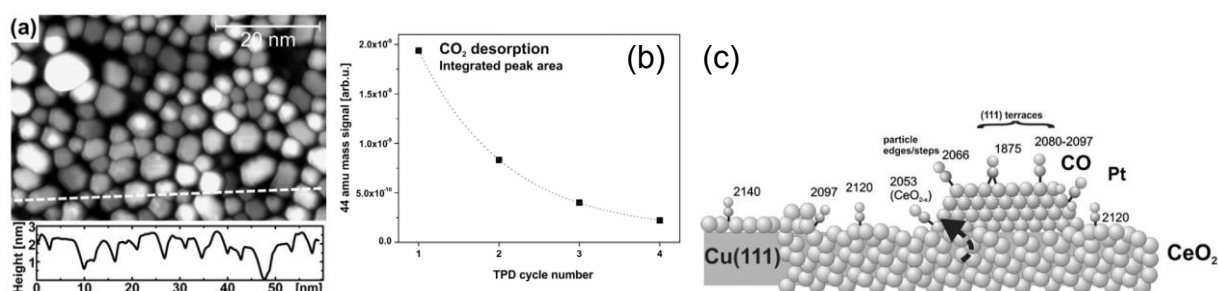
Figure 39: Interaction of CO with model Pt/ceria catalyst. (a) STM of model catalyst – 0.4 nm Pt on a thin film of 5 ML $CeO_2(111)$ on $Cu(111)$. Image width 60 nm. Bottom – height profile of the model catalyst. (b) Production of CO_2 upon repeated TPD of CO on the model catalyst. (c) Adsorption positions of CO on the model Pt/ceria catalyst identified by infrared absorption spectroscopy (IRAS). Adapted from Ref. [230], Appendix 19.

The properties of the Pt/ceria model catalyst system, and the availability of the highly sensitive resonant photoelectron spectroscopy (RPES) for determining the degree of reduction of the ceria supports [67] allowed us, for the first time, to quantify the charge transfer between the metal particles and the oxide support on the example of Pt/ceria system (Ref. [231], Appendix 20). The charge state of the supported metal particles is difficult to detect by the existing experimental methods. When supported on ceria, however, electrons transferred from the Pt particles to the ceria substrate cause reduction of Ce^{4+} ions to Ce^{3+} ions and a clear RPES Ce^{3+} signal [67]. A careful evaluation of the density and the size of the supported Pt particles (Figure 40 a) complemented by the quantification of the charge transfer based on the RPES data allows us to determine the size-dependent charge transfer in the Pt/ceria model catalyst (Figure 40 b). We identify a maximum of the charge transfer between Pt and ceria for Pt particles of 30-70 atoms in size, when approximately 1 electron per 10 Pt atoms is transferred. This information can be used e.g. for increasing the selectivity of heterogeneous catalysts for reactions that are sensitive to the charge of the metal particles in the catalyst.

Figure 40: Quantification of the charge transfer between Pt particles and ceria support. (a) Clean CeO$_2$(111)/Cu(111) surface and Pt deposits of different thickness for quantification of the sizes of Pt particles. (b) Dependence of the Pt particle charge per Pt atom (yellow circles) and per Pt particle (green squares) as a function of Pt particle size. Adapted from Ref. [231], Appendix 20.

5.4 Monodispersed platinum ions on model ceria surfaces
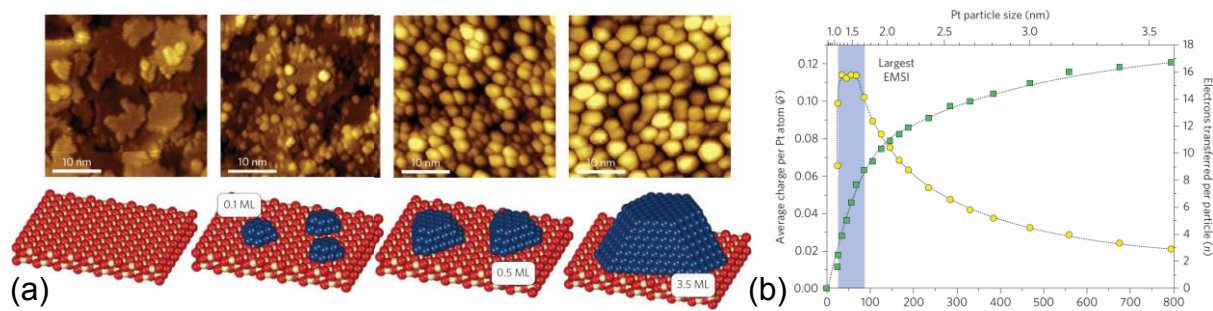
For very small loads of platinum on ceria, the platinum deposit no longer forms metal particles but is becoming predominantly ionic. Catalysts containing platinum ions supported on ceria show an exceptional reactivity in a range of industrially relevant applications including three-way automotive catalysts [233], water-gas shift catalysts [234] or catalysts for hydrogen oxidation reaction on the anode of PEMFC developed in the Surface Physics Group [59], [61], [65]. Platinum ions are stable at reaction conditions of elevated catalyst temperature and reactant pressure and are seemingly responsible for the majority of the turnover in the investigated reactions [233], [234]. Metallic Pt particles, on the other hand, seem not to be catalytically active [233], [234].

The high activity of the ionic Pt allows developing highly active catalysts with very reduced amount of costly Pt. This may represent a practical way for reducing the Pt load in strategic large-scale catalytic applications as, e.g., catalysis for hydrogen economy. Experiments indicate a high dispersion of the Pt deposit [235] qualifying the catalysts with ionic platinum as single-atom catalysts [170]. Single-atom catalysts represent a newly defined and quickly developing branch of research in catalysis dealing with catalysts where the metal load is ultimately dispersed as single metal atoms [236]. Depending on the actual charge, Pt ions seem to be a bulk dopant in ceria (Pt^{4+} ions [59], [169], [237]) or a surface-stabilized species (Pt^{2+} ions [59]).

We have investigated the nature of the Pt^{2+} site on ceria in Refs. [238], [239], Appendices 21, 22. Initially, the geometry of the adsorption site allowing for the stabilization of Pt atom on the ceria surface in the form of Pt^{2+} ion has been predicted theoretically. According to the prediction, Pt^{2+} occupies fourfold oxygen-coordinated sites at the apices of ceria nanoparticles where it strongly binds to four O atoms in a square-planar coordination ([238], Figure 41 a). The energy of the Pt-O bond of Pt^{2+} in square-planar coordination exceeds the Pt-Pt cohesive energy of metallic Pt clusters and ensures the high-temperature stability of the monodispersed Pt^{2+} species. Predicted by the calculation, thermally stable Pt^{2+} species were identified on the Pt-doped CeO$_2$ nanoparticles deposited on the CeO$_2$(111) model catalyst surface ([238], Figure 41 b). Actually, as evidenced by PES measurements, Pt^{2+} species are the only ionic species stable up to the catalyst temperature of 750 K while Pt^{4+} species initially present in the samples together with Pt^{2+} become destabilized ([238], Figure 41 c).
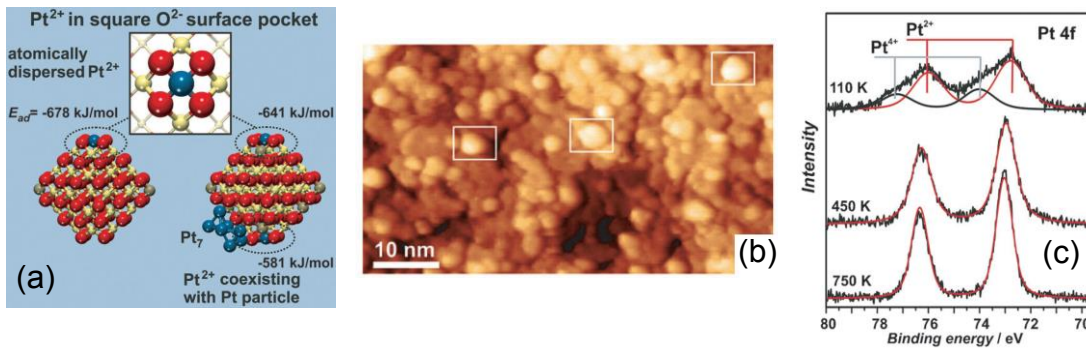
Figure 41: Stability of the ionic Pt^{2+} species supported on the ceria substrate. (a) Geometry of the single-atom adsorption position stabilizing Pt^{2+} ions on the ceria surface as predicted by ab-initio theoretical calculations. (b) STM of Pt-doped CeO$_2$ clusters supported on a model ceria substrate. (c) PES of Pt 4f state indicating the presence of Pt^{2+} and Pt^{4+} species on the as-prepared sample (top). Only Pt^{2+} species remains stable upon annealing of the sample at 450 K (middle) and 750 K (bottom). Adapted from Ref. [238], Appendix 21.

Besides Pt-doped CeO$_2$ nanoclusters we have studied adsorption of small amounts of Pt on highly ordered model ceria surfaces introduced in Section 5.2, Figures 35-37 (Ref. [239], Appendix 22). On reduced model ceria surfaces, Pt always forms metallic Pt clusters ([239], [240], Figure 42 a). On oxidized model ceria surfaces, we observe partial or complete ionization of Pt to Pt^{2+} (Figure 42 b). Preparing oxidized model ceria surfaces with different density of step edges we observe that the amount of Pt adsorbed as Pt^{2+} is proportional to the density of steps on the model ceria surface (Figure 45 c). Based on this observation we can conclude that Pt^{2+} species are stabilized also at step edges of ceria surfaces. The accompanying ab-initio calculations identify the adsorption of Pt^{2+} at different ceria step edges in a square–planar coordination (Figure 45 d, e). This indicates that the ceria surface can effectively bind Pt^{2+} on various types of defects. For stabilization of Pt^{2+} at ceria step edges, binding of excess oxygen from the reaction atmosphere becomes favorable (marked by * in Figures 45 d, e) indicating that the presence of Pt^{2+} in the Pt/ceria catalysts modifies its oxygen storage capacity.
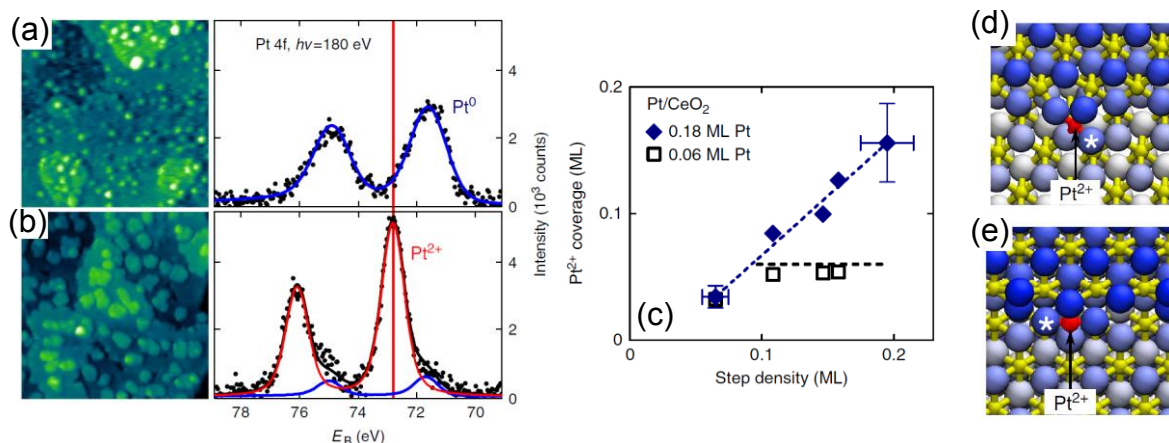
Figure 42: Stabilization of Pt^{2+} on model ceria surfaces. (a) growth of metal Pt clusters on reduced ceria surface. (b) Stabilization of Pt^{2+} on the CeO$_2$(111) surface with a high density of steps. (c) Direct proportionality between the density of steps on the model ceria surface and the amount of Pt^{2+} stabilized on the samples. (d, e) Ab-initio theoretical calculation of the geometry of Pt^{2+} stabilized at ceria step edges. (d) step type I [200], (e) step type II [200]. * denotes excess oxygen from the reaction atmosphere. Adapted from Ref. [239], Appendix 22.

Our model studies of monodispersed platinum ions on model ceria surfaces identify a characteristic square-planar coordination of thermally and chemically stable Pt^{2+} ions on the ceria surface. Pt^{2+} ions can stabilize at different adsorption sites on the ceria surface including monoatomic step edges that represent the most ubiquitous defect on the ceria substrate [196]. We have obtained model catalysts with adjustable concentration of surface stabilized Pt^{2+} ions that will find a broad use in upcoming studies of single-atom catalysis in Pt/ceria systems.

6   Conclusions

The present Thesis illustrates the importance of microscopic characterization, and quantification of morphological parameters in model catalysis. Introduction of the technique of Scanning Tunneling Microscopy in the Surface Physics Group allowed to perform advanced model catalysis studies where the most fundamental question of heterogeneous catalysis – the relationship between the structure and the reactivity of a catalyst – has been effectively addressed. For experimental studies of industrially very important ceria and Pt/ceria based catalyst we have developed a hierarchical system of model catalysts with controlled complexity (Figure 4, Figures 36-42) and used these model catalysts for elucidation a range of physicochemical phenomena underlying the reactivity of ceria and Pt/ceria based catalysts. The relevance of the presented research has been demonstrated by publication in leading specialized [188], [213], [238] as well as interdisciplinary international scientific journals [231], [239]. The presented research has been acknowledged by the international community of researchers in catalysis [14], [208], [221], [222].

Introduction of the technique of Scanning Tunneling Microscopy in the Surface Physics Group enhanced the level of education in the Surface Physics Groups. Working on the topics related to the present Thesis, 1 bachelor, 1 master, and 5 Ph.D. students have finished their Theses gaining invaluable experience with cutting-edge interdisciplinary and international research. The availability of the unique experimental apparatus combining the microscopic and space-averaging surface science techniques (Figure 11) allows the students to obtain hands-on experience with advanced experimental techniques in model catalysis research.
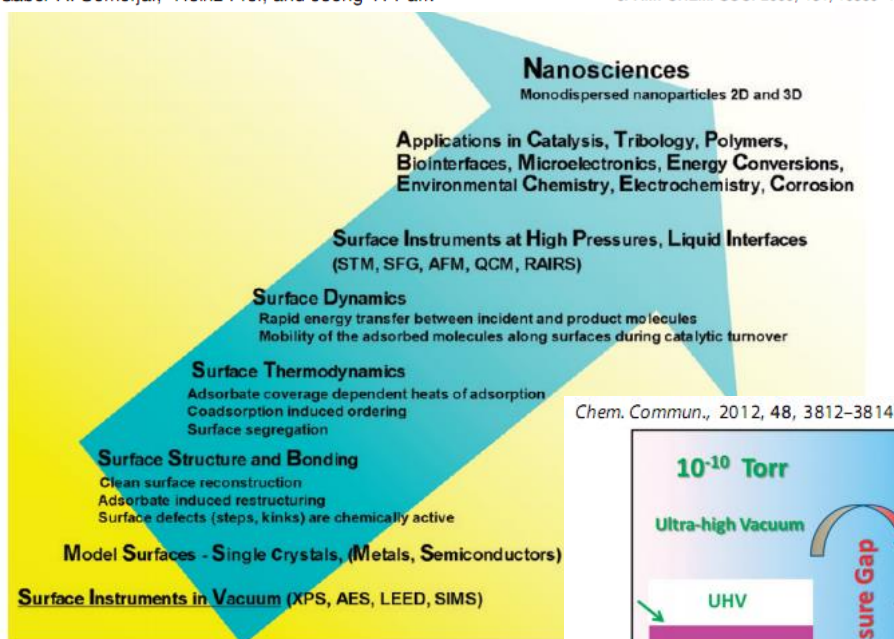
7   Outlook

Quantification of the morphological information in model catalysis and creation and investigation of model catalysts with hierarchically complex morphology as described in the present Thesis represent effective strategies for overcoming the so called materials gap between the real and the model catalysis [10]. The use of classical experimental techniques of surface science that are operated in ultrahigh vacuum imposes another critical difference between the real and the model catalysis – that of the pressure of the reactants above the model catalyst surface. In the conditions of ultrahigh vacuum reactants are exposed on model catalyst surfaces at pressures that are typically 10 orders of magnitude smaller than the atmospheric pressure; this situation is denoted as "pressure gap" [10].

Reactants at realistic pressures may drastically change the morphology of model catalysts [241], [242] huge efforts worldwide are thus directed towards modifying the existing and employing new surface sensitive experimental methods capable of characterizing the model catalysts at realistic pressures ([243], [244], Figure 43). These so called "operando" techniques are currently being adapted for use also in the Surface Physics Laboratory. Ambient pressure photoelectron spectroscopy ([245], Figure 44) allows characterizing the chemical properties of the samples under realistic pressures of the reactants. In combination with high-pressure Scanning Tunneling Microscope ([246], [247]) a powerful experimental apparatus for studies of relationships between structure and reactivity in model catalysts at realistic reaction conditions will become available.

Advancing the Frontiers in Nanocatalysis, Biointerfaces, and Renewable Energy Conversion by Innovations of Surface Techniques

Gabor A. Somorjai,* Heinz Frei, and Jeong Y. Park†

Nanosciences
Monodispersed nanoparticles 2D and 3D

Applications in Catalysis, Tribology, Polymers, Biointerfaces, Microelectronics, Energy Conversions, Environmental Chemistry, Electrochemistry, Corrosion

Surface Instruments at High Pressures, Liquid Interfaces
(STM, SFG, AFM, QCM, RAIRS)

Surface Dynamics
Rapid energy transfer between incident and product molecules
Mobility of the adsorbed molecules along surfaces during catalytic turnover

Surface Thermodynamics
Adsorbate coverage dependent heats of adsorption
Coadsorption induced ordering
Surface segregation

Surface Structure and Bonding
Clean surface reconstruction
Adsorbate induced restructuring
Surface defects (steps, kinks) are chemically active

Model Surfaces - Single Crystals, (Metals, Semiconductors)

Surface Instruments in Vacuum (XPS, AES, LEED, SIMS)

Figure 1. Evolution of surface science.

Chem. Commun., 2012, 48, 3812–3814

10⁻¹⁰ Torr — Ultra-high Vacuum — UHV — UHV/Solid interface
Pressure Gap
Torrs or higher — Atmosphere or higher pressure — Gaseous Reactant (ambient pressure) — Gas/Solid interface
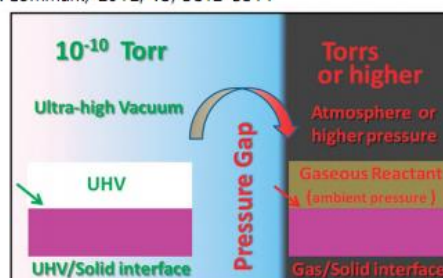
Fig. 1 Schematic of the pressure gap in the study of heterogeneous catalysis.

Figure 43: Extending the scope of topics that can be addressed by the methods of surface science when "operando" methods of surface characterization at realistic pressures and in liquids become available. Adapted from Refs. [243], [244]. Illustration from the graduate course NEVF515 – Methods of Surface and Thin Film Physics I. Josef Mysliveček, MFF UK Praha.

(a)

(b)

SPECS™
PHOIBOS 150 NAP
Near Ambient Pressure Hemispherical Energy Analyzer
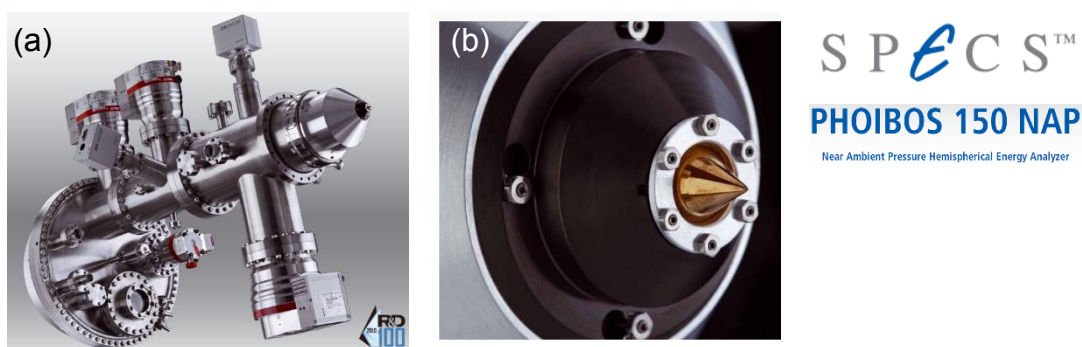
Exchangeable conic aperture separating the high pressure chamber from the first pumping stage. The diameter is 1 mm or less.

Figure 44: Near ambient pressure electron energy analyzer Specs Phoibos 150 NAP [248], [249] installed in the Surface Physics Group as a part of a complex experimental apparatus allowing operando characterization of real and model catalysts. Adapted from the Internet presentation of the manufacturer SPECS Surface Nano Analysis GmbH, Berlin, Germany [249].

Many of the up-to-date catalytic applications including Polymer Electrolyte Membrane Fuel Cells (PEMFCs, [250]) or Electrolyzers (PEMECs, [251]) are, essentially, electrochemical in their nature. For effective development of the corresponding model catalysis experiments implementation of the electrochemical analytic methods on the model catalysts becomes inevitable. In the Surface Physics Laboratory we are implementing the method of transferring highly defined model catalysts prepared and characterized by surface science methods in vacuum into electrolyte for the subsequent electrochemical characterization ([252], [253], Figure 44). This will allow us to enter the prospective field of model electrocatalysis [254], [255] and develop model electrocatalysis of oxide/metal systems relevant to hydrogen economy.
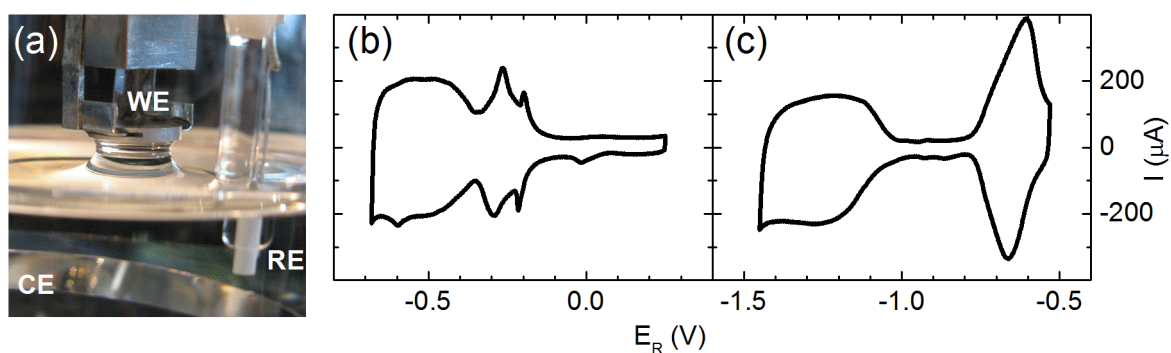
Figure 45: Electrochemical characterization of model catalysts transferred from vacuum to electrolyte. (a) Model catalyst as a working electrode (WE) in contact with liquid electrolyte. Reference electrode (RE) and counter electrode (CE) complement the setup for characterization by cyclic voltammetry. (b, c) Cyclic voltammograms of clean Pt(111) surface in 0.1 M H$_2$SO$_4$ (b) and 0.1 M KOH solutions (c) – proof-of-principle measurements confirming the correct adaptation of the method. Unpublished results, Jiří Keresteš, Charles University in Prague, 2016.

8 References

[1]   G. Ertl, H. Knözinger, F. Schüth, and J. Weitkamp, Eds., *Handbook of Heterogeneous Catalysis*. Weinheim, Germany: Wiley-VCH Verlag GmbH & Co. KGaA, 2008.

[2]   F. Dvořák, "Interaction of simple molecules with reducible oxides: model studies of H2O/CeOx and CO/CuOx," Charles University in Prague, 2014.

[3]   G. Prieto and F. Schüth, "Bridging the gap between insightful simplicity and successful complexity: From fundamental studies on model systems to technical catalysts," *J. Catal.*, vol. 328, pp. 59–71, 2015, doi:10.1016/j.jcat.2014.12.009.

[4]   H. P. Bonzel, "The role of surface science experiments in understanding heterogeneous catalysis," *Surf. Sci.*, vol. 68, pp. 236–258, Nov. 1977, doi:10.1016/0039-6028(77)90209-6.

[5]   D. W. Goodman, "Model catalytic studies over metal single crystals," *Acc. Chem. Res.*, vol. 17, no. 5, pp. 194–200, May 1984, doi:10.1021/ar00101a007.

[6]   D. W. Goodman, "Model Studies in Catalysis Using Surface Science Probes," *Chem. Rev.*, vol. 95, no. 3, pp. 523–536, May 1995, doi:10.1021/cr00035a004.

[7]   *Press release: The 2007 Nobel Prize in Chemistry*. The Royal Swedish Academy of Sciences, 2007.

[8]   G. Ertl, "Reactions at surfaces: From atoms to complexity (Nobel lecture)," *Angew. Chemie - Int. Ed.*, vol. 47, pp. 3524–3535, 2008, doi:10.1002/anie.200800480.

[9]   J. M. Thomas, "Heterogeneous catalysis: Enigmas, illusions, challenges, realities, and emergent strategies of design," *J. Chem. Phys.*, vol. 128, no. 18, p. 182502, 2008, doi:10.1063/1.2832309.

[10]   D. W. Goodman, "Correlations between Surface Science Models and 'Real-World' Catalysts," *J. Phys. Chem.*, vol. 100, no. 100, pp. 13090–13102, 1996, doi:10.1021/jp953755e.

[11]   U. Diebold, S.-C. Li, and M. Schmid, "Oxide surface science," *Annu. Rev. Phys. Chem.*, vol. 61, pp. 129–48, Jan. 2010, doi:10.1146/annurev.physchem.012809.103254.

[12]   C. T. Campbell and J. Sauer, "Introduction: Surface chemistry of oxides," *Chem. Rev.*, vol. 113, no. 6, pp. 3859–3862, 2013, doi:10.1021/cr4002337.

[13]   U. Diebold, "The surface science of titanium dioxide," *Surf. Sci. Rep.*, vol. 48, no. 5–8, pp. 53–229, Jan. 2003, doi:10.1016/S0167-5729(02)00100-0.

[14]   D. R. Mullins, "The surface chemistry of cerium oxide," *Surf. Sci. Rep.*, vol. 70, no. 1, pp. 42–85, 2015, doi:10.1016/j.surfrep.2014.12.001.

[15]   H. Kuhlenbeck, S. Shaikhutdinov, and H. Freund, "Well-ordered transition metal oxide layers in model catalysis - a series of case studies," *Chem. Rev.*, vol. 113, no. 6, pp. 3986–4034, Jun. 2013, doi:10.1021/cr300312n.

[16]   T. Zambelli, J. Wintterlin, J. Trost, and G. Ertl, "Identification of the 'Active Sites' of a Surface-Catalyzed Reaction," *Science*, vol. 273, no. 5282, pp. 1688–1690, Sep. 1996, doi:10.1126/science.273.5282.1688.

[17]   J. T. Yates, "Surface chemistry at metallic step defect sites," *J. Vac. Sci. Technol. A Vacuum, Surfaces, Film.*, vol. 13, no. 3, p. 1359, May 1995, doi:10.1116/1.579564.

[18]   J. K. Nørskov, T. Bligaard, B. Hvolbaek, F. Abild-Pedersen, I. Chorkendorff, and C. H. Christensen, "The nature of the active site in heterogeneous metal catalysis," *Chem. Soc. Rev.*, vol. 37, no. 10, pp. 2163–71, 2008, doi:10.1039/b800260f.

[19]   B. Hammer, "Special sites at noble and late transition metal catalysts," *Top. Catal.*, vol. 37, no. 1, pp. 3–16, 2006, doi:10.1007/s11244-006-0004-y.

[20]   R. A. Van Santen, "Complementary structure sensitive and insensitive catalytic relationships.," *Acc. Chem. Res.*, vol. 42, no. 1, pp. 57–66, Jan. 2009, doi:10.1021/ar800022m.

[21]   C. R. Henry, "Surface studies of supported model catalysts," *Surf. Sci. Rep.*, vol. 31, no. 7–8, pp. 231–325, 1998, doi:10.1016/S0167-5729(98)00002-8.

[22]   U. Heiz and W.-D. Schneider, "Nanoassembled model catalysts," *J. Phys. D. Appl. Phys.*, vol. 33, no. 11, pp. R85–R102, 2000, doi:10.1088/0022-3727/33/11/201.

[23]   H.-J. Freund, "Clusters and islands on oxides: from catalysis via electronics and magnetism to optics," *Surf. Sci.*, vol. 500, no. 1–3, pp. 271–299, Mar. 2002, doi:10.1016/S0039-6028(01)01543-6.

[24]   E. C. Tyo and S. Vajda, "Catalysis by clusters with precise numbers of atoms," *Nat. Nanotechnol.*, vol. 10, no. 7, pp. 577–588, 2015, doi:10.1038/nnano.2015.140.

[25]   C. R. Henry, "2D-Arrays of Nanoparticles as Model Catalysts," *Catal. Letters*, vol. 145, no. 3, pp. 731–749, Mar. 2015, doi:10.1007/s10562-014-1402-6.

[26]   J. Libuda, S. Schauermann, M. Laurin, T. Schalow, and H. J. Freund, "Model studies in heterogeneous catalysis. From structure to kinetics," *Monatshefte fur Chemie*, vol. 136, no. 1, pp. 59–75, 2005, doi:10.1007/s00706-004-0249-8.

[27]   C. J. Davisson, "The Discovery of Electron Waves (Nobel lecture)," *Bell Syst. Tech. J.*, vol. 17, no. 3, pp. 475–482, 1938, doi:10.1002/j.1538-7305.1938.tb00792.x.

[28]   M. Henzler, "LEED studies of surface imperfections," *Appl. Surf. Sci.*, vol. 11–12, no. C, pp. 450–469, 1982, doi:10.1016/0378-5963(82)90092-7.

[29]   K. Heinz, "Structural analysis of surfaces by LEED," *Prog. Surf. Sci.*, vol. 27, no. 4, pp. 239–326, Jan. 1988, doi:10.1016/0079-6816(88)90008-1.

[30]   K. Siegbahn, "Electron spectroscopy for atoms, molecules, and condensed matter (Nobel Lecture)," *Rev. Mod. Phys.*, vol. 54, no. 3, pp. 709–728, 1982, doi:10.1103/RevModPhys.54.709.

[31]   C. S. Fadley, "X-ray photoelectron spectroscopy: Progress and perspectives," *J. Electron Spectros. Relat. Phenomena*, vol. 178–179, no. C, pp. 2–32, May 2010, doi:10.1016/j.elspec.2010.01.006.

[32]   J. L. Falconer and J. A. Schwarz, "Temperature-Programmed Desorption and Reaction: Applications to Supported Catalysts," *Catal. Rev.*, vol. 25, no. 2, pp. 141–227, Jun. 1983, doi:10.1080/01614948308079666.

[33]   A. M. de Jong and J. W. Niemantsverdriet, "Thermal desorption analysis: Comparative test of ten commonly applied procedures," *Surf. Sci.*, vol. 233, no. 3, pp. 355–365, 1990, doi:10.1016/0039-6028(90)90649-S.

[34]   Y. T. Lee, "Molecular Beam Studies of Elementary Chemical Processes (Nobel Lecture)," *Angew. Chemie Int. Ed. English*, vol. 26, no. 10, pp. 939–951, Oct. 1987, doi:10.1002/anie.198709393.

[35]   J. Libuda and H.-J. Freund, "Molecular beam experiments on model catalysts," *Surf. Sci. Rep.*, vol. 57, no. 7–8, pp. 157–298, 2005, doi:10.1016/j.surfrep.2005.03.002.

[36] E. Ruska, "The Development of the Electron Microscope and of Electron Microscopy (Nobel Lecture)," *Angew. Chemie Int. Ed. English*, vol. 26, no. 7, pp. 595–605, 1987, doi:10.1002/anie.198705953.

[37] G. Binnig and H. Rohrer, "Scanning tunneling microscopy—from birth to adolescence (Nobel Lecture)," *Rev. Mod. Phys.*, vol. 59, no. 3, pp. 615–625, 1987, doi:10.1103/RevModPhys.59.615.

[38] G. Binnig, H. Rohrer, C. Gerber, and E. Weibel, "Surface Studies by Scanning Tunneling Microscopy," *Phys. Rev. Lett.*, vol. 49, no. 1, pp. 57–61, 1982, doi:10.1103/PhysRevLett.49.57.

[39] G. Binnig, F. Quate, and C. Gerber, "Atomic Force Microscope," *Phys. Rev. Lett.*, vol. 56, no. 9, pp. 930–933, 1986, doi:10.1103/PhysRevLett.56.930.

[40] A. Picolin, C. Busse, A. Redinger, M. Morgenstern, and T. Michely, "Desorption of H2O from Flat and Stepped Pt(111)," *J. Phys. Chem. C*, vol. 113, no. 2, pp. 691–697, Jan. 2009, doi:10.1021/jp808170f.

[41] J. A. Rodriguez, S. Ma, P. Liu, J. Hrbek, J. Evans, and M. Perez, "Activity of CeOx and TiOx Nanoparticles Grown on Au(111) in the Water-Gas Shift Reaction," *Science (80-.).*, vol. 318, no. 5857, pp. 1757–1760, Dec. 2007, doi:10.1126/science.1150038.

[42] M. Valden, X. Lai, and D. W. Goodman, "Onset of Catalytic Activity of Gold Clusters on Titania with the Appearance of Nonmetallic Properties," *Science*, vol. 281, no. 5383, pp. 1647–1650, Sep. 1998, doi:10.1126/science.281.5383.1647.

[43] A. Hodgson and S. Haq, "Water adsorption and the wetting of metal surfaces," *Surf. Sci. Rep.*, vol. 64, no. 9, pp. 381–451, 2009, doi:10.1016/j.surfrep.2009.07.001.

[44] J. A. Rodríguez and J. Hrbek, "Inverse oxide/metal catalysts: A versatile approach for activity tests and mechanistic studies," *Surf. Sci.*, vol. 604, no. 3–4, pp. 241–244, Feb. 2010, doi:10.1016/j.susc.2009.11.038.

[45] J. A. Rodriguez, J. Graciani, J. Evans, J. B. Park, F. Yang, D. Stacchiola, S. D. Senanayake, S. Ma, M. Pérez, P. Liu, J. F. Sanz, and J. Hrbek, "Water-Gas Shift Reaction on a Highly Active Inverse CeOx/Cu(111) Catalyst: Unique Role of Ceria Nanoparticles," *Angew. Chemie Int. Ed.*, vol. 48, no. 43, pp. 8047–8050, Oct. 2009, doi:10.1002/anie.200903918.

[46] A. Hornés, A. B. Hungría, P. Bera, A. L. Cámara, M. Fernández-García, A. Martínez-Arias, L. Barrio, M. Estrella, G. Zhou, J. J. Fonseca, J. C. Hanson, and J. a Rodriguez, "Inverse CeO2/CuO Catalyst As an Alternative to Classical Direct Configurations for Preferential Oxidation of CO in Hydrogen-Rich Stream," *J. Am. Chem. Soc.*, vol. 132, no. 1, pp. 34–35, Jan. 2010, doi:10.1021/ja9089846.

[47] A. S. K. Hashmi and G. J. Hutchings, "Gold Catalysis," *Angew. Chemie - Int. Ed.*, vol. 45, no. 47, pp. 7896–7936, 2006, doi:10.1002/anie.200602454.

[48] I. Stará, V. Nehasil, and V. Matolín, "The influence of particle size on CO oxidation on model catalyst," *Surf. Sci.*, vol. 331–333, pp. 173–177, 1995, doi:10.1016/0039-6028(95)00183-2.

[49] V. Matolín, I. Stará, N. Tsud, and V. Johánek, "XPS and TPD study of CO interaction with Pd – AlOx Systems," *Prog. Surf. Sci.*, vol. 67, pp. 167–181, 2001.

[50] V. Matolín and I. Stará, "CO diffusion over the alumina support of Pd particle model catalysts," *Surf. Sci.*, vol. 398, pp. 117–124, 1998.

[51] F. Šutara, M. Cabala, L. Sedláček, T. Skála, M. Škoda, V. Matolín, K. C. Prince, and V. Cháb, "Epitaxial growth of continuous CeO2(111) ultra-thin films on Cu(111)," *Thin Solid Films*, vol. 516, no. 18, pp. 6120–6124, 2008, doi:10.1016/j.tsf.2007.11.013.

[52] M. Škoda, M. Cabala, I. Matolínová, K. C. Prince, T. Skála, F. Šutara, K. Veltruská, and V. Matolín, "Interaction of Au with CeO2(111): A photoemission study," *J. Chem. Phys.*, vol. 130, no. 3, p. 034703, Jan. 2009, doi:10.1063/1.3046684.

[53] M. Škoda, M. Cabala, I. Matolínová, T. Skála, K. Veltruská, and V. Matolín, "A photoemission study of the ceria and Au-doped ceria/Cu(111) interfaces," *Vacuum*, vol. 84, no. 1, pp. 8–12, Aug. 2009, doi:10.1016/j.vacuum.2009.04.058.

[54] T. Skála, F. Šutara, K. C. Prince, and V. Matolín, "Cerium oxide stoichiometry alteration via Sn deposition: Influence of temperature," *J. Electron Spectros. Relat. Phenomena*, vol. 169, no. 1, pp. 20–25, Jan. 2009, doi:10.1016/j.elspec.2008.10.003.

[55] T. Skála, N. Tsud, K. C. Prince, and V. Matolín, "Interaction of tungsten with CeO2(111) layers as a function of temperature: a photoelectron spectroscopy study," *J. Phys. Condens. Matter*, vol. 23, no. 21, p. 215001, Jun. 2011, doi:10.1088/0953-8984/23/21/215001.

[56] V. Matolín, M. Cabala, I. Matolínová, M. Škoda, J. Libra, M. Václavů, K. C. Prince, T. Skála, H. Yoshikawa, Y. Yamashita, S. Ueda, and K. Kobayashi, "Au+ and Au3+ ions in CeO2 rf-sputtered thin films," *J. Phys. D. Appl. Phys.*, vol. 42, no. 11, p. 115301, Jun. 2009, doi:10.1088/0022-3727/42/11/115301.

[57] V. Matolín, M. Cabala, I. Matolínová, M. Škoda, M. Václavu, K. C. Prince, T. Skála, T. Mori, H. Yoshikawa, Y. Yamashita, S. Ueda, and K. Kobayashi, "Pt and Sn doped sputtered CeO2 electrodes for fuel cell applications," *Fuel Cells*, vol. 10, no. 1, pp. 139–144, 2010, doi:10.1002/fuce.200900036.

[58] V. Matolín, "Method for preparing oxidation catalyst and catalyst prepared by the oxidation," US patent, No. US 8435921 B2, 2013; Japanese patent, No. 5214032, 2013; Korean patent, No 10-1331108, 2013; Chinese patent, No. CN 102186588, 2013, Euro-Asian patent, No. 019445 B1, 2014; Indian patent, No. 266215, 2015.

[59] M. Václavů, I. Matolínová, J. Mysliveček, R. Fiala, and V. Matolín, "Anode Material for Hydrogen Polymer Membrane Fuel Cell: Pt–CeO2 RF-Sputtered Thin Films," *J. Electrochem. Soc.*, vol. 156, no. 8, p. B938, 2009, doi:10.1149/1.3147255.

[60] V. Matolín, I. Matolínová, M. Václavů, I. Khalakhan, M. Vorokhta, R. Fiala, I. Piš, Z. Sofer, J. Poltierová-Vejpravová, T. Mori, V. Potin, H. Yoshikawa, S. Ueda, and K. Kobayashi, "Platinum-Doped CeO2 Thin Film Catalysts Prepared by Magnetron Sputtering," *Langmuir*, vol. 26, no. 15, pp. 12824–12831, Aug. 2010, doi:10.1021/la100399t.

[61] R. Fiala, M. Vaclavu, A. Rednyk, I. Khalakhan, M. Vorokhta, J. Lavkova, V. Potin, I. Matolinova, and V. Matolin, "Pt–CeOx thin film catalysts for PEMFC," *Catal. Today*, vol. 240, pp. 236–241, Feb. 2015, doi:10.1016/j.cattod.2014.03.069.

[62] M. Vorokhta, I. Khalakhan, I. Matolínová, M. Kobata, H. Yoshikawa, K. Kobayashi, and V. Matolín, "Nanostructured Pt–CeO2 thin film catalyst grown on graphite foil by magnetron sputtering," *Appl. Surf. Sci.*, vol. 267, pp. 119–123, Feb. 2013, doi:10.1016/j.apsusc.2012.08.036.

[63] M. Dubau, J. Lavková, I. Khalakhan, S. Haviar, V. Potin, V. Matolín, and I. Matolínová, "Preparation of Magnetron Sputtered Thin Cerium Oxide Films with a Large Surface on Silicon Substrates Using Carbonaceous Interlayers," *ACS Appl. Mater. Interfaces*, vol. 6, no. 2, pp. 1213–1218, Jan. 2014, doi:10.1021/am4049546.

[64] J. Lavkova, I. Khalakhan, M. Chundak, M. Vorokhta, V. Potin, V. Matolin, and I. Matolinova, "Growth and composition of nanostructured and nanoporous cerium oxide thin films on a graphite foil," *Nanoscale*, vol. 7, no. 9, pp. 4038–4047, 2015, doi:10.1039/C4NR06550F.

[65] R. Fiala, M. Vaclavu, M. Vorokhta, I. Khalakhan, J. Lavkova, V. Potin, I. Matolinova, and V. Matolin, "Proton exchange membrane fuel cell made of magnetron sputtered Pt–CeOx and Pt–Co thin film catalysts," *J. Power Sources*, vol. 273, pp. 105–109, 2015, doi:10.1016/j.jpowsour.2014.08.093.

[66] K. Mašek, J. Beran, and V. Matolín, "RHEED study of the growth of cerium oxide on Cu(111)," *Appl. Surf. Sci.*, vol. 259, pp. 34–38, Oct. 2012, doi:10.1016/j.apsusc.2012.06.014.

[67] V. Matolín, M. Cabala, V. Cháb, I. Matolínová, K. C. Prince, M. Škoda, F. Šutara, T. Skála, and K. Veltruská, "A resonant photoelectron spectroscopy study of Sn(Ox) doped CeO2 catalysts," *Surf. Interface Anal.*, vol. 40, no. 3–4, pp. 225–230, Mar. 2008, doi:10.1002/sia.2625.

[68] H. Yoshikawa, I. Matolínová, and V. Matolín, "Practical chemical analysis of Pt and Pd based heterogeneous catalysts with hard X-ray photoelectron spectroscopy," *J. Electron Spectros. Relat. Phenomena*, vol. 190, pp. 268–277, Oct. 2013, doi:10.1016/j.elspec.2013.08.012.

[69] J. Libra and V. Matolín, "Angle resolved photoemission study of the Ce/Pd(111) interface," *Surf. Sci.*, vol. 600, no. 11, pp. 2317–2322, Jun. 2006, doi:10.1016/j.susc.2006.03.025.

[70] J. Tersoff and D. R. Hamann, "Theory of the scanning tunneling microscope," *Phys. Rev. B*, vol. 31, no. 2, pp. 805–813, Jan. 1985, doi:10.1103/PhysRevB.31.805.

[71] R. M. Feenstra, "Scanning tunneling spectroscopy," *Surf. Sci.*, vol. 299–300, pp. 965–979, Jan. 1994, doi:10.1016/0039-6028(94)90710-2.

[72] H. J. W. Zandvliet and A. van Houselt, "Scanning Tunneling Spectroscopy," *Annu. Rev. Anal. Chem.*, vol. 2, pp. 37–55, 2009, doi:10.1146/annurev-anchem-060908-155213.

[73] J. A. Stroscio and D. M. Eigler, "Atomic and Molecular Manipulation with the Scanning Tunneling Microscope," *Science*, vol. 254, no. 5036, pp. 1319–1326, Nov. 1991, doi:10.1126/science.254.5036.1319.

[74] B. C. Stipe, M. A. Rezaei, and W. Ho, "Single-Molecule Vibrational Spectroscopy and Microscopy," *Science*, vol. 280, no. 5370, pp. 1732–1735, Jun. 1998, doi:10.1126/science.280.5370.1732.

[75] "CreaTec Fischer & Co. GmbH." [Online]. Available: www.createc.de.

[76] R. R. Schulz and C. Rossel, "Beetle-like scanning tunneling microscope for ultrahigh vacuum and low-temperature applications," *Rev. Sci. Instrum.*, vol. 65, no. 6, p. 1918, 1994, doi:10.1063/1.1144843.

[77] G. Meyer, "A simple low-temperature ultrahigh-vacuum scanning tunneling microscope capable of atomic manipulation," *Rev. Sci. Instrum.*, vol. 67, no. 8, p. 2960, 1996, doi:10.1063/1.1147080.

[78] I. Ošťádal, P. Kocán, P. Sobotík, and J. Pudl, "Direct Observation of Long-Range Assisted Formation of Ag Clusters on Si(111)7×7," *Phys. Rev. Lett.*, vol. 95, no. 14, p. 146101, Sep. 2005, doi:10.1103/PhysRevLett.95.146101.

[79] P. Kocán, L. Jurczyszyn, P. Sobotík, and I. Ošťádal, "Defects on the Si(100)–(2×1) surface: Anchoring sites of the surface polymerization reaction of In atoms," *Phys. Rev. B*, vol. 77, no. 11, p. 113301, Mar. 2008, doi:10.1103/PhysRevB.77.113301.

[80]   P. Sobotík, M. Setvín, P. Zimmermann, P. Kocán, I. Ošťádal, P. Mutombo, M. Ondráček, and P. Jelínek, "Emergence of state at Fermi level due to the formation of In-Sn heterodimers on Si(100)-2×1," *Phys. Rev. B*, vol. 88, no. 20, p. 205406, Nov. 2013, doi:10.1103/PhysRevB.88.205406.

[81]   D. Nečas and P. Klapetek, "Gwyddion: an open-source software for SPM data analysis," *Open Phys.*, vol. 10, no. 1, pp. 181–188, Jan. 2012, doi:10.2478/s11534-011-0096-2.

[82]   G. Sauerbrey, "Verwendung von Schwingquarzen zur Wägung dünner Schichten und zur Mikrowägung," *Zeitschrift für Phys.*, vol. 155, no. 2, pp. 206–222, Apr. 1959, doi:10.1007/BF01337937.

[83]   J. Mysliveček, A. Stróżecka, J. Steffl, P. Sobotík, I. Ošťádal, and B. Voigtländer, "Structure of the adatom electron band of the Si(111)–7×7 surface," *Phys. Rev. B*, vol. 73, no. 16, p. 161302, Apr. 2006, doi:10.1103/PhysRevB.73.161302.

[84]   G. Binnig, H. Rohrer, C. Gerber, and E. Weibel, "7 × 7 Reconstruction on Si(111) Resolved in Real Space," *Phys. Rev. Lett.*, vol. 50, no. 2, pp. 120–123, Jan. 1983, doi:10.1103/PhysRevLett.50.120.

[85]   R. J. Hamers, R. M. Tromp, and J. E. Demuth, "Surface Electronic Structure of Si (111)-(7×7) Resolved in Real Space," *Phys. Rev. Lett.*, vol. 56, no. 18, pp. 1972–1975, May 1986, doi:10.1103/PhysRevLett.56.1972.

[86]   D. Sawada, Y. Sugimoto, K. Morita, M. Abe, and S. Morita, "Simultaneous measurement of force and tunneling current at room temperature," *Appl. Phys. Lett.*, vol. 94, no. 17, p. 173117, 2009, doi:10.1063/1.3127503.

[87]   M. Passoni, F. Donati, A. Li Bassi, C. S. Casari, and C. E. Bottani, "Recovery of local density of states using scanning tunneling spectroscopy," *Phys. Rev. B*, vol. 79, no. 4, p. 045404, Jan. 2009, doi:10.1103/PhysRevB.79.045404.

[88]   C. J. Chen, *Introduction to Scanning Tunneling Microscopy*, 2nd ed. Oxford University Press, 2007.

[89]   X. Shao, J.-F. Jerratsch, N. Nilius, and H.-J. Freund, "Probing the 4f states of ceria by tunneling spectroscopy," *Phys. Chem. Chem. Phys.*, vol. 13, no. 27, p. 12646, 2011, doi:10.1039/c1cp21113g.

[90]   M. Sterrer, M. Heyde, M. Novicki, N. Nilius, T. Risse, H.-P. Rust, G. Pacchioni, and H.-J. Freund, "Identification of Color Centers on MgO(001) Thin Films with Scanning Tunneling Microscopy," *J. Phys. Chem. B*, vol. 110, no. 1, pp. 46–49, Jan. 2006, doi:10.1021/jp056306f.

[91]   J. Mysliveček, F. Dvořák, A. Stróżecka, and B. Voigtländer, "Scanning tunneling microscopy contrast in lateral Ge-Si nanostructures on Si(111)–V3×V3–Bi," *Phys. Rev. B*, vol. 81, no. 24, p. 245427, Jun. 2010, doi:10.1103/PhysRevB.81.245427.

[92]   M. Kawamura, N. Paul, V. Cherepanov, and B. Voigtländer, "Nanowires and Nanorings at the Atomic Level," *Phys. Rev. Lett.*, vol. 91, no. 9, p. 096102, Aug. 2003, doi:10.1103/PhysRevLett.91.096102.

[93]   S. Korte, K. Romanyuk, B. Schnitzler, V. Cherepanov, B. Voigtländer, and S. N. Filimonov, "Selective Adsorption of C60 on Ge/Si Nanostructures," *Phys. Rev. Lett.*, vol. 108, no. 11, p. 116101, Mar. 2012, doi:10.1103/PhysRevLett.108.116101.

[94]   R. M. Feenstra, J. A. Stroscio, J. Tersoff, and A. P. Fein, "Atom-selective imaging of the GaAs(110) surface," *Phys. Rev. Lett.*, vol. 58, no. 12, pp. 1192–1195, Mar. 1987, doi:10.1103/PhysRevLett.58.1192.

[95]   M. Schmid, H. Stadler, and P. Varga, "Direct observation of surface chemical order by scanning tunneling microscopy," *Phys. Rev. Lett.*, vol. 70, no. 10, pp. 1441–1444, Mar. 1993, doi:10.1103/PhysRevLett.70.1441.

[96]   B. Voigtländer, V. Scheuch, H. P. Bonzel, S. Heinze, and S. Blügel, "Chemical identification of atoms at multicomponent surfaces on an atomic scale: CoSi2(100)," *Phys. Rev. B*, vol. 55, no. 20, pp. R13444–R13447, May 1997, doi:10.1103/PhysRevB.55.R13444.

[97]   A. Stróżecka, K. Muthukumar, J. A. Larsson, A. Dybek, T. J. S. Dennis, J. Mysliveček, and B. Voigtländer, "Electron-induced excitation of vibrations of Ce atoms inside a C80 cage," *Phys. Rev. B*, vol. 83, no. 16, p. 165414, Apr. 2011, doi:10.1103/PhysRevB.83.165414.

[98]   A. Stróżecka, K. Muthukumar, A. Dybek, T. J. Dennis, J. A. Larsson, J. Mysliveček, and B. Voigtländer, "Modification of the conductance of single fullerene molecules by endohedral doping," *Appl. Phys. Lett.*, vol. 95, no. 13, p. 133118, 2009, doi:10.1063/1.3236529.

[99]   H. J. Lee and W. Ho, "Structural determination by single-molecule vibrational spectroscopy and microscopy: Contrast between copper and iron carbonyls," *Phys. Rev. B*, vol. 61, no. 24, pp. R16347–R16350, Jun. 2000, doi:10.1103/PhysRevB.61.R16347.

[100] J. R. Hahn and W. Ho, "Oxidation of a Single Carbon Monoxide Molecule Manipulated and Induced with a Scanning Tunneling Microscope," *Phys. Rev. Lett.*, vol. 87, no. 16, p. 166102, Sep. 2001, doi:10.1103/PhysRevLett.87.166102.

[101] R. Schaub, E. Wahlström, A. Ronnau, E. Laegsgaard, I. Stensgaard, and F. Besenbacher, "Oxygen-Mediated Diffusion of Oxygen Vacancies on the TiO2(110) Surface," *Science*, vol. 299, no. 5605, pp. 377–379, Jan. 2003, doi:10.1126/science.1078962.

[102] S. Wendt, J. Matthiesen, R. Schaub, E. K. Vestergaard, E. Lægsgaard, F. Besenbacher, and B. Hammer, "Formation and Splitting of Paired Hydroxyl Groups on Reduced TiO2(110)," *Phys. Rev. Lett.*, vol. 96, no. 6, p. 066107, Feb. 2006, doi:10.1103/PhysRevLett.96.066107.

[103] S. Wendt, R. Schaub, J. Matthiesen, E. K. Vestergaard, E. Wahlström, M. D. Rasmussen, P. Thostrup, L. M. Molina, E. Lægsgaard, I. Stensgaard, B. Hammer, and F. Besenbacher, "Oxygen vacancies on TiO2(110) and their interaction with H2O and O2: A combined high-resolution STM and DFT study," *Surf. Sci.*, vol. 598, no. 1–3, pp. 226–245, Dec. 2005, doi:10.1016/j.susc.2005.08.041.

[104] J. V Barth, G. Costantini, and K. Kern, "Engineering atomic and molecular nanostructures at surfaces," *Nature*, vol. 437, no. 7059, pp. 671–679, Sep. 2005, doi:10.1038/nature04166.

[105] W. K. Burton, N. Cabrera, and F. C. Frank, "The Growth of Crystals and the Equilibrium Structure of their Surfaces," *Philos. Trans. R. Soc. A Math. Phys. Eng. Sci.*, vol. 243, no. 866, pp. 299–358, Jun. 1951, doi:10.1098/rsta.1951.0006.

[106] Y.-W. Mo, D. E. Savage, B. S. Swartzentruber, and M. G. Lagally, "Kinetic pathway in Stranski-Krastanov growth of Ge on Si(001)," *Phys. Rev. Lett.*, vol. 65, no. 8, pp. 1020–1023, Aug. 1990, doi:10.1103/PhysRevLett.65.1020.

[107] G. Haas, A. Menck, H. Brune, J. V. Barth, J. A. Venables, and K. Kern, "Nucleation and growth of supported clusters at defect sites: Pd/MgO(001)," *Phys. Rev. B*, vol. 61, no. 16, pp. 11105–11108, Apr. 2000, doi:10.1103/PhysRevB.61.11105.

[108] K. Romanyuk, J. Mysliveček, V. Cherepanov, T. Sekiguchi, S. Yoshida, K. Itoh, and B. Voigtländer, "Optimized Ge nanowire arrays on Si by modified surfactant mediated epitaxy," *Phys. Rev. B*, vol. 75, no. 24, p. 241309, Jun. 2007, doi:10.1103/PhysRevB.75.241309.

[109] B. Voigtländer, "Fundamental processes in Si/Si and Ge/Si epitaxy studied by scanning tunneling microscopy during growth," *Surf. Sci. Rep.*, vol. 43, no. 5–8, pp. 127–254, Sep. 2001, doi:10.1016/S0167-5729(01)00012-7.

[110] A. Emundts, P. Coenen, G. Pirug, B. Voigtländer, H. P. Bonzel, and P. Wynblatt, "Combination of a Besocke-type scanning tunneling microscope with a scanning electron microscope," *Rev. Sci. Instrum.*, vol. 72, no. 9, p. 3546, 2001, doi:10.1063/1.1392341.

[111] J. A. Venables, "Atomic processes in crystal growth," *Surf. Sci.*, vol. 299–300, no. 1–3, pp. 798–817, Jan. 1994, doi:10.1016/0039-6028(94)90698-X.

[112] G. Ehrlich, "Atomic View of Surface Self-Diffusion: Tungsten on Tungsten," *J. Chem. Phys.*, vol. 44, no. 3, p. 1039, 1966, doi:10.1063/1.1726787.

[113] H. Brune, G. S. Bales, J. Jacobsen, C. Boragno, and K. Kern, "Measuring surface diffusion from nucleation island densities," *Phys. Rev. B*, vol. 60, no. 8, pp. 5991–6006, Aug. 1999, doi:10.1103/PhysRevB.60.5991.

[114] T. Shitara, D. D. Vvedensky, M. R. Wilby, J. Zhang, J. H. Neave, and B. A. Joyce, "Step-density variations and reflection high-energy electron-diffraction intensity oscillations during epitaxial growth on vicinal GaAs(001)," *Phys. Rev. B*, vol. 46, no. 11, pp. 6815–6824, Sep. 1992, doi:10.1103/PhysRevB.46.6815.

[115] J. A. Stroscio, D. T. Pierce, and R. A. Dragoset, "Homoepitaxial growth of iron and a real space view of reflection-high-energy-electron diffraction," *Phys. Rev. Lett.*, vol. 70, no. 23, pp. 3615–3618, Jun. 1993, doi:10.1103/PhysRevLett.70.3615.

[116] J. A. Stroscio and D. T. Pierce, "Scaling of diffusion-mediated island growth in iron-on-iron homoepitaxy," *Phys. Rev. B*, vol. 49, no. 12, pp. 8522–8525, Mar. 1994, doi:10.1103/PhysRevB.49.8522.

[117] R. L. Schwoebel and E. J. Shipsey, "Step Motion on Crystal Surfaces," *J. Appl. Phys.*, vol. 37, no. 10, p. 3682, 1966, doi:10.1063/1.1707904.

[118] G. S. Bales and A. Zangwill, "Morphological instability of a terrace edge during step-flow growth," *Phys. Rev. B*, vol. 41, no. 9, pp. 5500–5508, Mar. 1990, doi:10.1103/PhysRevB.41.5500.

[119] J. Villain, "Continuum models of crystal growth from atomic beams with and without desorption," *J. Phys. I*, vol. 1, no. 1, pp. 19–42, Jan. 1991, doi:10.1051/jp1:1991114.

[120] A. Gocalinska, M. Manganaro, E. Pelucchi, and D. D. Vvedensky, "Surface organization of homoepitaxial InP films grown by metalorganic vapor-phase epitaxy," *Phys. Rev. B*, vol. 86, no. 16, p. 165307, Oct. 2012, doi:10.1103/PhysRevB.86.165307.

[121] T. Maroutian, L. Douillard, and H.-J. Ernst, "Morphological instability of Cu vicinal surfaces during step-flow growth," *Phys. Rev. B*, vol. 64, no. 16, p. 165401, Sep. 2001, doi:10.1103/PhysRevB.64.165401.

[122] M. Kalff, P. Šmilauer, G. Comsa, and T. Michely, "No coarsening in Pt(111) homoepitaxy," *Surf. Sci.*, vol. 426, no. 3, pp. L447–L453, May 1999, doi:10.1016/S0039-6028(99)00351-9.

[123] H. Brune, C. Romainczyk, H. Röder, and K. Kern, "Mechanism of the transition from fractal to dendritic growth of surface aggregates," *Nature*, vol. 369, no. 6480, pp. 469–471, Jun. 1994, doi:10.1038/369469a0.

[124] M. Kalff, G. Comsa, and T. Michely, "Temperature dependent morphological evolution of Pt(111) by ion erosion: destabilization, phase coexistence and coarsening," *Surf. Sci.*, vol. 486, no. 1–2, pp. 103–135, 2001, doi:10.1016/S0039-6028(01)01015-9.

[125] H. Brune, H. Röder, C. Romainczyk, C. Boragno, and K. Kern, "Aggregation of fractal and endritic Ag clusters on a Pt(111) surface," *Appl. Phys. A Mater. Sci. Process.*, vol. 60, no. 2, pp. 167–171, Feb. 1995, doi:10.1007/BF01538242.

[126] T. Luttrell, W.-K. Li, X.-Q. Gong, and M. Batzill, "New Directions for Atomic Steps: Step Alignment by Grazing Incident Ion Beams on TiO2(110)," *Phys. Rev. Lett.*, vol. 102, no. 16, p. 166103, Apr. 2009, doi:10.1103/PhysRevLett.102.166103.

[127] B. S. Swartzentruber, Y.-W. Mo, R. Kariotis, M. G. Lagally, and M. B. Webb, "Direct determination of step and kink energies on vicinal Si(001)," *Phys. Rev. Lett.*, vol. 65, no. 15, pp. 1913–1916, Oct. 1990, doi:10.1103/PhysRevLett.65.1913.

[128] J. A. Kubby and J. J. Boland, "Scanning tunneling microscopy of semiconductor surfaces," *Surf. Sci. Rep.*, vol. 26, no. 3–6, pp. 61–204, Dec. 1996, doi:10.1016/S0167-5729(97)80001-5.

[129] J. Mysliveček, C. Schelling, F. Schäffler, G. Springholz, P. Šmilauer, J. Krug, and B. Voigtländer, "On the microscopic origin of the kinetic step bunching instability on vicinal Si(001)," *Surf. Sci.*, vol. 520, no. 3, pp. 193–206, Dec. 2002, doi:10.1016/S0039-6028(02)02273-2.

[130] C. Schelling, G. Springholz, and F. Schäffler, "Kinetic Growth Instabilities on Vicinal Si(001) Surfaces," *Phys. Rev. Lett.*, vol. 83, no. 5, pp. 995–998, Aug. 1999, doi:10.1103/PhysRevLett.83.995.

[131] B. Voigtländer, T. Weber, P. Šmilauer, and D. E. Wolf, "Transition from Island Growth to Step-Flow Growth for Si/Si(100) Epitaxy," *Phys. Rev. Lett.*, vol. 78, no. 11, pp. 2164–2167, Mar. 1997, doi:10.1103/PhysRevLett.78.2164.

[132] I. Berbezier and A. Ronda, "SiGe nanostructures," *Surf. Sci. Rep.*, vol. 64, no. 2, pp. 47–98, Feb. 2009, doi:10.1016/j.surfrep.2008.09.003.

[133] J. Stangl, V. Holý, and G. Bauer, "Structural properties of self-organized semiconductor nanostructures," *Rev. Mod. Phys.*, vol. 76, no. 3, pp. 725–783, Sep. 2004, doi:10.1103/RevModPhys.76.725.

[134] W. Peng, Z. Aksamija, S. A. Scott, J. J. Endres, D. E. Savage, I. Knezevic, M. A. Eriksson, and M. G. Lagally, "Probing the electronic structure at semiconductor surfaces using charge transport in nanomembranes," *Nat. Commun.*, vol. 4, p. 1339, Jan. 2013, doi:10.1038/ncomms2350.

[135] M. Copel, M. C. Reuter, M. Horn von Hoegen, and R. M. Tromp, "Influence of surfactants in Ge and Si epitaxy on Si(001)," *Phys. Rev. B*, vol. 42, no. 18, pp. 11682–11689, Dec. 1990, doi:10.1103/PhysRevB.42.11682.

[136] S. Tanaka, S. Iwai, and Y. Aoyagi, "Self-assembling GaN quantum dots on AlxGa1−xN surfaces using a surfactant," *Appl. Phys. Lett.*, vol. 69, no. 26, p. 4096, 1996, doi:10.1063/1.117830.

[137] V. Cherepanov, S. Filimonov, J. Mysliveček, and B. Voigtländer, "Scaling of submonolayer island sizes in surfactant-mediated epitaxy of semiconductors," *Phys. Rev. B*, vol. 70, no. 8, p. 085401, Aug. 2004, doi:10.1103/PhysRevB.70.085401.

[138] D. Kandel and E. Kaxiras, "Surfactant Mediated Crystal Growth of Semiconductors," *Phys. Rev. Lett.*, vol. 75, no. 14, pp. 2742–2745, Oct. 1995, doi:10.1103/PhysRevLett.75.2742.

[139] J. W. Evans, P. A. Thiel, and M. C. Bartelt, "Morphological evolution during epitaxial thin film growth: Formation of 2D islands and 3D mounds," *Surf. Sci. Rep.*, vol. 61, no. 1–2, pp. 1–128, 2006, doi:10.1016/j.surfrep.2005.08.004.

[140] M. Fanfoni and M. Tomellini, "Film growth viewed as stochastic dot processes," *J. Phys. Condens. Matter*, vol. 17, no. 17, pp. R571–R605, May 2005, doi:10.1088/0953-8984/17/17/R02.

[141] F. Ratto and F. Rosei, "Order and disorder in the heteroepitaxy of semiconductor nanostructures," *Mater. Sci. Eng. R Reports*, vol. 70, no. 3–6, pp. 243–264, Nov. 2010, doi:10.1016/j.mser.2010.06.011.

[142] S. Just, M. Blab, S. Korte, V. Cherepanov, H. Soltner, and B. Voigtländer, "Surface and Step Conductivities on Si(111) Surfaces," *Phys. Rev. Lett.*, vol. 115, no. 6, p. 066801, Aug. 2015, doi:10.1103/PhysRevLett.115.066801.

[143] J. Tersoff and F. K. LeGoues, "Competing relaxation mechanisms in strained layers," *Phys. Rev. Lett.*, vol. 72, no. 22, pp. 3570–3573, May 1994, doi:10.1103/PhysRevLett.72.3570.

[144] M. Meixner, E. Schöll, M. Schmidbauer, H. Raidt, and R. Köhler, "Formation of island chains in SiGe/Si heteroepitaxy by elastic anisotropy," *Phys. Rev. B*, vol. 64, no. 24, p. 245307, Nov. 2001, doi:10.1103/PhysRevB.64.245307.

[145] D. D. Chambliss, R. J. Wilson, and S. Chiang, "Nucleation of ordered Ni island arrays on Au(111) by surface-lattice dislocations," *Phys. Rev. Lett.*, vol. 66, no. 13, pp. 1721–1724, Apr. 1991, doi:10.1103/PhysRevLett.66.1721.

[146] K. Kern, H. Brune, M. Giovannini, and K. Bromann, "Self-organized growth of nanostructure arrays on strain-relief patterns," *Nature*, vol. 394, no. 6692, pp. 451–453, 1998, doi:10.1038/28804.

[147] T. Jarolímek, J. Mysliveček, P. Sobotík, and I. Ošťádal, "Adsorption and diffusion of Ag atoms on Si(111)-(7×7) surface," *Surf. Sci.*, vol. 482–485, pp. 386–390, Jun. 2001, doi:10.1016/S0039-6028(00)01039-6.

[148] J. Mysliveček, P. Sobotík, I. Ošťádal, T. Jarolímek, and P. Šmilauer, "Unconventional features of Ag epitaxy on the Si(111)7×7 surface," *Phys. Rev. B*, vol. 63, no. 4, p. 045403, Jan. 2001, doi:10.1103/PhysRevB.63.045403.

[149] K. Takayanagi, "Structural analysis of Si(111)-7×7 by UHV-transmission electron diffraction and microscopy," *J. Vac. Sci. Technol. A Vacuum, Surfaces, Film.*, vol. 3, no. 3, p. 1502, May 1985, doi:10.1116/1.573160.

[150] O. Custance, S. Brochard, I. Brihuega, E. Artacho, J. M. Soler, A. M. Baró, and J. M. Gómez-Rodríguez, "Single adatom adsorption and diffusion on Si(111)–7×7 surfaces: Scanning tunneling microscopy and first-principles calculations," *Phys. Rev. B*, vol. 67, no. 23, p. 235410, Jun. 2003, doi:10.1103/PhysRevB.67.235410.

[151] C. Zhang, G. Chen, K. Wang, H. Yang, T. Su, C. T. Chan, M. M. T. Loy, and X. Xiao, "Experimental and Theoretical Investigation of Single Cu, Ag, and Au Atoms Adsorbed on Si(111)–(7×7)," *Phys. Rev. Lett.*, vol. 94, no. 17, p. 176104, May 2005, doi:10.1103/PhysRevLett.94.176104.

[152] J.-L. Li, J.-F. Jia, X.-J. Liang, X. Liu, J.-Z. Wang, Q.-K. Xue, Z.-Q. Li, J. S. Tse, Z. Zhang, and S. B. Zhang, "Spontaneous Assembly of Perfectly Ordered Identical-Size Nanocluster Arrays," *Phys. Rev. Lett.*, vol. 88, no. 6, p. 066101, Jan. 2002, doi:10.1103/PhysRevLett.88.066101.

[153] A. T. N'Diaye, T. Gerber, C. Busse, J. Mysliveček, J. Coraux, and T. Michely, "A versatile fabrication method for cluster superlattices," *New J. Phys.*, vol. 11, no. 10, p. 103045, Oct. 2009, doi:10.1088/1367-2630/11/10/103045.

[154] K. S. Novoselov, "Nobel Lecture: Graphene: Materials in the Flatland," *Rev. Mod. Phys.*, vol. 83, no. 3, pp. 837–849, Aug. 2011, doi:10.1103/RevModPhys.83.837.

[155] A. T. N'Diaye, S. Bleikamp, P. J. Feibelman, and T. Michely, "Two-Dimensional Ir Cluster Lattice on a Graphene Moiré on Ir(111)," *Phys. Rev. Lett.*, vol. 97, no. 21, p. 215501, Nov. 2006, doi:10.1103/PhysRevLett.97.215501.

[156] M. Batzill, "The surface science of graphene: Metal interfaces, CVD synthesis, nanoribbons, chemical modifications, and defects," *Surf. Sci. Rep.*, vol. 67, no. 3–4, pp. 83–115, Mar. 2012, doi:10.1016/j.surfrep.2011.12.001.

[157] S. Bai and X. Shen, "Graphene–inorganic nanocomposites," *RSC Adv.*, vol. 2, no. 1, pp. 64–98, 2012, doi:10.1039/C1RA00260K.

[158] A. Trovarelli and P. Fornasiero, *Catalysis by ceria and related materials*, 2nd ed. Singapore: World Scientific, 2013.

[159] J. Kašpar, P. Fornasiero, and M. Graziani, "Use of CeO2-based oxides in the three-way catalysis," *Catal. Today*, vol. 50, no. 2, pp. 285–298, Apr. 1999, doi:10.1016/S0920-5861(98)00510-0.

[160] H. S. Gandhi, G. W. Graham, and R. W. McCabe, "Automotive exhaust catalysis," *J. Catal.*, vol. 216, no. 1–2, pp. 433–442, 2003, doi:10.1016/S0021-9517(02)00067-2.

[161] R. Farrauto, S. Hwang, L. Shore, W. Ruettinger, J. Lampert, T. Giroux, Y. Liu, and O. Ilinich, "New Material Needs for Hydrocarbon Fuel Processing: Generating Hydrogen for the PEM Fuel Cell," *Annu. Rev. Mater. Res.*, vol. 33, no. 1, pp. 1–27, Aug. 2003, doi:10.1146/annurev.matsci.33.022802.091348.

[162] C. Ratnasamy and J. P. Wagner, "Water Gas Shift Catalysis," *Catal. Rev.*, vol. 51, no. 3, pp. 325–440, Sep. 2009, doi:10.1080/01614940903048661.

[163] S. D. Senanayake, D. Stacchiola, and J. A. Rodriguez, "Unique Properties of Ceria Nanoparticles Supported on Metals: Novel Inverse Ceria/Copper Catalysts for CO Oxidation and the Water-Gas Shift Reaction," *Acc. Chem. Res.*, vol. 46, no. 8, pp. 1702–1711, Aug. 2013, doi:10.1021/ar300231p.

[164] C. Tang, H. Zhang, and L. Dong, "Ceria-based catalysts for low-temperature selective catalytic reduction of NO with NH3," *Catal. Sci. Technol.*, vol. 6, no. 5, pp. 1248–1264, 2016, doi:10.1039/C5CY01487E.

[165] A. Hernández-Giménez, D. Castelló, and A. Bueno-López, "Diesel soot combustion catalysts: review of active phases," *Chem. Pap.*, vol. 68, no. 9, Jan. 2014, doi:10.2478/s11696-013-0469-7.

[166] L. Vivier and D. Duprez, "Ceria-based solid catalysts for organic chemistry," *ChemSusChem*, vol. 3, no. 6, pp. 654–678, 2010, doi:10.1002/cssc.201000054.

[167] J. T. Miller, A. J. Kropf, Y. Zha, J. R. Regalbuto, L. Delannoy, C. Louis, E. Bus, and J. A. van Bokhoven, "The effect of gold particle size on AuAu bond length and reactivity toward oxygen in supported catalysts," *J. Catal.*, vol. 240, no. 2, pp. 222–234, Jun. 2006, doi:10.1016/j.jcat.2006.04.004.

[168] J. A. Rodriguez, "Gold-based catalysts for the water–gas shift reaction: Active sites and reaction mechanism," *Catal. Today*, vol. 160, no. 1, pp. 3–10, Feb. 2011, doi:10.1016/j.cattod.2010.06.030.

[169] M. S. Hegde, G. Madras, and K. C. Patil, "Noble metal ionic catalysts," *Acc. Chem. Res.*, vol. 42, no. 6, pp. 704–712, 2009, doi:10.1021/ar800209s.

[170] M. Flytzani-Stephanopoulos and B. C. Gates, "Atomically Dispersed Supported Metal Catalysts," *Annu. Rev. Chem. Biomol. Eng.*, vol. 3, no. 1, pp. 545–574, 2012, doi:10.1146/annurev-chembioeng-062011-080939.

[171] R. M. Ormerod, "Solid oxide fuel cells," *Chem. Soc. Rev.*, vol. 32, no. 1, pp. 17–28, Dec. 2003, doi:10.1039/b105764m.

[172] D. J. L. Brett, A. Atkinson, N. P. Brandon, and S. J. Skinner, "Intermediate temperature solid oxide fuel cells," *Chem. Soc. Rev.*, vol. 37, no. 8, p. 1568, 2008, doi:10.1039/b612060c.

[173] W. C. Chueh, C. Falter, M. Abbott, D. Scipio, P. Furler, S. M. Haile, and A. Steinfeld, "High-Flux Solar-Driven Thermochemical Dissociation of CO2 and H2O Using Nonstoichiometric Ceria," *Science*, vol. 330, no. 6012, pp. 1797–1801, Dec. 2010, doi:10.1126/science.1197834.

[174] J. R. Scheffe and A. Steinfeld, "Oxygen exchange materials for solar thermochemical splitting of H2O and CO2: a review," *Mater. Today*, vol. 17, no. 7, pp. 341–348, 2014, doi:10.1016/j.mattod.2014.04.025.

[175] D. R. Mullins, P. V. Radulovic, and S. H. Overbury, "Ordered cerium oxide thin films grown on Ru(0001) and Ni(111)," *Surf. Sci.*, vol. 429, no. 1–3, pp. 186–198, Jun. 1999, doi:10.1016/S0039-6028(99)00369-6.

[176] J.-L. Lu, H.-J. Gao, S. Shaikhutdinov, and H.-J. Freund, "Morphology and defect structure of the CeO2(111) films grown on Ru(0001) as studied by scanning tunneling microscopy," *Surf. Sci.*, vol. 600, no. 22, pp. 5004–5010, Nov. 2006, doi:10.1016/j.susc.2006.08.023.

[177] B. Kaemena, S. D. Senanayake, A. Meyer, J. T. Sadowski, J. Falta, and J. I. Flege, "Growth and Morphology of Ceria on Ruthenium (0001)," *J. Phys. Chem. C*, vol. 117, no. 1, pp. 221–232, Jan. 2013, doi:10.1021/jp3081782.

[178] U. Berner and K.-D. Schierbaum, "Cerium oxides and cerium-platinum surface alloys on Pt(111) single-crystal surfaces studied by scanning tunneling microscopy," *Phys. Rev. B*, vol. 65, no. 23, p. 235404, May 2002, doi:10.1103/PhysRevB.65.235404.

[179] D. C. Grinter, R. Ithnin, C. L. Pang, and G. Thornton, "Defect Structure of Ultrathin Ceria Films on Pt(111): Atomic Views from Scanning Tunnelling Microscopy," *J. Phys. Chem. C*, vol. 114, no. 40, pp. 17036–17041, Oct. 2010, doi:10.1021/jp102895k.

[180] P. Luches, F. Pagliuca, and S. Valeri, "Structural and morphological modifications in thermally reduced cerium oxide ultrathin epitaxial films on Pt(111)," *Phys. Chem. Chem. Phys.*, vol. 16, no. 111, pp. 18848–18857, 2014, doi:10.1039/C4CP02723J.

[181] S. Ma, X. Zhao, J. A. Rodriguez, and J. Hrbek, "STM and XPS Study of Growth of Ce on Au(111)," *J. Phys. Chem. C*, vol. 111, no. 9, pp. 3685–3691, Mar. 2007, doi:10.1021/jp064366v.

[182] M. Baron, O. Bondarchuk, D. Stacchiola, S. Shaikhutdinov, and H.-J. Freund, "Interaction of Gold with Cerium Oxide Supports: CeO2(111) Thin Films vs CeOx Nanoparticles," *J. Phys. Chem. C*, vol. 113, no. 15, pp. 6042–6049, Apr. 2009, doi:10.1021/jp9001753.

[183] S. D. Senanayake, J. Zhou, A. P. Baddorf, and D. R. Mullins, "The reaction of carbon monoxide with palladium supported on cerium oxide thin films," *Surf. Sci.*, vol. 601, no. 15, pp. 3215–3223, Aug. 2007, doi:10.1016/j.susc.2007.05.037.

[184] J. Schoiswohl, S. Surnev, and F. P. Netzer, "Reactions on Inverse Model Catalyst Surfaces: Atomic Views by STM," *Top. Catal.*, vol. 36, no. 1–4, pp. 91–105, Aug. 2005, doi:10.1007/s11244-005-7865-3.

[185] S. Surnev, A. Fortunelli, and F. P. Netzer, "Structure-property relationship and chemical aspects of oxide-metal hybrid nanostructures.," *Chem. Rev.*, vol. 113, no. 6, pp. 4314–72, Jun. 2013, doi:10.1021/cr300307n.

[186] F. P. Netzer, "'Small and beautiful' – The novel structures and phases of nano-oxides," *Surf. Sci.*, vol. 604, no. 5–6, pp. 485–489, Mar. 2010, doi:10.1016/j.susc.2010.01.002.

[187] L. Szabová, O. Stetsovych, F. Dvořák, M. Farnesi Camellone, S. Fabris, J. Mysliveček, and V. Matolín, "Distinct Physicochemical Properties of the First Ceria Monolayer on Cu(111)," *J. Phys. Chem. C*, vol. 116, no. 11, pp. 6677–6684, Mar. 2012, doi:10.1021/jp211955v.

[188] O. Stetsovych, F. Dvořák, L. Szabová, S. Fabris, J. Mysliveček, and V. Matolín, "Nanometer-Range Strain Distribution in Layered Incommensurate Systems," *Phys. Rev. Lett.*, vol. 109, no. 26, p. 266102, Dec. 2012, doi:10.1103/PhysRevLett.109.266102.

[189] S. Torbrügge, M. Cranney, and M. Reichling, "Morphology of step structures on CeO2(111)," *Appl. Phys. Lett.*, vol. 93, no. 7, p. 073112, 2008, doi:10.1063/1.2969790.

[190] P. Luches, F. Pagliuca, S. Valeri, and F. Boscherini, "Structure of Ultrathin CeO2 Films on Pt(111) by Polarization-Dependent X-ray Absorption Fine Structure," *J. Phys. Chem. C*, vol. 117, no. 2, pp. 1030–1036, Jan. 2013, doi:10.1021/jp310375t.

[191] G. Niu, M. H. Zoellner, T. Schroeder, A. Schaefer, J.-H. Jhang, V. Zielasek, M. Bäumer, H. Wilkens, J. Wollschläger, R. Olbrich, C. Lammers, and M. Reichling, "Controlling the physics and chemistry of binary and ternary praseodymium and cerium oxide systems," *Phys. Chem. Chem. Phys.*, vol. 17, no. 38, pp. 24513–24540, 2015, doi:10.1039/C5CP02283E.

[192] S. Agnoli, A. E. Reeder, S. D. Senanayake, J. Hrbek, and J. A. Rodriguez, "Structure and special chemical reactivity of interface-stabilized cerium oxide nanolayers on TiO2 (110)," *Nanoscale*, vol. 6, no. 2, pp. 800–810, 2014, doi:10.1039/C3NR04623K.

[193] L. Ma, N. Doudin, S. Surnev, G. Barcaro, L. Sementa, A. Fortunelli, and F. P. Netzer, "Lattice Strain Defects in a Ceria Nanolayer," *J. Phys. Chem. Lett.*, vol. 7, no. 7, pp. 1303–1309, Apr. 2016, doi:10.1021/acs.jpclett.6b00253.

[194] R. Streber, C. Papp, M. P. A. Lorenz, A. Bayer, R. Denecke, and H.-P. Steinrück, "Sulfur Oxidation on Pt(355): It Is the Steps!," *Angew. Chemie Int. Ed.*, vol. 48, no. 51, pp. 9743–9746, Dec. 2009, doi:10.1002/anie.200904488.

[195] R. T. Vang, K. Honkala, S. Dahl, E. K. Vestergaard, J. Schnadt, E. Lægsgaard, B. S. Clausen, J. K. Nørskov, and F. Besenbacher, "Controlling the catalytic bond-breaking selectivity of Ni surfaces by step blocking," *Nat. Mater.*, vol. 4, no. 2, pp. 160–162, Feb. 2005, doi:10.1038/nmat1311.

[196] X.-Q. Gong, A. Selloni, M. Batzill, and U. Diebold, "Steps on anatase TiO2(101)," *Nat. Mater.*, vol. 5, no. 8, pp. 665–670, Aug. 2006, doi:10.1038/nmat1695.

[197] X. Gong, A. Selloni, O. Dulub, P. Jacobson, and U. Diebold, "Small Au and Pt Clusters at the Anatase TiO2(101) Surface: Behavior at Terraces, Steps, and Surface Oxygen Vacancies," *J. Am. Chem. Soc.*, vol. 130, no. 1, pp. 370–381, Jan. 2008, doi:10.1021/ja0773148.

[198] M. Setvin, X. Hao, B. Daniel, J. Pavelec, Z. Novotny, G. S. Parkinson, M. Schmid, G. Kresse, C. Franchini, and U. Diebold, "Charge trapping at the step edges of TiO2 anatase (101)," *Angew. Chemie - Int. Ed.*, vol. 53, no. 18, pp. 4714–4716, 2014, doi:10.1002/anie.201309796.

[199] N. Nilius, S. M. Kozlov, J.-F. Jerratsch, M. Baron, X. Shao, F. Viñes, S. Shaikhutdinov, K. M. Neyman, and H.-J. Freund, "Formation of One-Dimensional Electronic States along the Step Edges of CeO2(111)," *ACS Nano*, vol. 6, no. 2, pp. 1126–1133, Feb. 2012, doi:10.1021/nn2036472.

[200] S. M. Kozlov, F. Viñes, N. Nilius, S. Shaikhutdinov, and K. M. Neyman, "Absolute Surface Step Energies: Accurate Theoretical Methods Applied to Ceria Nanoislands," *J. Phys. Chem. Lett.*, vol. 3, no. 15, pp. 1956–1961, Aug. 2012, doi:10.1021/jz3006942.

[201] S. M. Kozlov and K. M. Neyman, "O vacancies on steps on the CeO2(111) surface," *Phys. Chem. Chem. Phys.*, vol. 16, no. 17, p. 7823, May 2014, doi:10.1039/c4cp00136b.

[202] F. Dvořák, O. Stetsovych, M. Steger, E. Cherradi, I. Matolínová, N. Tsud, M. Škoda, T. Skála, J. Mysliveček, and V. Matolín, "Adjusting Morphology and Surface Reduction of CeO2(111) Thin Films on Cu(111)," *J. Phys. Chem. C*, vol. 115, no. 15, pp. 7496–7503, Apr. 2011, doi:10.1021/jp1121646.

[203] R. Kunkel, B. Poelsema, L. K. Verheij, and G. Comsa, "Reentrant layer-by-layer growth during molecular-beam epitaxy of metal-on-metal substrates," *Phys. Rev. Lett.*, vol. 65, no. 6, pp. 733–736, Aug. 1990, doi:10.1103/PhysRevLett.65.733.

[204] P. Šmilauer, M. R. Wilby, and D. D. Vvedensky, "Reentrant layer-by-layer growth: A numerical study," *Phys. Rev. B*, vol. 47, no. 7, pp. 4119–4122, Feb. 1993, doi:10.1103/PhysRevB.47.4119.

[205] N. Skorodumova, S. Simak, B. Lundqvist, I. Abrikosov, and B. Johansson, "Quantum Origin of the Oxygen Storage Capability of Ceria," *Phys. Rev. Lett.*, vol. 89, no. 16, p. 166601, Sep. 2002, doi:10.1103/PhysRevLett.89.166601.

[206] F. Esch, S. Fabris, L. Zhou, T. Montini, C. Africh, P. Fornasiero, G. Comelli, and R. Rosei, "Electron Localization Determines Defect Formation on Ceria Substrates," *Science*, vol. 309, no. 5735, pp. 752–755, 2005, doi:10.1126/science.1111568.

[207] M. V. Ganduglia-Pirovano, A. Hofmann, and J. Sauer, "Oxygen vacancies in transition metal and rare earth oxides: Current state of understanding and remaining challenges," *Surf. Sci. Rep.*, vol. 62, no. 6, pp. 219–270, Jun. 2007, doi:10.1016/j.surfrep.2007.03.002.

[208] J. Paier, C. Penschke, and J. Sauer, "Oxygen Defects and Surface Chemistry of Ceria: Quantum Chemical Studies Compared to Experiment," *Chem. Rev.*, vol. 113, no. 6, pp. 3949–3985, Jun. 2013, doi:10.1021/cr3004949.

[209] S. D. Senanayake, D. Stacchiola, J. Evans, M. Estrella, L. Barrio, M. Pérez, J. Hrbek, and J. A. Rodriguez, "Probing the reaction intermediates for the water–gas shift over inverse CeOx/Au(111) catalysts," *J. Catal.*, vol. 271, no. 2, pp. 392–400, May 2010, doi:10.1016/j.jcat.2010.02.024.

[210] Y. Lykhach, V. Johánek, H. A. Aleksandrov, S. M. Kozlov, M. Happel, T. Skála, P. St. Petkov, N. Tsud, G. N. Vayssilov, K. C. Prince, K. M. Neyman, V. Matolín, and J. Libuda, "Water Chemistry on Model Ceria and Pt/Ceria Catalysts," *J. Phys. Chem. C*, vol. 116, no. 22, pp. 12103–12113, Jun. 2012, doi:10.1021/jp302229x.

[211] G. D. Wang, D. D. Kong, Y. H. Pan, H. B. Pan, and J. F. Zhu, "Low energy Ar-ion bombardment effects on the CeO2 surface," *Appl. Surf. Sci.*, vol. 258, no. 6, pp. 2057–2061, Jan. 2012, doi:10.1016/j.apsusc.2011.04.103.

[212] S. Torbrügge, M. Reichling, A. Ishiyama, S. Morita, and Ó. Custance, "Evidence of Subsurface Oxygen Vacancy Ordering on Reduced CeO2(111)," *Phys. Rev. Lett.*, vol. 99, no. 5, p. 056101, Aug. 2007, doi:10.1103/PhysRevLett.99.056101.

[213] V. Stetsovych, F. Pagliuca, F. Dvořák, T. Duchoň, M. Vorokhta, M. Aulická, J. Lachnitt, S. Schernich, I. Matolínová, K. Veltruská, T. Skála, D. Mazur, J. Mysliveček, J. Libuda, and V. Matolín, "Epitaxial Cubic Ce2O3 Films via Ce–CeO2 Interfacial Reaction," *J. Phys. Chem. Lett.*, vol. 4, no. 6, pp. 866–871, Mar. 2013, doi:10.1021/jz400187j.

[214] T. Duchoň, F. Dvořák, M. Aulická, V. Stetsovych, M. Vorokhta, D. Mazur, K. Veltruská, T. Skála, J. Mysliveček, I. Matolínová, and V. Matolín, "Ordered Phases of Reduced Ceria As Epitaxial Films on Cu(111)," *J. Phys. Chem. C*, vol. 118, no. 1, pp. 357–365, Jan. 2014, doi:10.1021/jp409220p.

[215] T. Duchoň, F. Dvořák, M. Aulická, V. Stetsovych, M. Vorokhta, D. Mazur, K. Veltruská, T. Skála, J. Mysliveček, I. Matolínová, and V. Matolín, "Comment on 'Ordered Phases of Reduced Ceria as Epitaxial Films on Cu(111),'" *J. Phys. Chem. C*, vol. 118, no. 9, pp. 5058–5059, Mar. 2014, doi:10.1021/jp412439b.

[216] J. Da Silva, "Stability of the Ce2O3 phases: A DFT+U investigation," *Phys. Rev. B*, vol. 76, no. 19, p. 193108, Nov. 2007, doi:10.1103/PhysRevB.76.193108.

[217] M. Aulická, T. Duchoň, F. Dvořák, V. Stetsovych, J. Beran, K. Veltruská, J. Mysliveček, K. Mašek, and V. Matolín, "Faceting Transition at the Oxide–Metal Interface: (13 13 1) Facets on Cu(110) Induced by Carpet-Like Ceria Overlayer," *J. Phys. Chem. C*, no. 110, 2015, doi:10.1021/jp5099359.

[218] J. Mysliveček, V. Matolín, and I. Matolínová, "Heteroepitaxy of Cerium Oxide Thin Films on Cu(111)," *Materials (Basel).*, vol. 8, no. 9, pp. 6346–6359, Sep. 2015, doi:10.3390/ma8095307.

[219] I. Matolínová, J. Mysliveček, and V. Matolín, "CeOx(111)/Cu(111) Thin Films as Model Catalyst Supports," in *Oxide Materials at the Two-Dimensional Limit*, F. P. Netzer and A. Fortunelli, Eds. Springer International Publishing, 2016, pp. 233–250.

[220] G. E. Murgida, V. Ferrari, M. V. Ganduglia-Pirovano, and A. M. Llois, "Ordering of oxygen vacancies and excess charge localization in bulk ceria: A DFT+U study," *Phys. Rev. B*, vol. 90, no. 11, p. 115120, Sep. 2014, doi:10.1103/PhysRevB.90.115120.

[221] P. Luches and S. Valeri, "Structure, Morphology and Reducibility of Epitaxial Cerium Oxide Ultrathin Films and Nanostructures," *Materials (Basel)*, vol. 8, no. 9, pp. 5818–5833, Aug. 2015, doi:10.3390/ma8095278.

[222] T. Montini, M. Melchionna, M. Monai, and P. Fornasiero, "Fundamentals and Catalytic Applications of CeO2 -Based Materials," *Chem. Rev.*, vol. 116, no. 10, pp. 5987–6041, May 2016, doi:10.1021/acs.chemrev.5b00603.

[223] V. Matolín, I. Matolínová, F. Dvořák, V. Johánek, J. Mysliveček, K. C. Prince, T. Skála, O. Stetsovych, N. Tsud, M. Václavů, and B. Šmíd, "Water interaction with CeO2(111)/Cu(111) model catalyst surface," *Catal. Today*, vol. 181, no. 1, pp. 124–132, Feb. 2012, doi:10.1016/j.cattod.2011.05.032.

[224] D. R. Mullins, P. M. Albrecht, T.-L. Chen, F. C. Calaza, M. D. Biegalski, H. M. Christen, and S. H. Overbury, "Water Dissociation on CeO2(100) and CeO2(111) Thin Films," *J. Phys. Chem. C*, vol. 116, no. 36, pp. 19419–19428, Sep. 2012, doi:10.1021/jp306444h.

[225] B. Chen, Y. Ma, L. Ding, L. Xu, Z. Wu, Q. Yuan, and W. Huang, "Reactivity of Hydroxyls and Water on a CeO2(111) Thin Film Surface: The Role of Oxygen Vacancy," *J. Phys. Chem. C*, vol. 117, no. 11, pp. 5800–5810, Mar. 2013, doi:10.1021/jp312406f.

[226] S. Hu, Y. Wang, W. Wang, Y. Han, Q. Fan, X. Feng, Q. Xu, and J. Zhu, "Ag Nanoparticles on Reducible CeO2(111) Thin Films: Effect of Thickness and Stoichiometry of Ceria," *J. Phys. Chem. C*, vol. 119, no. 111, pp. 3579–3588, 2015, doi:10.1021/jp511691p.

[227] G. Vári, L. Óvári, C. Papp, H. P. Steinrück, J. Kiss, and Z. Kónya, "The Interaction of Cobalt with CeO2(111) Prepared on Cu(111)," *J. Phys. Chem. C*, vol. 119, no. 17, pp. 9324–9333, 2015, doi:10.1021/acs.jpcc.5b00626.

[228] Y. Lykhach, M. Happel, V. Johánek, T. Skála, F. Kollhoff, N. Tsud, F. Dvořák, K. C. Prince, V. Matolín, and J. Libuda, "Adsorption and Decomposition of Formic Acid on Model Ceria and Pt/Ceria Catalysts," *J. Phys. Chem. C*, vol. 117, no. 24, pp. 12483–12494, Jun. 2013, doi:10.1021/jp311008v.

[229] S. Schernich, M. Laurin, Y. Lykhach, H.-P. Steinrück, N. Tsud, T. Skála, K. C. Prince, N. Taccardi, V. Matolín, P. Wasserscheid, and J. Libuda, "Functionalization of Oxide Surfaces through Reaction with 1,3-Dialkylimidazolium Ionic Liquids," *J. Phys. Chem. Lett.*, vol. 4, no. 1, pp. 30–35, Jan. 2013, doi:10.1021/jz301856a.

[230] M. Happel, J. Mysliveček, V. Johánek, F. Dvořák, O. Stetsovych, Y. Lykhach, V. Matolín, and J. Libuda, "Adsorption sites, metal-support interactions, and oxygen spillover identified by vibrational spectroscopy of adsorbed CO: A model study on Pt/ceria catalysts," *J. Catal.*, vol. 289, pp. 118–126, May 2012, doi:10.1016/j.jcat.2012.01.022.

[231] Y. Lykhach, S. M. Kozlov, T. Skála, A. Tovt, V. Stetsovych, N. Tsud, F. Dvořák, V. Johánek, A. Neitzel, J. Mysliveček, S. Fabris, V. Matolín, K. M. Neyman, and J. Libuda, "Counting electrons on supported nanoparticles," *Nat. Mater.*, vol. 15, no. 3, pp. 284–288, Mar. 2016, doi:10.1038/nmat4500.

[232] G. N. Vayssilov, Y. Lykhach, A. Migani, T. Staudt, G. P. Petrova, N. Tsud, T. Skála, A. Bruix, F. Illas, K. C. Prince, V. Matolín, K. M. Neyman, and J. Libuda, "Support nanostructure boosts oxygen transfer to catalytically active platinum nanoparticles," *Nat. Mater.*, vol. 10, no. 4, pp. 310–315, Apr. 2011, doi:10.1038/nmat2976.

[233] M. Hatanaka, N. Takahashi, T. Tanabe, Y. Nagai, K. Dohmae, Y. Aoki, T. Yoshida, and H. Shinjoh, "Ideal Pt loading for a Pt/CeO2-based catalyst stabilized by a Pt–O–Ce bond," *Appl. Catal. B Environ.*, vol. 99, no. 1–2, pp. 336–342, Aug. 2010, doi:10.1016/j.apcatb.2010.07.003.

[234] Q. Fu, H. Saltsburg, and M. Flytzani-Stephanopoulos, "Active Nonmetallic Au and Pt Species on Ceria-Based Water-Gas Shift Catalysts," *Science*, vol. 301, no. 5635, pp. 935–938, Aug. 2003, doi:10.1126/science.1085721.

[235] M. Hatanaka, N. Takahashi, N. Takahashi, T. Tanabe, Y. Nagai, A. Suda, and H. Shinjoh, "Reversible changes in the Pt oxidation state and nanostructure on a ceria-based supported Pt," *J. Catal.*, vol. 266, no. 2, pp. 182–190, Sep. 2009, doi:10.1016/j.jcat.2009.06.005.

[236] X. Yang, A. Wang, B. Qiao, J. Li, J. Liu, and T. Zhang, "Single-Atom Catalysts: A New Frontier in Heterogeneous Catalysis," *Acc. Chem. Res.*, vol. 46, no. 8, pp. 1740–1748, Aug. 2013, doi:10.1021/ar300361m.

[237] M. S. Hegde and P. Bera, "Noble metal ion substituted CeO2 catalysts: Electronic interaction between noble metal ions and CeO2 lattice," *Catal. Today*, vol. 253, pp. 40–50, 2015, doi:10.1016/j.cattod.2015.03.035.

[238]   A. Bruix, Y. Lykhach, I. Matolínová, A. Neitzel, T. Skála, N. Tsud, M. Vorokhta, V. Stetsovych, K. Ševčíková, J. Mysliveček, R. Fiala, M. Václavů, K. C. Prince, S. Bruyère, V. Potin, F. Illas, V. Matolín, J. Libuda, and K. M. Neyman, "Maximum Noble-Metal Efficiency in Catalytic Materials: Atomically Dispersed Surface Platinum," *Angew. Chemie Int. Ed.*, vol. 53, no. 39, pp. 10525–10530, Sep. 2014, doi:10.1002/anie.201402342.

[239]   F. Dvořák, M. Farnesi Camellone, A. Tovt, N. Tran, F. R. Negreiros, M. Vorokhta, T. Skála, I. Matolínová, J. Mysliveček, V. Matolín, and S. Fabris, "Creating single-atom Pt-ceria catalysts by surface step decoration," *Nat. Commun.*, vol. 7, p. 10801, Feb. 2016, doi:10.1038/ncomms10801.

[240]   Y. Zhou, J. M. Perket, and J. Zhou, "Growth of Pt Nanoparticles on Reducible CeO2(111) Thin Films: Effect of Nanostructures and Redox Properties of Ceria," *J. Phys. Chem. C*, vol. 114, no. 27, pp. 11853–11860, 2010, doi:10.1021/jp1007279.

[241]   F. Tao, M. E. Grass, Y. Zhang, D. R. Butcher, J. R. Renzas, Z. Liu, J. Y. Chung, B. S. Mun, M. Salmeron, and G. A. Somorjai, "Reaction-Driven Restructuring of Rh-Pd and Pt-Pd Core-Shell Nanoparticles," *Science*, vol. 322, no. 5903, pp. 932–934, Nov. 2008, doi:10.1126/science.1164170.

[242]   F. Tao, S. Dag, L.-W. Wang, Z. Liu, D. R. Butcher, H. Bluhm, M. Salmeron, and G. A. Somorjai, "Break-Up of Stepped Platinum Catalyst Surfaces by High CO Coverage," *Science*, vol. 327, no. 5967, pp. 850–853, Feb. 2010, doi:10.1126/science.1182122.

[243]   G. A. Somorjai, H. Frei, and J. Y. Park, "Advancing the Frontiers in Nanocatalysis, Biointerfaces, and Renewable Energy Conversion by Innovations of Surface Techniques," *J. Am. Chem. Soc.*, vol. 131, no. 46, pp. 16589–16605, Nov. 2009, doi:10.1021/ja9061954.

[244]   F. Tao, "Design of an in-house ambient pressure AP-XPS using a bench-top X-ray source and the surface chemistry of ceria under reaction conditions," *Chem. Commun.*, vol. 48, no. 32, p. 3812, 2012, doi:10.1039/c2cc17715c.

[245]   M. Salmeron and R. Schlögl, "Ambient pressure photoelectron spectroscopy: A new tool for surface science and nanotechnology," *Surf. Sci. Rep.*, vol. 63, no. 4, pp. 169–199, Apr. 2008, doi:10.1016/j.surfrep.2008.01.001.

[246]   E. Laegsgaard, L. Österlund, P. Thostrup, P. B. Rasmussen, I. Stensgaard, and F. Besenbacher, "A high-pressure scanning tunneling microscope," *Rev. Sci. Instrum.*, vol. 72, no. 9, p. 3537, 2001, doi:10.1063/1.1389497.

[247]   F. Tao and P. A. Crozier, "Atomic-Scale Observations of Catalyst Structures under Reaction Conditions and during Catalysis," *Chem. Rev.*, vol. 116, no. 6, pp. 3487–3539, Mar. 2016, doi:10.1021/cr5002657.

[248]   J. Schnadt, J. Knudsen, J. N. Andersen, H. Siegbahn, A. Pietzsch, F. Hennies, N. Johansson, N. Mårtensson, G. Öhrwall, S. Bahr, S. Mähl, and O. Schaff, "The new ambient-pressure X-ray photoelectron spectroscopy instrument at MAX-lab," *J. Synchrotron Radiat.*, vol. 19, no. 5, pp. 701–704, Sep. 2012, doi:10.1107/S0909049512032700.

[249]   "PHOIBOS 150 NAP Near Ambient Pressure Hemispherical Energy Analyzer." [Online]. Available: http://www.specs.de/cms/front_content.php?idcat=269. [Accessed: 30-Jun-2016].

[250]   J.-H. Wee, "Applications of proton exchange membrane fuel cell systems," *Renew. Sustain. Energy Rev.*, vol. 11, no. 8, pp. 1720–1738, Oct. 2007, doi:10.1016/j.rser.2006.01.005.

[251] M. Carmo, D. L. Fritz, J. Mergel, and D. Stolten, "A comprehensive review on PEM water electrolysis," *Int. J. Hydrogen Energy*, vol. 38, no. 12, pp. 4901–4934, Apr. 2013, doi:10.1016/j.ijhydene.2013.01.151.

[252] N. M. Markovic and P. N. J. Ross, "Surface science studies of model fuel cell electrocatalysts," *Surf. Sci.Reports*, vol. 45, no. 4–6, pp. 117–229, 2002, doi:10.1016/S0167-5729(01)00022-X.

[253] V. Stamenkovic, N. M. Markovic, and P. N. Ross, "Structure-relationships in electrocatalysis: oxygen reduction and hydrogen oxidation reactions on Pt(111) and Pt(100) in solutions containing chloride ions," *J. Electroanal. Chem.*, vol. 500, no. 1–2, pp. 44–51, Mar. 2001, doi:10.1016/S0022-0728(00)00352-1.

[254] V. R. Stamenkovic, B. Fowler, B. S. Mun, G. Wang, P. N. Ross, C. A. Lucas, and N. M. Marković, "Improved oxygen reduction activity on Pt3Ni(111) via increased surface site availability," *Science*, vol. 315, no. 5811, pp. 493–7, Jan. 2007, doi:10.1126/science.1135941.

[255] C. Wang, N. M. Markovic, and V. R. Stamenkovic, "Advanced Platinum Alloy Electrocatalysts for the Oxygen Reduction Reaction," *ACS Catal.*, vol. 2, no. 5, pp. 891–898, May 2012, doi:10.1021/cs3000792.

Appendix 1: Structure of the adatom electron band of the Si(111)-7×7 surface

Structure of the adatom electron band of the Si(111)-7×7 surface

J. Mysliveček, A. Stróżecka, J. Steffl, P. Sobotík, I. Ošt'ádal, and B. Voigtländer,
Phys. Rev. B, vol. 73, no. 16, p. 161302, Apr. 2006,

Appendix 2: Scanning tunneling microscopy contrast in lateral Ge-Si nanostructures on Si(111)-√3×√3-Bi

Appendix 3: Electron-induced excitation of vibrations of Ce atoms inside a C_{80} cage

Electron-induced excitation of vibrations of Ce atoms inside a C_{80} cage
A. Stróżecka, K. Muthukumar, J. a. Larsson, a. Dybek, T. J. S. Dennis, J. Mysliveček, and B. Voigtländer,
Phys. Rev. B, vol. 83, no. 16, p. 165414, Apr. 2011,

Appendix 4: Modification of the conductance of single fullerene molecules by endohedral doping

Appendix 5: On the microscopic origin of the kinetic step bunching instability on vicinal Si(001)

On the microscopic origin of the kinetic step bunching instability on vicinal Si(001)
J. Mysliveček, C. Schelling, F. Schäffler, G. Springholz, P. Šmilauer, J. Krug, and B. Voigtländer,

Appendix 6: Scaling of submonolayer island sizes in surfactant-mediated epitaxy of semiconductors

Appendix 7: Optimized Ge nanowire arrays on Si by modified surfactant mediated epitaxy

Appendix 8: Adsorption and diffusion of Ag atoms on Si(111)-(7×7) surface

Appendix 9: Unconventional features of Ag epitaxy on the Si(111)7×7 surface

A versatile fabrication method for cluster superlattices
A. T. N'Diaye, T. Gerber, C. Busse, J. Mysliveček, J. Coraux, and T. Michely,
New J. Phys., vol. 11, no. 10, p. 103045, Oct. 2009,

Appendix 11: Anode Material for Hydrogen Polymer Membrane Fuel Cell: Pt–CeO$_2$ RF-Sputtered Thin Films

Appendix 13: Nanometer-Range Strain Distribution in Layered Incommensurate Systems

Epitaxial Cubic Ce$_2$O$_3$ Films via Ce–CeO$_2$ Interfacial Reaction

V. Stetsovych, F. Pagliuca, F. Dvořák, T. Duchoň, M. Vorokhta, M. Aulická, J. Lachnitt, S. Schernich, I. Matolínová, K. Veltruská, T. Skála, D. Mazur, J. Mysliveček, J. Libuda, and V. Matolín,

Appendix 16: Ordered Phases of Reduced Ceria As Epitaxial Films on Cu(111)

Ordered Phases of Reduced Ceria As Epitaxial Films on Cu(111)
T. Duchoň, F. Dvořák, M. Aulická, V. Stetsovych, M. Vorokhta, D. Mazur, K. Veltruská, T. Skála, J. Mysliveček, I. Matolínová, and V. Matolín

Heteroepitaxy of Cerium Oxide Thin Films on Cu(111)
J. Mysliveček, V. Matolín, and I. Matolínová,
Materials (Basel)., vol. 8, no. 9, pp. 6346–6359, Sep. 2015,

Appendix 18: Water interaction with CeO$_2$(111)/Cu(111) model catalyst surface

Appendix 20: Counting electrons on supported nanoparticles

Maximum noble-metal efficiency in catalytic materials: atomically dispersed surface platinum.
A. Bruix, Y. Lykhach, I. Matolínová, A. Neitzel, T. Skála, N. Tsud, M. Vorokhta, V. Stetsovych, K. Ševčíková, J. Mysliveček, R. Fiala, M. Václavů, K. C. Prince, S. Bruyère, V. Potin, F. Illas, V. Matolín, J. Libuda, and K. M. Neyman,
Angew. Chem. Int. Ed., vol. 53, no. 39, pp. 10525–30, Sep. 2014,

Document Type: Article,
doi:10.1002/anie.201402342,
IF: 11.261 (2014)

Publisher: John Wiley & Sons, Gesselschaft Deutscher Chemiker

Appendix 22: Creating single-atom Pt-ceria catalysts by surface step decoration